ELECTRO-OPTIC POCKELS CELL VOLTAGE SENSORS FOR ACCELERATOR DIAGNOSTICS

by

Adam Joseph Iverson

A thesis submitted in partial fulfillment
of the requirements for the degree

of

Masters of Science

in

Electrical Engineering

MONTANA STATE UNIVERSITY
Bozeman, Montana

July 2004

APPROVAL

of a thesis submitted by

Adam Joseph Iverson

This thesis has been read by each member of the thesis committee and has been found to be satisfactory regarding content, English usage, format, citations, bibliographic style, and consistency, and is ready for submission to the College of Graduate Studies.

David Dickensheets

Approved for the Department of Electrical & Computer Engineering

James Peterson

Approved for the College of Graduate Studies

Bruce McLeod

STATEMENT OF PERMISSION OF USE

Adam Iverson

07/07/04

TABLE OF CONTENTS

LIST OF TABLES

Table Page

LIST OF FIGURES

Figure Page

LIST OF FIGURES – CONT.

LIST OF FIGURES – CONT.

LIST OF FIGURES – CONT.

ABSTRACT

Three prototype electro-optic Pockels cell voltage sensors were fabricated, each using a different electro-optic crystal. These sensors were to be used in an electron particle accelerator with a pulse length outside of the working range of operation for current electrical B-dot probes. The three crystals of interest were bismuth germanium oxide (BGO), bismuth silicon oxide (BSO) and zinc selenide (ZnSe). Each crystal was bench tested at two different wavelengths to determine sensitivity. BSO was shown to be the most sensitive to voltage, followed by ZnSe. BGO was shown to be the least sensitive to voltage but its other characteristics made it a better choice for voltage sensor use in the accelerator environment.

CHAPTER 1

INTRODUCTION

The propagation of optical radiation through certain materials while in the presence of an electric field demonstrates an interesting phenomenon known as the electro-optic effect. The effect is defined as a deformation of the refractive indices of a material due to an applied electric field. This deformation gives rise to a change in the way polarized light behaves while propagating through the material.

The relationship between the electric field and the change in refractive index primarily takes two forms, the linear and quadratic. In the linear case the change in the refractive index is proportional to the strength of the electric field, whereas the change in the index of refraction is proportional to the square of the field strength in the quadratic case. The quadratic electro-optic effect was first discovered in 1875 by John Kerr and is commonly known as the Kerr effect. The linear electro-optic effect, which was first observed by Röntgen in 1883, is known as the Pockels effect after Fredrich Pockels who developed the theory of the linear electro-optic effect in 1893.

When the linear electro-optic effect is present in a solid it usually dominates the quadratic effect which is typically neglected.(1) Such materials are called Pockels mediums or Pockels cells. When the linear effect is absent and the Kerr effect dominates, the material is known as a Kerr medium or Kerr cell. Higher order effects can be present but are usually ignored because they tend to be very small.(2)

Practical applications of Pockels cells primarily include electro-optic modulators and electro-optic sensors. Both implementations require the incorporation of additional optics and are designed to impress information onto the optical beam propagating through the cell. When used as a modulator, information is applied to the Pockels cell in the form of a known electric field and is encoded into the characteristics of the light passing through the cell. The light is then transmitted to a receiver where the information is decoded. When used as a sensor, specific characteristics of the transmitted light are measured to determine the unknown electric field applied to the Pockels cell. Once the electric field is known, other quantities such as voltage and current can be readily determined.

Electro-optic modulators are used in a wide variety of applications in the telecommunications industry.(3) Companies like JDS Uniphase and Nortel make electro-optic intensity modulators to transmit information across fiber optic networks. Electro-optic modulators are also used to control or scramble the state of polarization of light for information encryption and polarization loss measurements. New and unique applications for electro-optic modulators are continually being developed for the telecommunication industry.(4)

Electro-optic sensors are also being used in a wide variety of industries. Test and measurement companies like ANDO are developing them for high-impedance electrical probes where it is difficult to obtain measurements using standard electronic methods.(5) Companies like Westinghouse Electric Corp.(6), ABB Power T&D(7,8) and NxtPhase Corp.(9) have been developing and deploying electro-optic voltage sensors for high voltage line monitoring applications in the power utility industry. Another new area where electro-optic sensor use is being implemented is in the diagnostic systems of particle accelerators.(10,11) Scientists and engineers at Los Alamos National Laboratory in Los Alamos, New Mexico are investigating their performance in pulsed power and electron particle accelerator monitoring applications.(12,13,14,15) It is this area of use which we shall primarily discuss in this paper.

The dual-axis radiographic hydrodynamic test (DARHT) facility currently under construction at Los Alamos National Laboratory in Los Alamos, New Mexico is a dual-axis electron particle accelerator used to generate very intense x-rays for hydrodynamic radiography.(16) This facility utilizes two separate linear electron particle accelerators oriented at 90° to each other. Figure (1-1) shows an aerial view of the DARHT facility.

Figure (1-1) – DARHT facility in Los Alamos, New Mexico

This configuration enables scientists to perform three-dimensional radiographic imaging and analysis. The first axis of DARHT nominally generates a 20 MeV, 2 kA burst of electrons 60 nanoseconds long. When the second axis is completed, it will generate a 20 MeV, 2 kA pulse approximately 30 times longer on the order of 2 microseconds. The beam energy of the first axis is about 2.4 kJ and due to the longer time scale, the second axis will have a beam energy of approximately 80 kJ. Beam monitoring diagnostics are essential to the successful and safe operation of each accelerator.

The first axis of DARHT uses conventional non-invasive diagnostic probes called B-dots to accurately monitor the current and position of the electron beam within the accelerator. Four B-dot probes are mounted 90° apart on a ring section of the accelerator. If a perfectly uniform beam of electrons travel through the exact center of the accelerator, the signals from each calibrated probe will be the same. Differences in these signals are used to determine the position of the beam in that section of the accelerator while the magnitude of the signal can be used to determine the beam current. B-dots use a wire loop mounted near the accelerator wall to measure the change in the magnetic field inside the accelerator caused by the passing electrons. According to Faraday's law, a current will flow around a closed conducting loop that is proportional to the change in the magnetic field intersected by the loop. The induced loop current in the B-dot flows across a resistor causing a voltage drop that can be easily and accurately measured. The measured voltage in the B-dot is proportional to the time derivative of the beam current and must therefore be time integrated. Typically this is done using analog hardware integrators with the proper time constant.

The longer time scale of the second axis of DARHT poses significant measurement challenges and has prompted the development of new sensors. The B-dots used in the first axis are not well suited for the second axis because the longer integration time and reduced rates of change in the magnetic field cause excessive drooping and signal attenuation.(14) Therefore a sensor capable of making a directly proportional measurement of the beam current, instead of the time derivative, is desired. Other challenges that conventional diagnostics face are time isolation and ground loops. Aside from creating electron pulses, particle accelerators generate enormous amounts of electrical noise. A signal acquired by local acquisition systems without proper isolation will be excessively noisy and susceptible to feedback. To solve these problems, suitable yet practical lengths of cable called delay lines are used to delay the signals produced by the B-dots before they are acquired by the data acquisition system. This allows time for the accelerator noise and ringing to dissipate. Time isolation for the first axis is achieved using delay cables approximately 200 meters long. The second axis would require delay lines of approximately five kilometers, which is impractical. These problems have prompted engineers to develop electro-optic sensors for the second axis of DARHT.

Electro-optic sensors are ideally suited for noninvasive electron beam diagnostic applications because they do not suffer from many of the problems of conventional diagnostics. Electro-optic sensors utilize electrically insulating fiber optic cables to transmit the sensor signals to the acquisition system. By galvanically isolating the sensor from the data acquisition system, the time isolation and ground loop problems associated with the longer time scale are solved. Electro-optic sensors also have an intrinsic advantage over conventional electronic sensors on a longer time scale. Traditional B-dots produce a signal proportional to the time derivative of the beam current, thus requiring the signal to be integrated before being acquired.(15) The signals from an electro-optic probe do not require time integration because there exists a linear relationship between the field created by the beam and the measured optical signal. This advantage is the primary reason that electro-optic sensors are being investigated for accelerator applications.

The Pockels material used in electro-optic voltage sensors is key in developing a functional and accurate electro-optic sensor. Bulk electro-optic crystals work well and are easily incorporated as Pockels cells if the appropriate crystal is selected. Materials such as KH_2PO_4 (KDP) and $LiNbO_3$ are very common choices due to the large Pockels effect they demonstrate.(1) However, the harsh particle accelerator environment offers substantial challenges in selecting appropriate electro-optic crystals that yield the required accuracy, durability, dynamic range and performance.

Electron particle accelerators produce extremely high-energy electron beams, resulting in very strong electric fields.(16) If the crystal is too sensitive the induced electric field could saturate the sensor. If the crystal is not sensitive enough, dynamic range is forfeited. The wavelength of operation can also affect the performance of the sensor system as the electro-optic coefficient of the crystal depends upon wavelength. This will become apparent in the next chapter. The crystal must also be able to withstand the high vacuum, intense radiation and free electron, ion and photon impacts which are typically found in accelerator environments.

This thesis investigates the performance of three crystal candidates for electro-optic voltage sensors used in accelerator diagnostic applications. The three crystals chosen were bismuth germanium oxide ($Bi_4Ge_3O_{12}$), zinc selenide (ZnSe) and bismuth silicon oxide ($Bi_{12}SiO_{20}$). Bismuth germanium oxide (BGO) was selected as our initial crystal candidate because it has been extensively used and tested in harsh environments similar to those found in accelerators. Its good performance and durability in those harsh environments have been reported in the literature.(17,18,19) Zinc selenide and bismuth silicon oxide (BSO) have not been as widely used or tested in harsh environments but were chosen because they exhibit physical and optical characteristics similar to BGO.(1,20,21) The following chapter will explain more of the differences and similarities between the three crystals.

The theory of how an electro-optic Pockels cell voltage sensor works is presented in the following chapters. It has been separated into two sections where the electro-optic theory itself is first investigated and then the theory of operation of the voltage sensor is given. Experiments have been conducted to test the performance of each crystal candidate in the laboratory and prototype voltage sensors have been fabricated using each crystal type. The results of the crystal experiments have been analyzed and are presented. Finally a conclusion and recommendations for future work is given in the final chapter. Included in the Appendix is a Jones calculus analysis of the experiments, sensors and BSO crystal experiment.

CHAPTER 2

THEORY

Electro-Optic Crystals

Before we can understand how an electro-optic sensor works, we must investigate the mechanism behind the sensor, namely the electro-optic effect. The key component of any electro-optic sensor is the electro-optic crystal. Its characteristics ultimately determine the overall sensor performance. Electro-optic crystals are simply crystals that exhibit electro-optic properties, and a crystal is any solid whose atoms are arranged in an orderly and repetitive way.(30) Every crystal in fact exhibits some type of electro-optic property(30), but it is the Pockels effect that we are interested in.

The three crystals researched are cubic crystals, meaning they all have a cubic atomic structure. This atomic structure provides us a convenient way to describe direction within the crystal by applying a rectangular coordinate system to the crystal axes. Using this coordinate system, we may mathematically define the direction of propagation and polarization of the light within the crystal. We are also able to use this coordinate system as a way of orienting additional optical components. Figure (2-1) shows the orientation of the coordinate system to a unit cell that defines the cubic structure of the crystal. It should be pointed out that the location of the origin is irrelevant and only the coordinate directions are important.

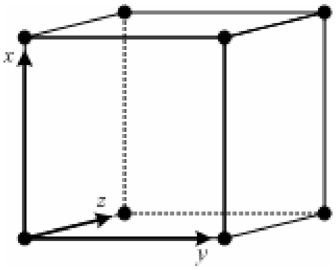

Figure (2-1) – Unit cell coordinate system

BGO, ZnSe and BSO are cubic crystals with BGO and ZnSe belonging to symmetry group $\bar{4}3m$ (T_d) and BSO belonging to group 23 (T). BGO and ZnSe are functionally identical, however BSO has an intrinsic property called optical activity. Optical activity in a crystal causes the direction of incident polarization to be rotated as it travels through the crystal. We shall discuss this property further in the following chapters.

We investigate the Pockels effect as it specifically pertains to the crystals we have chosen to research. We use the work of Yariv(1,4,23) as a guide for the derivations of the linear electro-optic effect throughout this chapter. For a more complete and general description of the electro-optic effect please consult the individual references listed in the bibliography at the end of this thesis.

Linear Electro-Optic Effect

If the crystal we are interested in is optically transparent at the wavelength of interest, then the primary optical property we are concerned with is the index of refraction. In its simplest description, the Pockels effect deals with a change in the refractive index of the crystal when an electric field is applied to it. The optical properties of an electro-optic crystal can be described by what is known as the index ellipsoid. The equation is given by

$$\left(\frac{1}{n_x^2}\right)x^2 + \left(\frac{1}{n_y^2}\right)y^2 + \left(\frac{1}{n_z^2}\right)z^2 = 1 \tag{2-1}$$

where x, y and z are the principal or crystallographic axes of the crystal and n_x, n_y and n_z are the principal indices of refraction in the x, y and z directions respectively. This equation holds for zero applied electric field.

The equation for the index ellipsoid of a crystal in an arbitrary external electric field $E(E_x, E_y, E_z)$ is

$$\begin{aligned} &\left(\frac{1}{n^2}\right)_1 x^2 + \left(\frac{1}{n^2}\right)_2 y^2 + \left(\frac{1}{n^2}\right)_3 z^2 \\ &+ 2\left(\frac{1}{n^2}\right)_4 yz + 2\left(\frac{1}{n^2}\right)_5 xz + 2\left(\frac{1}{n^2}\right)_6 xy = 1 \end{aligned} \tag{2-2}$$

and if x, y and z are aligned with the principal axes of the crystal and $E = 0$, then Equation (2-2) must reduce to Equation (2-1) and

$$\left(\frac{1}{n^2}\right)_1\Bigg|_{E=0} = \frac{1}{n_x^2}$$

$$\left(\frac{1}{n^2}\right)_2\Bigg|_{E=0} = \frac{1}{n_y^2}$$

$$\left(\frac{1}{n^2}\right)_3\Bigg|_{E=0} = \frac{1}{n_z^2}$$

$$\left(\frac{1}{n^2}\right)_4\Bigg|_{E=0} = 0 \qquad \text{(2-3)}$$

$$\left(\frac{1}{n^2}\right)_5\Bigg|_{E=0} = 0$$

$$\left(\frac{1}{n^2}\right)_6\Bigg|_{E=0} = 0$$

The change in the coefficients of the left sides of the above equations is given by

$$\Delta\left(\frac{1}{n^2}\right)_i = \left(\frac{1}{n^2}\right)_i - \left(\frac{1}{n^2}\right)_i\Bigg|_{E=0} \qquad i = 1,2,\ldots 6 \qquad \text{(2-4)}$$

and is defined by

$$\Delta\left(\frac{1}{n^2}\right)_i = \sum_{j=1}^{3} r_{ij} E_j \qquad \text{(2-5)}$$

where the values $j = 1,2,3$ represent *x*, *y* and *z*, respectively. This definition allows us to express Equation (2-5) in matrix form as

$$\begin{bmatrix} \Delta\left(\frac{1}{n^2}\right)_1 \\ \Delta\left(\frac{1}{n^2}\right)_2 \\ \Delta\left(\frac{1}{n^2}\right)_3 \\ \Delta\left(\frac{1}{n^2}\right)_4 \\ \Delta\left(\frac{1}{n^2}\right)_5 \\ \Delta\left(\frac{1}{n^2}\right)_6 \end{bmatrix} = \begin{bmatrix} r_{11} & r_{12} & r_{13} \\ r_{21} & r_{22} & r_{23} \\ r_{31} & r_{32} & r_{33} \\ r_{41} & r_{42} & r_{43} \\ r_{51} & r_{52} & r_{53} \\ r_{61} & r_{62} & r_{63} \end{bmatrix} \cdot \begin{bmatrix} E_x \\ E_y \\ E_z \end{bmatrix} \tag{2-6}$$

where the 6 x 3 matrix of r_{ij} is called the electro-optic tensor matrix of the crystal. Substituting Equations (2-3) and (2-6) into Equation (2-4) gives

$$\left(\frac{1}{n^2}\right)_1 = r_{11}E_x + r_{12}E_y + r_{13}E_z + \frac{1}{n_x^2}$$

$$\left(\frac{1}{n^2}\right)_2 = r_{21}E_x + r_{22}E_y + r_{23}E_z + \frac{1}{n_y^2}$$

$$\left(\frac{1}{n^2}\right)_3 = r_{31}E_x + r_{32}E_y + r_{33}E_z + \frac{1}{n_z^2}$$

$$\left(\frac{1}{n^2}\right)_4 = r_{41}E_x + r_{42}E_y + r_{43}E_z$$

$$\left(\frac{1}{n^2}\right)_5 = r_{51}E_x + r_{52}E_y + r_{53}E_z$$

$$\left(\frac{1}{n^2}\right)_6 = r_{61}E_x + r_{62}E_y + r_{63}E_z \tag{2-7}$$

which can be substituted into Equation (2-2) for the expanded index ellipsoid equation of

$$\begin{aligned}&\left(r_{11}E_x + r_{12}E_y + r_{13}E_z + \frac{1}{n_x^2}\right)x^2 + \left(r_{21}E_x + r_{22}E_y + r_{23}E_z + \frac{1}{n_y^2}\right)y^2\\ &+\left(r_{31}E_x + r_{32}E_y + r_{33}E_z + \frac{1}{n_z^2}\right)z^2 + 2\left(r_{41}E_x + r_{42}E_y + r_{43}E_z\right)yz\\ &+2\left(r_{51}E_x + r_{52}E_y + r_{53}E_z\right)xz + 2\left(r_{61}E_x + r_{62}E_y + r_{63}E_z\right)xy = 1\end{aligned} \tag{2-8}$$

To simplify this equation we reduce the electro-optic tensor matrix based on the symmetry of the crystal chosen. BGO, ZnSe and BSO all have the same electro-optic tensor matrix of

$$\bar{4}3m, 23$$

$$\begin{bmatrix} 0 & 0 & 0 \\ 0 & 0 & 0 \\ 0 & 0 & 0 \\ r_{41} & 0 & 0 \\ 0 & r_{41} & 0 \\ 0 & 0 & r_{41} \end{bmatrix} \qquad \text{(2-9)}$$

which leads to

$$\begin{bmatrix} r_{11} & r_{12} & r_{13} \\ r_{21} & r_{22} & r_{23} \\ r_{31} & r_{32} & r_{33} \\ r_{41} & r_{42} & r_{43} \\ r_{51} & r_{52} & r_{53} \\ r_{61} & r_{62} & r_{63} \end{bmatrix} = \begin{bmatrix} 0 & 0 & 0 \\ 0 & 0 & 0 \\ 0 & 0 & 0 \\ r_{41} & 0 & 0 \\ 0 & r_{41} & 0 \\ 0 & 0 & r_{41} \end{bmatrix} \qquad \text{(2-10)}$$

and if we choose x, y and z to be parallel to the crystallographic axes of the crystal, Equation (2-8) reduces to

$$\left(\frac{1}{n_o^2}\right)x^2 + \left(\frac{1}{n_o^2}\right)y^2 + \left(\frac{1}{n_o^2}\right)z^2 + 2r_{41}E_x yz + 2r_{41}E_y xz + 2r_{41}E_z xy = 1 \qquad \text{(2-11)}$$

We can further simplify Equation (2-11) by defining the orientation of the applied electric field to be parallel to the z direction ($E_x = E_y = 0$, $E_z = E$).

$$\left(\frac{1}{n_o^2}\right)x^2 + \left(\frac{1}{n_o^2}\right)y^2 + \left(\frac{1}{n_o^2}\right)z^2 + 2r_{41}E_z xy = 1 \tag{2-12}$$

It can easily be seen that with no applied field, Equation (2-12) equals the undistorted index ellipsoid of Equation (2-1). We notice that Equation (2-12) has an additional mixed term, which means that the major dielectric axes of the ellipsoid (*x'*, *y'* and *z'*) are no longer parallel to the crystallographic axes of the crystal (*x*, *y* and *z*). We must choose a new coordinate system so that Equation (2-12) transforms into the form

$$\left(\frac{1}{n_{x'}^2}\right)x'^2 + \left(\frac{1}{n_{y'}^2}\right)y'^2 + \left(\frac{1}{n_{z'}^2}\right)z'^2 = 1 \tag{2-13}$$

By inspection, we can see that our new coordinate system must have *z'* parallel to *z* and also that *x'* and *y'* are related to *x* and *y* by a rotation of θ about *z*. Figure (2-2) shows this new coordinate system.

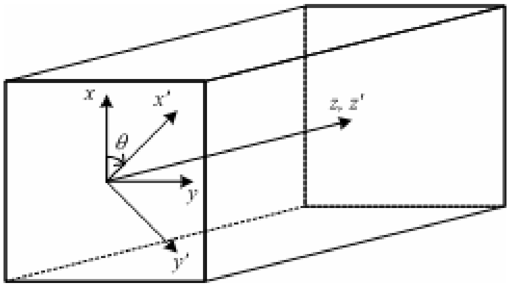

Figure (2-2) – Coordinate rotation

The new coordinates are related by

$$
\begin{aligned}
x &= x' \cos\theta - y' \sin\theta \\
y &= x' \sin\theta + y' \cos\theta \\
z &= z'
\end{aligned}
\tag{2-14}
$$

If we substitute Equation (2-14) into Equation (2-12) it becomes

$$
\begin{aligned}
&\frac{(x' \cos\theta - y' \sin\theta)^2}{n_o^2} + \frac{(x' \sin\theta + y' \cos\theta)^2}{n_o^2} + \left(\frac{1}{n_o^2}\right) z'^2 \\
&+ 2r_{41} E_z (x' \cos\theta - y' \sin\theta)(x' \sin\theta + y' \cos\theta) = 1
\end{aligned}
\tag{2-15}
$$

which leads to

$$
\begin{aligned}
&\left(\frac{\cos^2\theta + \sin^2\theta}{n_o^2}\right) x'^2 + \left(\frac{\sin^2\theta + \cos^2\theta}{n_o^2}\right) y'^2 + \left(\frac{1}{n_o^2}\right) z'^2 \\
&+ 2r_{41} E_z \left(x'^2 \cos\theta \sin\theta + x'y' \cos^2\theta - x'y' \sin^2\theta - y'^2 \sin\theta \cos\theta\right) = 1
\end{aligned}
\tag{2-16}
$$

or

$$
\begin{aligned}
&\left(\frac{1}{n_o^2}\right) x'^2 + \left(\frac{1}{n_o^2}\right) y'^2 + \left(\frac{1}{n_o^2}\right) z'^2 \\
&+ 2r_{41} E_z \left(x'^2 \cos\theta \sin\theta + x'y' \cos^2\theta - x'y' \sin^2\theta - y'^2 \sin\theta \cos\theta\right) = 1
\end{aligned}
\tag{2-17}
$$

The symmetry of the crystal group leads us to choose $\theta = 45°$ which nicely reduces Equation (2-17) to

$$\left(\frac{1}{n_o^2} + r_{41}E_z\right)x'^2 + \left(\frac{1}{n_o^2} - r_{41}E_z\right)y'^2 + \left(\frac{1}{n_o^2}\right)z'^2 = 1 \tag{2-18}$$

by removing the cross terms containing $x'y'$. Equation (2-18) is now in the form of Equation (2-13), which means that

$$\begin{aligned} \frac{1}{n_{x'}^2} &= \frac{1}{n_o^2} + r_{41}E_z \\ \frac{1}{n_{y'}^2} &= \frac{1}{n_o^2} - r_{41}E_z \\ \frac{1}{n_{z'}^2} &= \frac{1}{n_o^2} \end{aligned} \tag{2-19}$$

If we assume the differential change in the refractive index of the crystal to be small when an electric field is present,

$$r_{41}E_z \ll \frac{1}{n_o^2} \tag{2-20}$$

we can rewrite Equation (2-19) as

$$\begin{aligned} \frac{1}{n_{x'}^2} &\approx \frac{1}{n_o^2} \\ \frac{1}{n_{y'}^2} &\approx \frac{1}{n_o^2} \\ \frac{1}{n_{z'}^2} &= \frac{1}{n_o^2} \end{aligned} \tag{2-21}$$

which also leads us to

$$\begin{aligned} n_{x'} &\approx n_o \\ n_{y'} &\approx n_o \\ n_{z'} &= n_o \end{aligned} \qquad (2\text{-}22)$$

The assumption of a small differential change in the refractive index also allows us to rewrite Equations (2-21) and (2-22) as

$$\begin{aligned} \frac{1}{n_{x'}^2} &= \frac{1}{n_o^2} + \frac{d}{dn}\left(\frac{1}{n_o^2}\right) \\ \frac{1}{n_{y'}^2} &= \frac{1}{n_o^2} - \frac{d}{dn}\left(\frac{1}{n_o^2}\right) \\ \frac{1}{n_{z'}^2} &= \frac{1}{n_o^2} \end{aligned} \qquad (2\text{-}23)$$

and

$$\begin{aligned} n_{x'} &= n_o + \frac{d}{dn}\left(n_o\right) \\ n_{y'} &= n_o + \frac{d}{dn}\left(n_o\right) \\ n_{z'} &= n_o \end{aligned} \qquad (2\text{-}24)$$

In order to solve for $n_{x'}$ and $n_{y'}$ we make use of the following differential identity

$$\frac{d}{dn}\left(n_o\right) = -\frac{1}{2}n_o^3\,\frac{d}{dn}\left(\frac{1}{n_o^2}\right) \tag{2-25}$$

and substitute Equations (2-25) and (2-23) into Equation (2-24) to get

$$\begin{aligned} n_{x'} - n_o &= -\frac{1}{2}n_o^3\left(\frac{1}{n_{x'}^2} - \frac{1}{n_o^2}\right) \\ n_{y'} - n_o &= -\frac{1}{2}n_o^3\left(\frac{1}{n_{y'}^2} - \frac{1}{n_o^2}\right) \\ n_{z'} &= n_o \end{aligned} \tag{2-26}$$

and when we use Equation (2-19), we can write

$$\begin{aligned} n_{x'} &= n_o - \frac{1}{2}n_o^3 r_{41} E_z \\ n_{y'} &= n_o + \frac{1}{2}n_o^3 r_{41} E_z \\ n_{z'} &= n_o \end{aligned} \tag{2-27}$$

Equation (2-27) gives the new indices of refraction along the major dielectric axes of the crystal with an electric field, E_z applied longitudinally. The difference in the index of refraction between *x'* and *y'* is the induced birefringence caused by the electric field.

$$\left(n_{y'} - n_{x'}\right) = n_o^3 r_{41} E_z \tag{2-28}$$

This change in the index of refraction leads to a phase difference in the light traveling through the crystal.

Consider a beam of light that is linearly polarized along the crystallographic *x*-axis, traveling in the *z* direction.

$$\varepsilon_x = Ae^{i(\omega t - k_x z)} \tag{2-29}$$

That beam can be resolved into two components polarized along the major dielectric *x'* and *y'* axes

$$\begin{aligned} \varepsilon_{x'} &= Ae^{i(\omega t - k_{x'} z)} \\ \varepsilon_{y'} &= Ae^{i(\omega t - k_{y'} z)} \end{aligned} \tag{2-30}$$

where $k_{x'} = (2\pi/\lambda_o)n_{x'}$ and $k_{y'} = (2\pi/\lambda_o)n_{y'}$. We then use Equation (2-27) to rewrite Equation (2-30) as

$$\begin{aligned} \varepsilon_{x'} &= Ae^{i\left[\omega t - (2\pi/\lambda_o)\left(n_o - 1/2 n_o^3 r_{41} E_z\right)z\right]} = Ae^{i\phi_{x'}} \\ \varepsilon_{y'} &= Ae^{i\left[\omega t - (2\pi/\lambda)\left(n_o + 1/2 n_o^3 r_{41} E_z\right)z\right]} = Ae^{i\phi_{y'}} \end{aligned} \tag{2-31}$$

The phase difference between the components is called the retardance and is defined by

$$\Gamma = \phi_{x'} - \phi_{y'} \tag{2-32}$$

which expands to

$$\Gamma = \left(\omega t - \frac{2\pi n_o z}{\lambda_o} + \frac{\pi n_o^3 r_{41} E_z z}{\lambda_o} \right) - \left(\omega t - \frac{2\pi n_o z}{\lambda_o} - \frac{\pi n_o^3 r_{41} E_z z}{\lambda_o} \right) \tag{2-33}$$

and then reduces to

$$\Gamma = \frac{2\pi n_o^3 r_{41} V}{\lambda_o} \tag{2-34}$$

where $V = E_z z$ for a given length.

This phase difference is essentially the phase delay between orthogonal polarizations and is commonly termed birefringence. In electro-optic crystals, this birefringence is caused by an applied electric field. There are materials, however, that inherently exhibit this type of phase delay. Calcite, quartz and mica are common materials that demonstrate natural birefringence. Another term commonly used in place of birefringence is double refraction, and materials that exhibit this are called doubly refracting crystals.

The above theory shows what the electro-optic effect is and what happens to electro-optic crystals when in the presence of an electric field. The following section deals with the use of the electro-optic effect in electro-optic sensors.

Pockels Cells

The term Pockels cell, as mentioned in the introduction, describes a material that exhibits the linear electro-optic effect. While that description is accurate, there is more to it. Technically a Pockels cell is made up of the electro-optic crystal and two electrodes. These two electrodes provide a means of applying an electric field across the crystal. The placement of the electrodes of a Pockels cell may be one of two configurations, either transverse or longitudinal. They are named as such to describe the orientation the electric field has to the optical beam passing through the crystal. The transverse orientation requires the electrodes to be on the sides of the crystal with the beam passing through the ends of the crystal. Figure (2-3) shows this configuration.

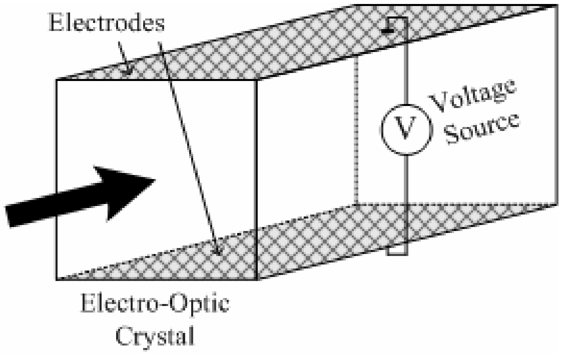

Figure (2-3) – Transverse Pockels cell

The longitudinal configuration requires the electrodes to be on the ends of the crystal with the beam also passing through the ends of the crystal. This orientation causes a throughput problem that is remedied by one of the following options shown in Figure (2-4).

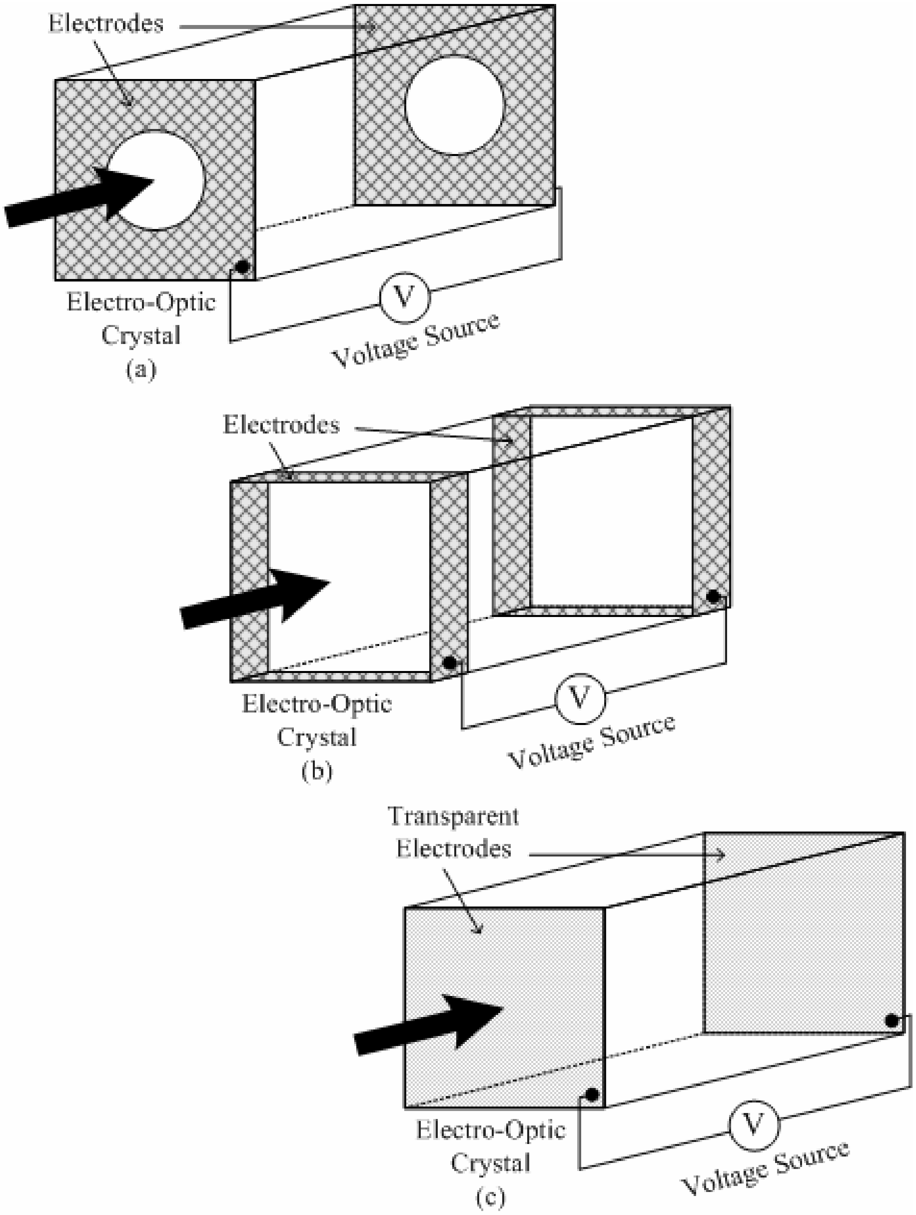

Figure (2-4) – Longitudinal Pockels cells

Figure (2-4 (a)) shows the electrodes mounted to the ends of the crystal but they have a hole large enough for the optical beam to pass through. A hole of small enough size will not significantly affect the electric field distribution within the crystal. Figure (2-4 (b)) show another option of mounting the electrodes on the sides near the ends of the crystal. This allows the beam full access to the ends of the crystal and does not limit the field of view of the Pockels cell as in the first option. This configuration would typically be used when the size of the crystal is close to the size of the beam, leaving little room for electrodes on the ends of the crystal. The electric field distribution will be essentially uniform along the crystal with a small enough crystal cross section. The final option, shown in Figure (2-4 (c)), utilizes an optically transparent conductor to coat the ends of the crystal thereby providing transparent electrodes. This configuration would yield a wide field of view and a uniform longitudinal electric field distribution, but could raise insertion loss issues due to the transparent coating.

The performance of the transverse Pockels cell is different from that of the longitudinal cell. According to electro-optic theory, the birefringence created by a longitudinal Pockels cell is dependent only upon the electric field applied to the crystal. In the transverse configuration, the amount of birefringence created depends upon the applied field strength and the length of the Pockels cell. This may or may not be helpful, depending upon your application. To achieve a desired amount of birefringence in the longitudinal case, you simply vary the strength of the applied electric field. However, if the electric field needed to achieve the required birefringence is too great, an electrical breakdown condition may occur. In the case of the transverse cell, you can vary the field strength and the length of the Pockels cell to achieve your desired birefringence. This helps avoid the potential problems of electrical breakdown but can give rise to an additional problem. As the length of the crystal increases, the field of view decreases. If field of view is not an issue, then transverse Pockels cells work well. For this project we have chosen the longitudinal configuration because we require a larger field of view. The geometry of the longitudinal Pockels cell also lends itself well to the physical constraints of the sensor design, which is detailed in the next chapter.

Electro-Optic Sensors

We have already seen in the math that linearly polarized light must enter the crystal along a specific axis in order for the electro-optic effect to add a phase retardance to the polarized light. With a correctly oriented polarizer and Pockels cell, we can construct a phase modulator. Phase is difficult to actively measure, so we add a second polarizer to the system oriented 90° to the first. This second polarizer acts as an analyzer, thus converting the phase modulation into an amplitude modulation. Figure (2-5) shows this configuration.

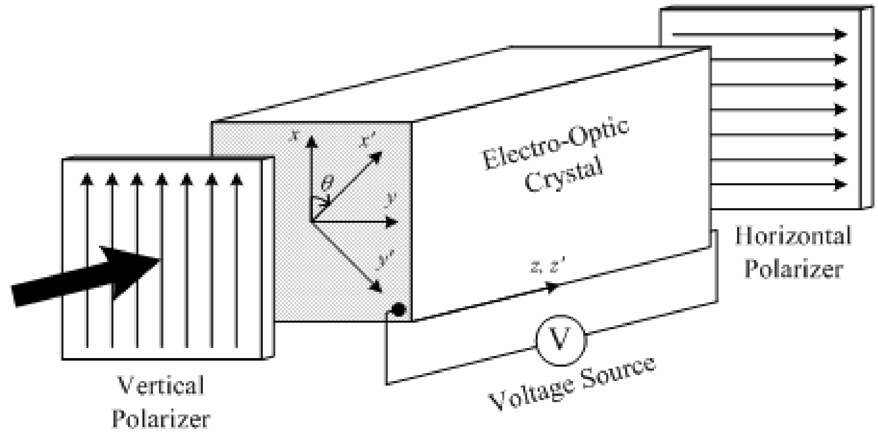

Figure (2-5) – Amplitude modulator

The transmission through this system is represented by

$$T = \sin^2\left(\frac{\Gamma}{2}\right) \tag{2-35}$$

where Γ is the phase delay caused by the Pockels cell. Equation (2-35) can be expanded by substituting for Γ using Equation (2-34).

$$T = \sin^2\left(\frac{\pi n_o^3 r_{41} V}{\lambda_o}\right) \tag{2-36}$$

As the applied voltage (*V*) varies, the transmission through the system (*T*) changes. The normalized intensity through such a system is shown in Figure (2-6).

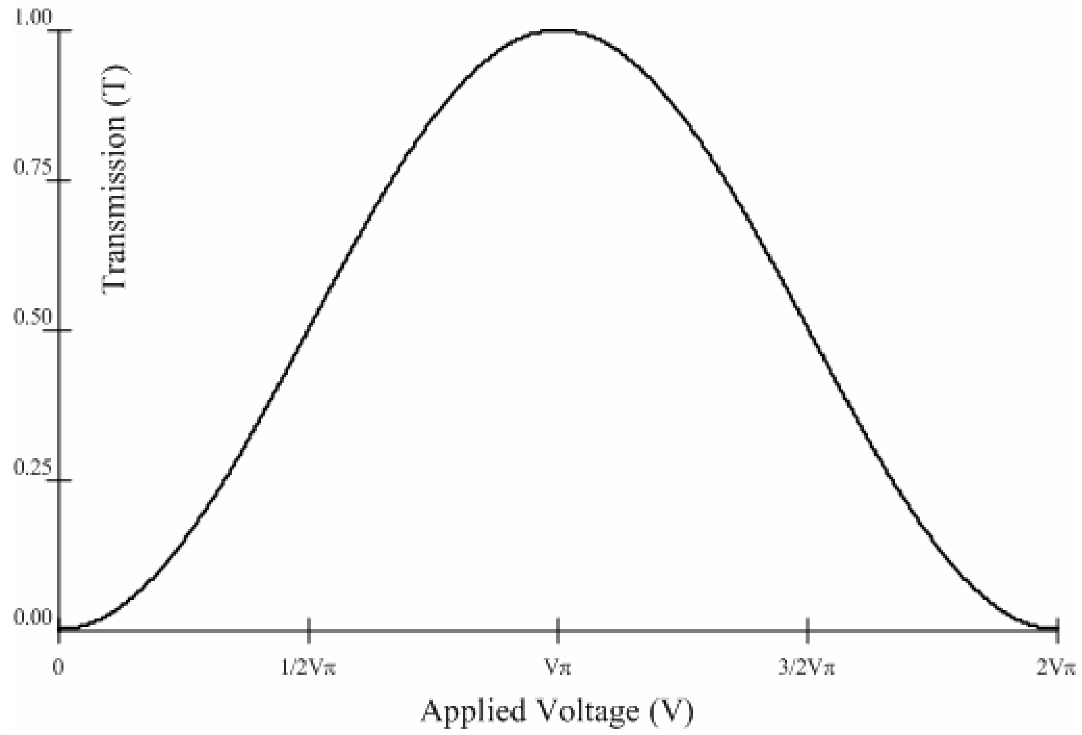

Figure (2-6) – Amplitude modulator transmission curve

The voltage applied to the crystal that leads to a phase retardance of π (180°) is called the half-wave voltage, V_π. When this voltage is applied to the Pockels cell, the linear vertical polarization that enters the Pockels cell is converted into linear horizontal polarization. This then allows for 100% of the light to pass through the horizontal analyzer. If more voltage is applied, the phase delay is increased until the polarization of the light becomes linear vertical again and the intensity of the transmitted light decreases back to zero. This squared sine equation continues indefinitely.

Three factors contribute to the sensitivity of an electro-optic crystal. The free-space wavelength of operation (λ_o), the ordinary index of refraction of the crystal (n_o)

and, most importantly, the electro-optic coefficient (r_{ij}). These factors determine the value of V_π by the following

$$V_\pi = \frac{\lambda_o}{2n_o^3 r_{ij}} \tag{2-37}$$

A crystal with a smaller V_π value will require less voltage to achieve a π phase delay, thereby making the crystal more sensitive than one with a larger value of V_π. Now that we have defined the half-wave voltage, we can rewrite the transmission equation for an amplitude modulator as

$$T = \sin^2\left(\frac{\pi}{2}\frac{V}{V_\pi}\right) \tag{2-38}$$

We can add a fixed amount of natural phase retardance to the light in the voltage sensor by including a waveplate, which would be the same as applying a DC bias voltage to the Pockels cell. This is done to add extra birefringence, thus biasing the sensor output at the quadrature point of the curve in Figure (2-6). The quadrature point of the transmission curve is the region that gives the most linear intensity response to applied voltage, thus improving accuracy and sensitivity. The amount of phase retardance needed to reach this bias point is one quarter wave, or $\pi/2$. To accomplish this, a zero order quarter wave retarder is placed in between the two linear polarizers. Its extraordinary and ordinary (fast and slow) axes are aligned to the *x'* and *y'* axes of the crystal. Figure (2-7) shows the addition of the waveplate.

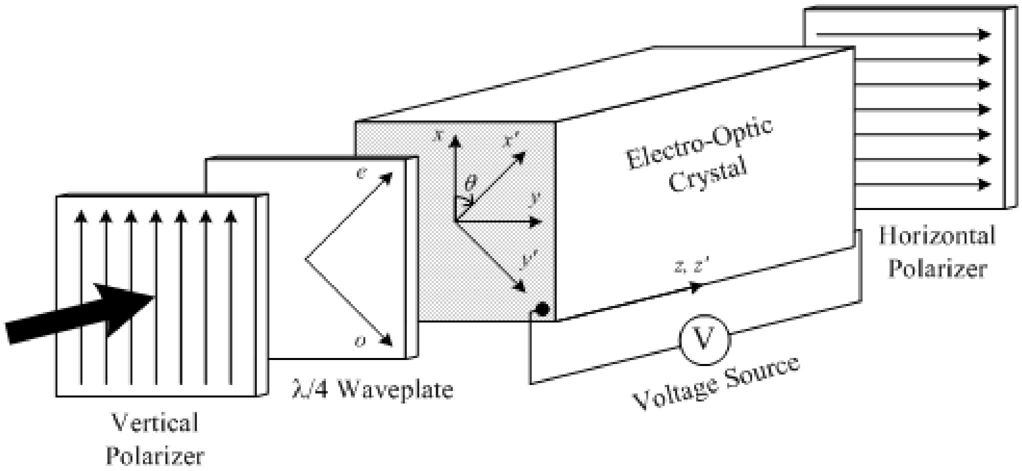

Figure (2-7) – Biased amplitude modulator

This changes Equation (2-35) to

$$T = \sin^2\left(\frac{\Gamma + \Phi}{2}\right) \tag{2-39}$$

where *Φ* is the fixed *π*/2 phase shift introduced by the quarter waveplate. We are now able to mathematically describe a biased amplitude modulator as

$$T = \sin^2\left(\frac{\pi}{2}\frac{V}{V_\pi} + \frac{\pi}{4}\right) \tag{2-40}$$

This additional phase component shifts the curve in Figure (2-6) to the left as seen in Figure (2-8).

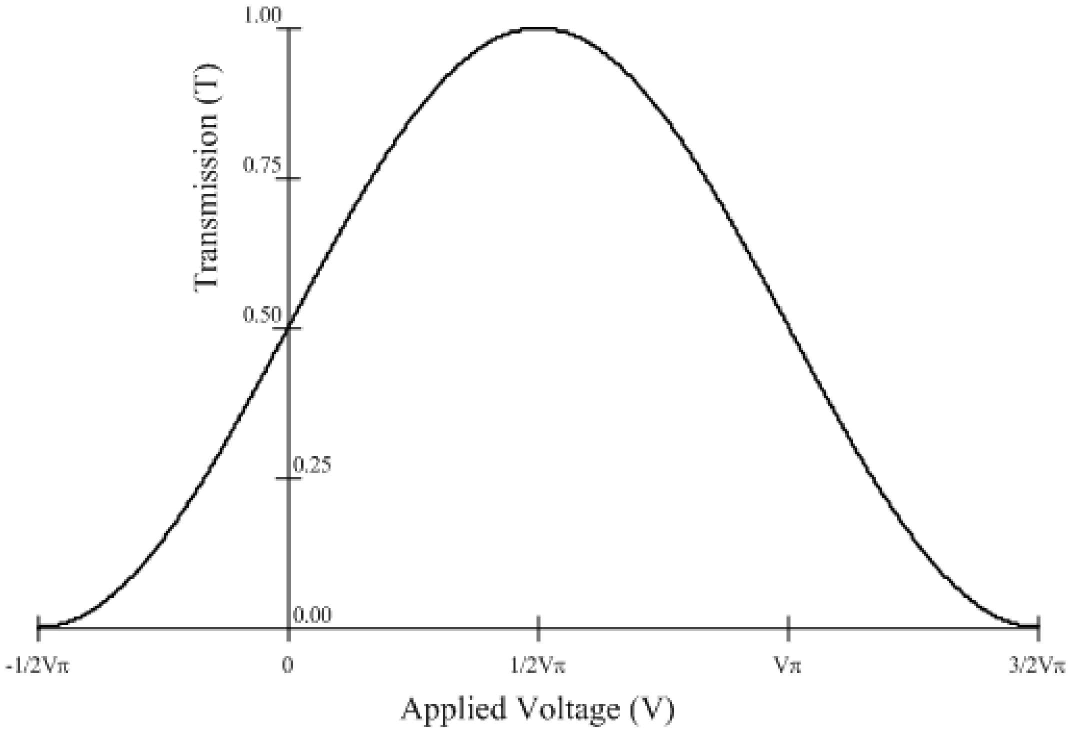

Figure (2-8) – Biased amplitude modulator transmission curve

When there is no applied voltage, the vertical linear polarization is converted into right-hand circular polarization. When $V = 0$, half of the light makes it through the biased amplitude modulator, as shown in Figure (2-8). We can now see that a small applied voltage will cause the greatest amount of intensity change in this linear region provided

$$V << V_{\pi} \tag{2-41}$$

Figure (2-9) shows graphically how variations in the applied voltage will cause a linearly related intensity modulation in the output of the system.

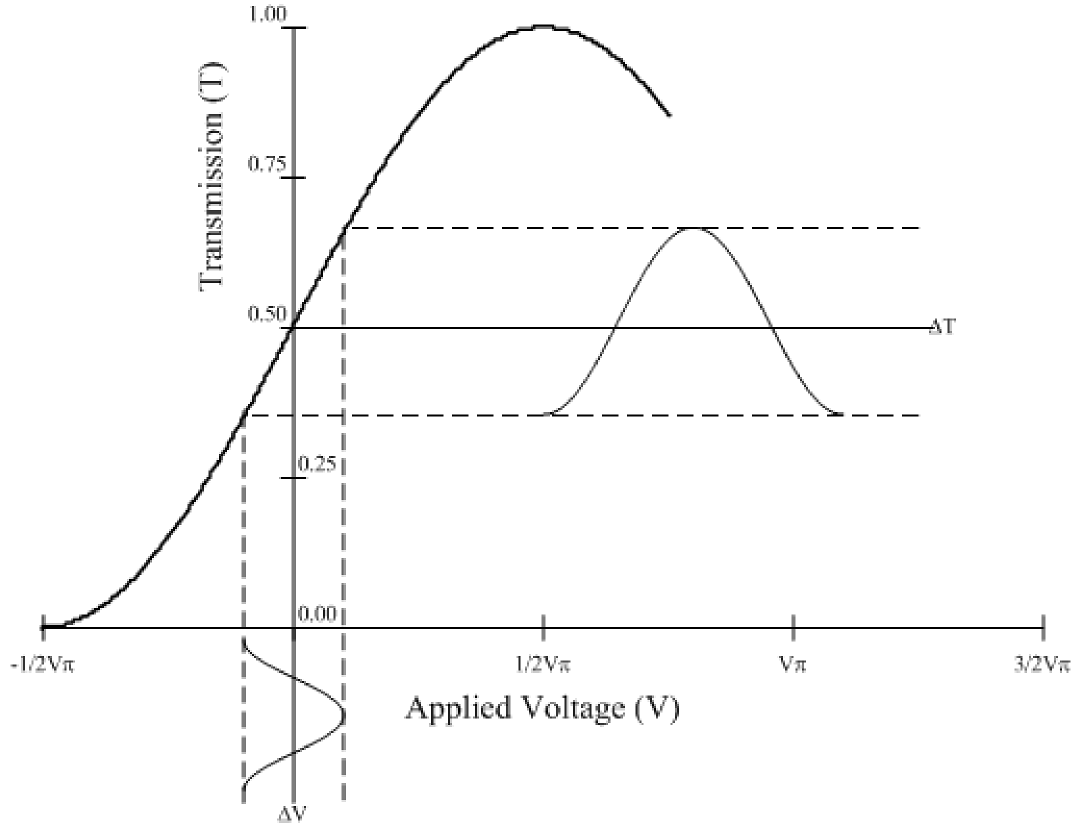

Figure (2-9) – Intensity modulation due to electric field variation

With the proper optical delivery and collection system, a functional voltage sensor can be fabricated from a biased amplitude modulator.

CHAPTER 3

SENSOR DESIGN

Sensor Requirements

There are many different ways to configure a voltage sensor using a biased amplitude modulator. Several different factors will ultimately determine the configuration used. Regardless of which is chosen, the electro-optic Pockels cell voltage sensor must have five major components in order to function properly. The first obvious part of the voltage sensor is the Pockels cell itself with two functional electrodes. Second, additional polarization optics are needed to convert the phase changes from the Pockels cell into amplitude changes. This may or may not require a biasing waveplate, depending on your needs. The third part of the voltage sensor is the light delivery and collection system. For the sensor to work properly, collimated light must be sent through the sensor and collected after it has been modulated. The fourth and fifth parts of the voltage sensor deal with the light itself. A suitable light source and detector are required in order to make a functional sensor. An ideal light source for most electro-optic voltage sensors would be a stable single frequency laser with the appropriate wavelength and power. The ideal detector would be a shot noise limited receiver capable of measuring the modulated light with the appropriate speed and sensitivity. As long as these five major components are present, an electro-optic voltage sensor can be realized.

Fiber Optic Collimator

A light delivery and collection system utilizing fiber optics is in many cases very useful. It safely transmits the laser light to and from the sensor; however, in order to properly modulate the light traveling through the voltage sensor, it must be collimated, and the light from the end of a bare fiber is not.

Many different techniques exist for collimating light from a fiber optic cable. The technique we used is shown in Figure (3-1) and consists of 100/140 μm multi-mode optical fiber, a fiber optic ferrule, a support collar and a gradient index (GRIN) lens. A GRIN lens is a rod of material in which the index of refraction changes radially from the center of the lens outward. This continuum of index changes results in a gradual "bending" of a light beam entering one end of the lens.(28) The total amount of "bending" is a function of the size of the lens itself and the radial variation of the refractive index. The index of refraction of a GRIN lens as a function of radial distance is given by

$$n(r) = n_o\left(1 - \frac{A}{2}r^2\right) \tag{3-1}$$

where n_o is the refractive index of the lens directly in the center, r is the radius of the lens and A is a positive constant relating to the rate of change of the refractive index. A ray of light that enters the GRIN lens travels inside the lens upon a sinusoidal path that has a period P given by

$$P = \frac{2\pi}{\sqrt{A}} \tag{3-2}$$

In order for the light to be collimated, the lens must be of a certain length such that the light travels along ¼ of its sinusoidal path. A GRIN lens with this length is called a quarter pitch or quarter period lens. This quarter pitch GRIN lens will act as a collimator if spatially diverging light, such as that from the end of a fiber, is placed at one end. The reciprocal is also true: if a collimated beam of light returns through the GRIN lens collimator, it will be focused into the fiber at the other end.

A simple single element glass lens refracts light based upon the lens' shape and index of refraction. A GRIN lens refracts light by a gradual change in the refractive index of the lens. Because of this refractive index gradient, the wavelength of the light passing through the GRIN lens has a significant impact on the performance of the lens as a collimator. A quarter pitch GRIN lens at one wavelength will not be a quarter pitch GRIN lens at a different wavelength and instead of collimating the light, the lens will either diverge or focus the light as it exits the lens.

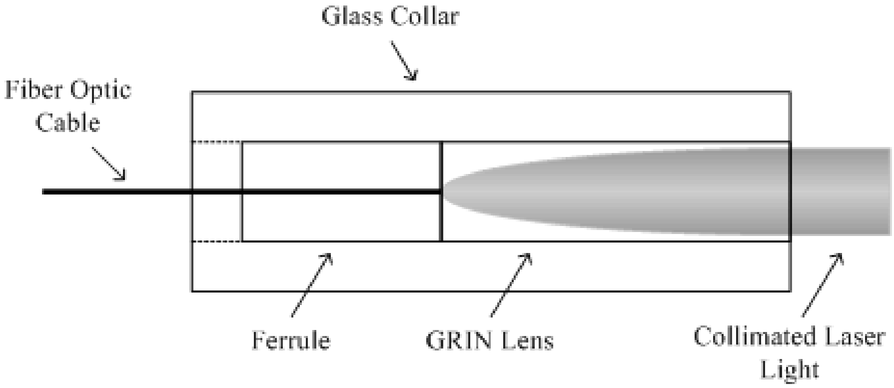

Figure (3-1) – GRIN lens fiber optic collimator

Sensor Configurations

Figure (2-7) implies the light traveling through the biased amplitude modulator travels in only one direction. This does not have to be the case. A bi-directional sensor can be built if a mirror is placed at the far end of the biased amplitude modulator so that the light is reflected back through the Pockels cell and polarization optics. With this double-pass sensor, the polarization state of the light within the Pockels cell is different from the single-pass sensor.

For a single-pass sensor the light is polarized by the first linear polarizer and is converted into circular polarization by the quarter waveplate. The Pockels cell then adds or subtracts phase from the circularly polarized light to form some amount of elliptical polarization. This polarization is analyzed by a second linear polarizer and the phase information is converted into amplitude information.

For the double-pass configuration, the second linear polarizer is replaced by a mirror. The initial linear polarizer in the sensor now also acts as the analyzer for the system. Reflection off of the mirror changes the handedness of the elliptical polarization and the second pass through the Pockels cell adds to this ellipticity. This is a nice benefit because it doubles sensor sensitivity. Unfortunately when the doubly elliptical light passes through the quarter waveplate again, the quadrature biasing of the transmission curve is lost. When the light arrives at the linear polarization analyzer we have twice the biasing we would like, which washes out much of the modulated phase acquired in the Pockels cell. To correct this, we must replace the quarter waveplate with an eighth waveplate. This ensures we remain at the quadrature point of operation by giving us a round trip total birefringence equal to the quarter waveplate. The double-pass biased amplitude modulator configuration is shown in Figure (3-2).

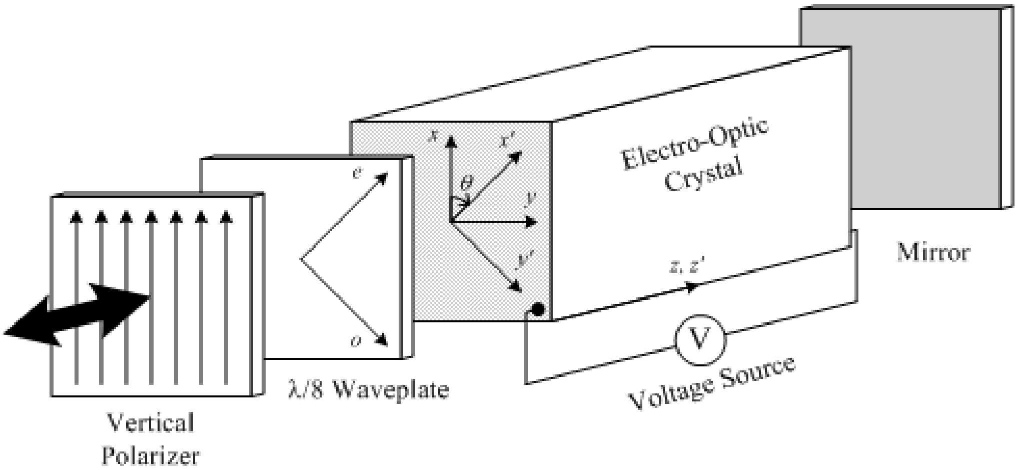

Figure (3-2) – Double-pass biased amplitude modulator #1

This sensor configuration slightly modifies the transmission equation and curve of the modulator. Instead of a squared sine curve we now have a squared cosine curve given by

$$T = \cos^2\left(\frac{2\Gamma + 2\Phi}{2}\right) \tag{3-3}$$

where Γ is still the phase delay caused by the Pockels cell and Φ is the fixed phase shift from the waveplate. However, because of the two passes through the Pockels cell and waveplate there is now twice the phase delay for each component. Equation (3-3) can be expanded by substituting for the Pockels cell and waveplate phases.

$$T = \cos^2\left(\frac{\pi V}{V_\pi} + \frac{\pi}{4}\right) \tag{3-4}$$

Figure (3-3) shows this new transmission equation graphically.

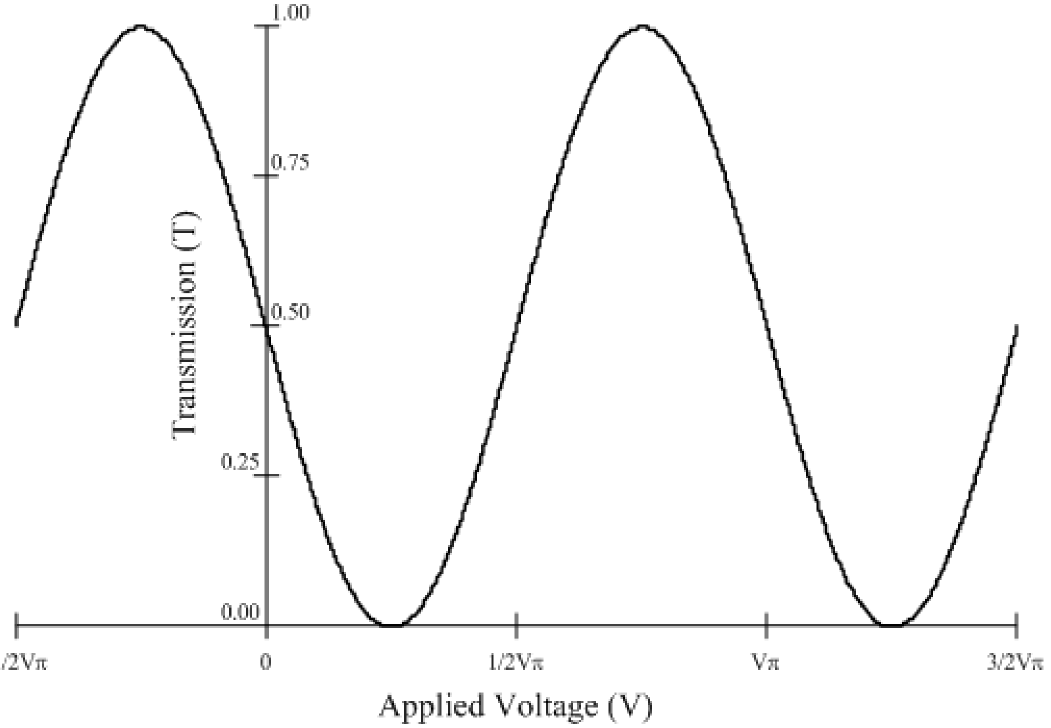

Figure (3-3) – Double-pass cosine transmission curve

As you can see from the above graph, we are still biased at the quadrature point but there is a sign change and the sensitivity of the double-pass biased amplitude modulator has changed. Figure (3-4) illustrates how the sensitivity of this configuration is higher than the configuration shown in Figure (2-7).

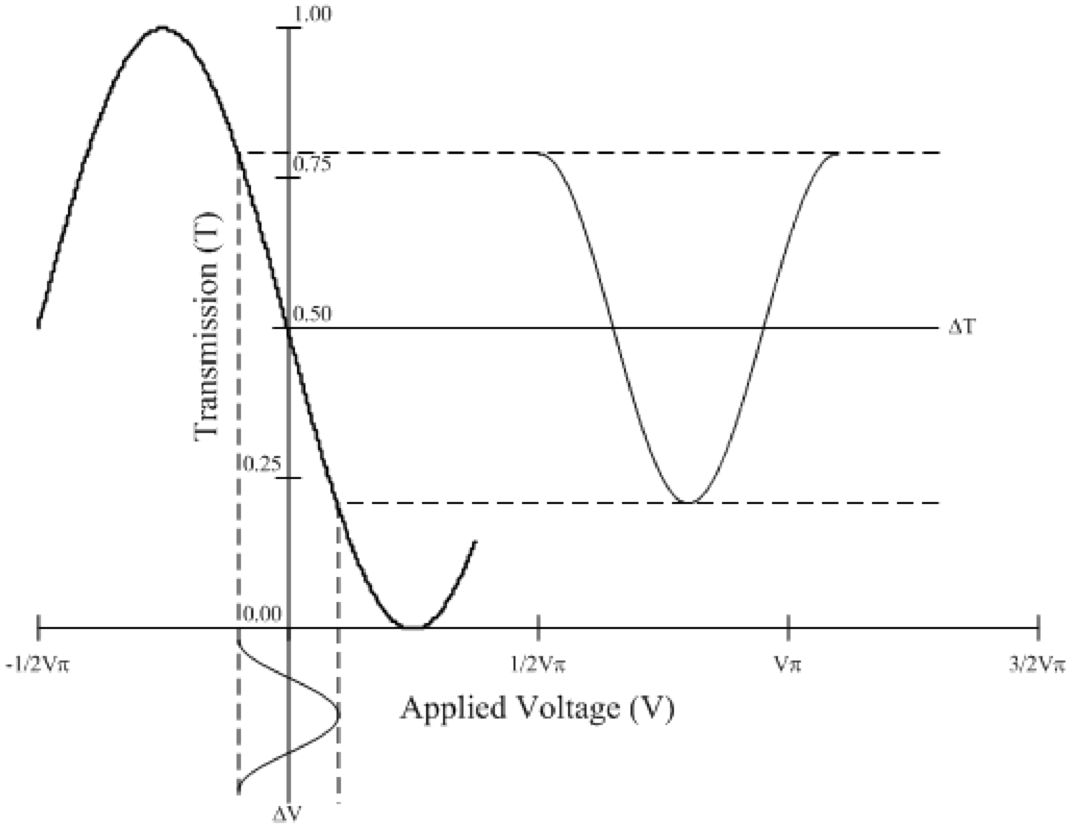

Figure (3-4) – Double-pass cosine intensity modulation

This configuration brings us back to the point made earlier about the fiber collimator having the ability to work in reverse. If we couple the light from a laser into the fiber collimator and pass the collimated light through the double-pass biased amplitude modulator shown in Figure (3-2) the still collimated but now modulated light will couple back through the collimator and travel back toward the laser source. This presents a challenge when trying to send the modulated light to a receiver. To solve this we can use a fiber optic coupler. A block diagram of this configuration is shown in Figure (3-5). The sensor design of the single collimator double-pass voltage sensor is presented in Figure (3-6).

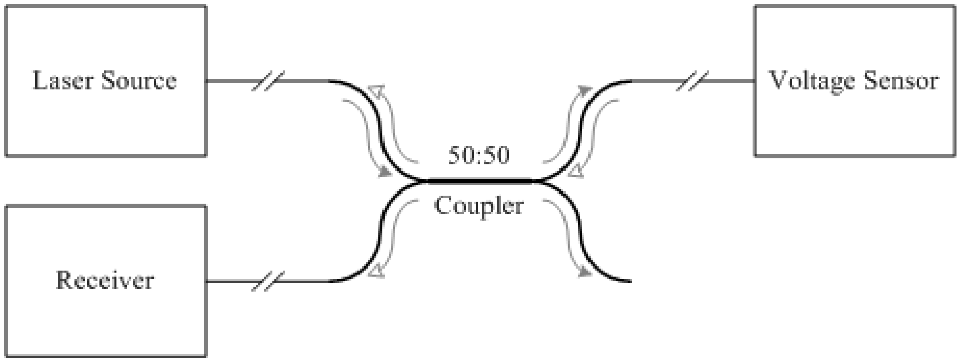

Figure (3-5) – Double-pass light delivery and collection system

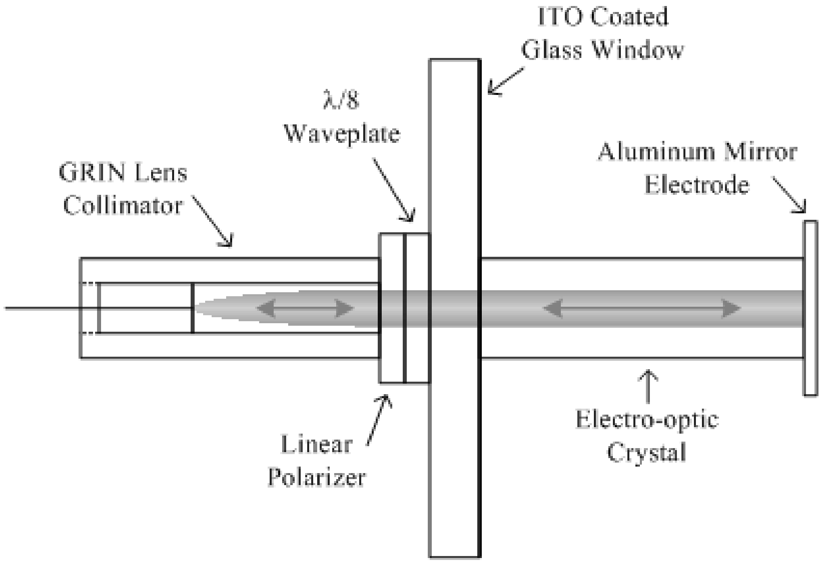

Figure (3-6) – Double-pass single collimator voltage sensor

Although this design worked, it had some problems. If we look at the amount of light lost in the system, or insertion loss, we can see that we are somewhat 'light starved'. The coupler used for this sensor system was a 100/140 μm multi-mode 50:50 fiber optic coupler, meaning that half of the light entering one leg would be split equally between the two output legs. This also means that any light returning through the output legs of the coupler would be split between the two input fibers. Note the diagram of the bi-directional coupler in Figure (3-5).

We can add up the throughput losses throughout the system to evaluate this design. Losses in the system can mostly be attributed to splitting loss, absorption loss and index mismatch or Fresnel loss. To simplify the calculations we assume there are negligible coupling losses in the system. The numerical aperture of the 100/140 μm multi-mode optical fiber used in the collimator is approximately 0.29. The numerical aperture of the GRIN lens is approximately 0.46 for a 3 mm diameter GRIN lens. Since the numerical aperture of the GRIN lens is larger than the NA of the fiber, we assume perfect coupling can be achieved. The GRIN lens is also capable of maintaining nearly perfect collimation for a minimum of 25 mm. The optical path length of the sensor is on that order, therefore light returning to the GRIN lens is assumed to be collimated. We have summarized the losses in sensor design #1 in Table (3-1) and make the statement that the sensor loss is separate from the system loss. The system loss would include coupling efficiency from the laser source to the fiber optic coupler and from the fiber optic coupler to the photo receiver.

The major sources of loss in design #1 come from the fiber optic coupler and the polarizer. On each pass through the fiber optic coupler we split our light intensity in half. We loose another 50% from the first pass through the linear polarizer if we assume the light entering the sensor is unpolarized. The two passes through the waveplate transform the linearly polarized light into circular polarization and when it passes through the linear polarizer again we loose another 50% of our light intensity.

Loss Mechanism *	Loss Type	n1	n2	% Loss	dB Loss
50:50 Coupler	Splitting	-	-	50.00%	-3.01
50:50 Coupler	Absorption	-	-	10.00%	-0.46
1 Meter of Optical Fiber	Absorption	-	-	0.05%	0.00
Optical Fiber – GRIN Lens	Fresnel	1.4860	1.6165	0.18%	-0.01
GRIN Lens	Absorption	-	-	11.00%	-0.51
GRIN Lens – Polarizer	Fresnel	1.6165	1.6500	0.01%	0.00
Polarizer	Splitting	-	-	50.00%	-3.01
Polarizer	Absorption	-	-	2.00%	-0.09
Polarizer – Waveplate	Fresnel	1.6500	1.5309	0.14%	-0.01
Waveplate – Glass Window	Fresnel	1.5309	1.5030	0.01%	0.00
Glass Window – ITO Coating	Fresnel	1.5030	1.9500	1.68%	-0.07
ITO Coating	Absorption	-	-	17.00%	-0.81
ITO Coating – BGO Crystal	Fresnel	1.9500	2.0500	0.06%	0.00
Aluminum Mirror	Absorption	-	-	11.00%	-0.51
BGO Crystal – ITO Coating	Fresnel	2.0500	1.9500	0.06%	0.00
ITO Coating	Absorption	-	-	17.00%	-0.81
ITO Coating – Glass Window	Fresnel	1.9500	1.5030	1.68%	-0.07
Glass Window – Waveplate	Fresnel	1.5030	1.5309	0.01%	0.00
Waveplate – Polarizer	Fresnel	1.5309	1.6500	0.14%	-0.01
Polarizer	Splitting	-	-	50.00%	-3.01
Polarizer	Absorption	-	-	2.00%	-0.09
Polarizer – GRIN Lens	Fresnel	1.6500	1.6165	0.01%	0.00
GRIN Lens	Absorption	-	-	11.00%	-0.51
GRIN Lens – Optical Fiber	Fresnel	1.6165	1.4860	0.18%	-0.01
1 Meter of Optical Fiber	Absorption	-	-	0.05%	0.00
50:50 Coupler	Splitting	-	-	50.00%	-3.01
50:50 Coupler	Absorption	-	-	10.00%	-0.46
* Index and loss data from datasheets				Total	-16.45

Table (3-1) – Sensor design #1 approximate losses at 1319 nm

If we add up all of the estimated losses of the double-pass single collimator voltage sensor, we find that the insertion loss is approximately 16.45 db. This means that if 100 mW of optical power were sent into the fiber optic coupler, we would only receive about 2.3 mW. This high amount of loss prompted a redesign of the double-pass single collimator voltage sensor.

The redesign prompted the replacement the single fiber optic collimator with two collimators. This required additional optics but allowed the lossy fiber coupler to be removed from the system. The major changes to the optics in the sensor came about by replacing the linear polarizer. Instead of the sheet polarizer used in the first design, a polarizing beamsplitter cube was implemented. This concept is presented below in Figure (3-7).

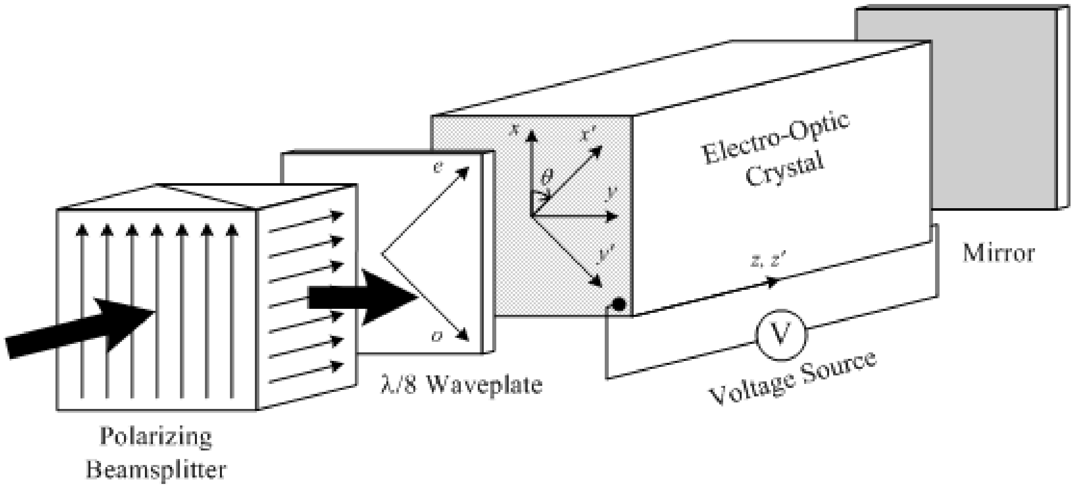

Figure (3-7) – Double-pass biased amplitude modulator #2

The replacement of the linear polarizer with the beamsplitting polarizer causes the polarization state of the light within the sensor to behave in a manner similar to the biased amplitude modulator in Figure (2-8) but with twice the Pockels cell phase. The incoming light from the source collimator is linearly polarized by the beam splitting cube. The light is then converted to elliptical polarization by the waveplate and then to circular polarization after traveling through the Pockels cell and waveplate again. The beamsplitting cube again linearly polarizes the light and sends it 90° to the side. Half of the light does travel back into the input collimator, but we are more interested in collecting the light that is reflected by the cube. A 90° prism, attached to the beam splitting cube, re-directs the light parallel to the input beam, where a second collimator collects the light and sends it to the receiver. Because the polarization analyzer is oriented 90° to the initial polarizer, the transmission curve is 180° out of phase from that of Figure (3-3). The equation that describes the behavior of the voltage sensor configuration shown in Figure (3-7) is given as

$$T = \sin^2\left(\frac{\pi V}{V_\pi} + \frac{\pi}{4}\right) \tag{3-5}$$

and is shown graphically below by Figures (3-8) and (3-9). A block diagram of a double-pass dual collimator voltage sensor is presented in Figure (3-10).

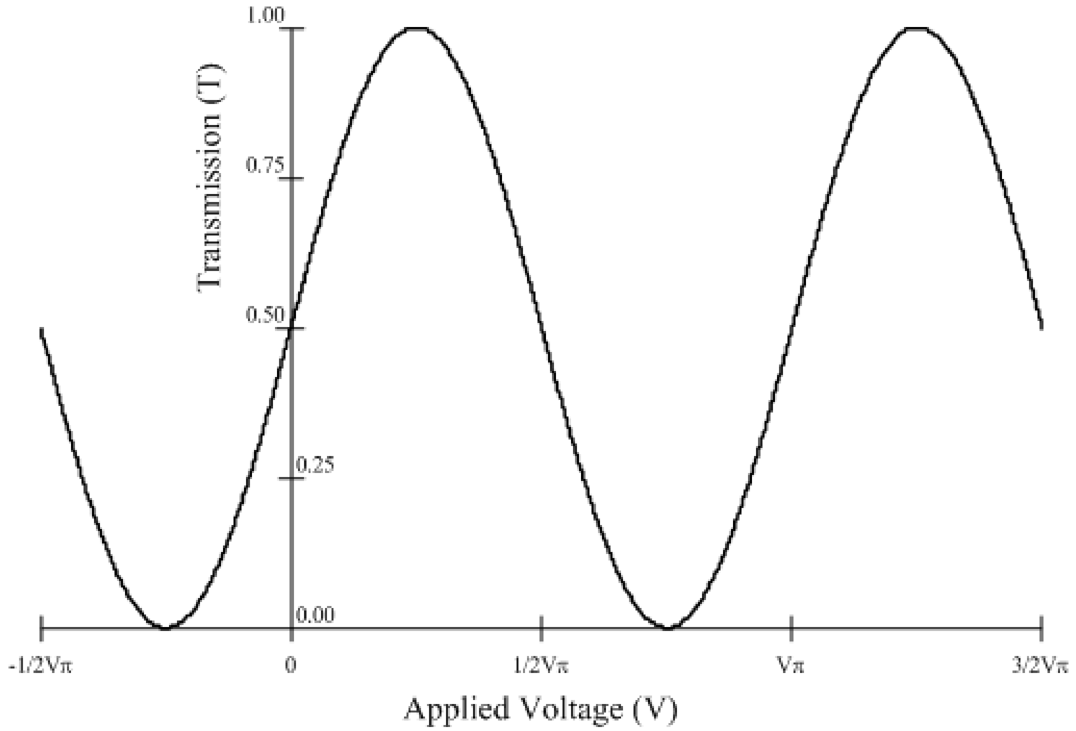

Figure (3-8) – Double-pass sine transmission curve

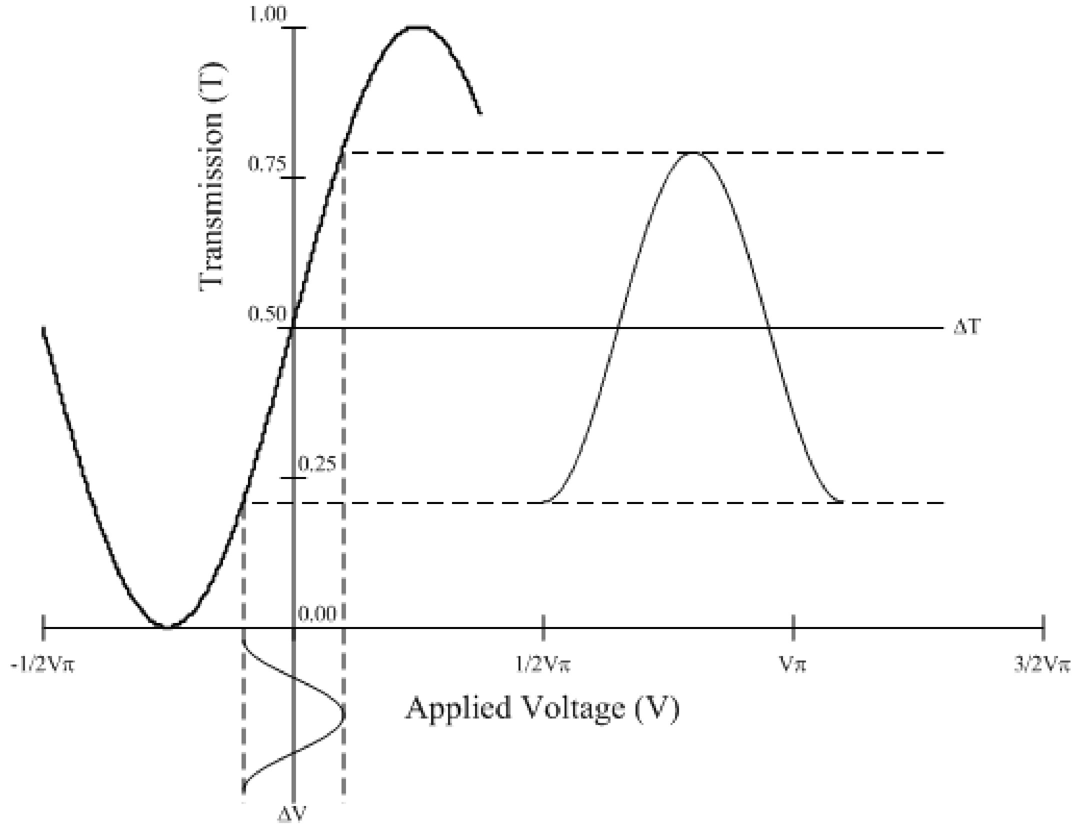

Figure (3-9) – Double-pass sine intensity modulation

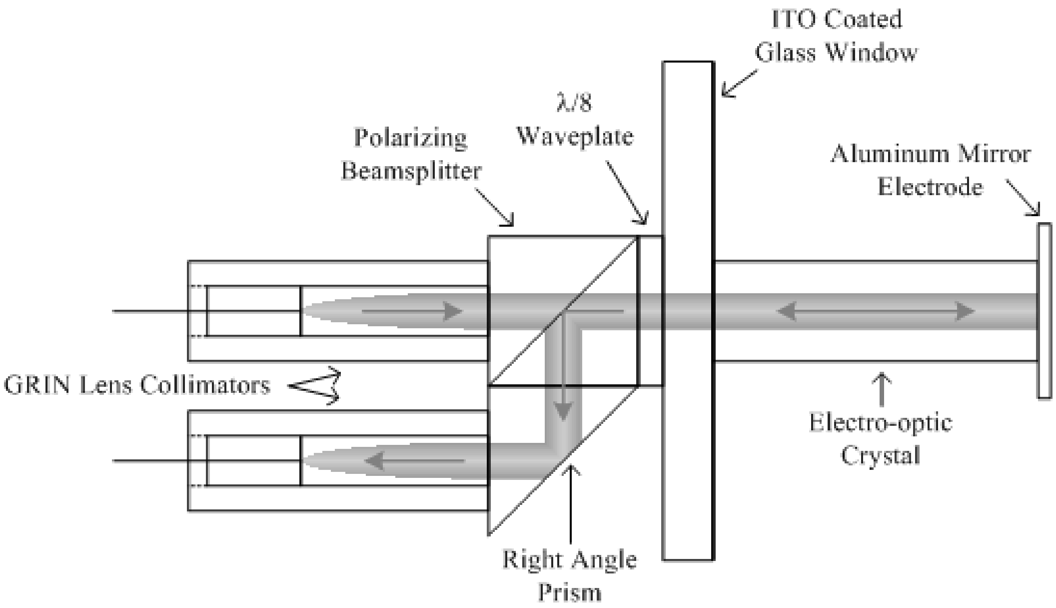

Figure (3-10) – Double-pass dual collimator voltage sensor

The above configuration works well in that there is now at least 6 db less of intrinsic loss in the system, attributed to the removal of the 50:50 fiber optic coupler. Table (3-2) summarizes the losses of sensor design #2 with the same assumptions given above for the losses in sensor design #1.

Loss Mechanism *	Loss Type	n1	n2	% Loss	dB Loss
1 Meter of Optical Fiber	Absorption	-	-	0.05%	0.00
Optical Fiber – GRIN Lens	Fresnel	1.4860	1.6165	0.18%	-0.01
GRIN Lens	Absorption	-	-	11.00%	-0.51
GRIN Lens – Polarizer	Fresnel	1.6165	1.6500	0.01%	0.00
Polarizer	Splitting	-	-	50.00%	-3.01
Polarizer	Absorption	-	-	2.00%	-0.09
Polarizer – Waveplate	Fresnel	1.6500	1.5309	0.14%	-0.01
Waveplate – Glass Window	Fresnel	1.5309	1.5030	0.01%	0.00
Glass Window – ITO Coating	Fresnel	1.5030	1.9500	1.68%	-0.07
ITO Coating	Absorption	-	-	17.00%	-0.81
ITO Coating – BGO Crystal	Fresnel	1.9500	2.0500	0.06%	0.00
Aluminum Mirror	Absorption	-	-	11.00%	-0.51
BGO Crystal – ITO Coating	Fresnel	2.0500	1.9500	0.06%	0.00
ITO Coating	Absorption	-	-	17.00%	-0.81
ITO Coating – Glass Window	Fresnel	1.9500	1.5030	1.68%	-0.07
Glass Window – Waveplate	Fresnel	1.5030	1.5309	0.01%	0.00
Waveplate – Polarizer	Fresnel	1.5309	1.6500	0.14%	-0.01
Polarizer	Splitting	-	-	50.00%	-3.01
Polarizer	Absorption	-	-	2.00%	-0.09
Polarizer – Prism	Fresnel	1.6500	1.5200	0.17%	-0.01
Prism – GRIN Lens	Fresnel	1.5200	1.6165	0.09%	0.00
GRIN Lens	Absorption	-	-	11.00%	-0.51
GRIN Lens – Optical Fiber	Fresnel	1.6165	1.4860	0.18%	-0.01
1 Meter of Optical Fiber	Absorption	-	-	0.05%	0.00
				Total	-9.53

* Index of refraction and absorption loss data obtained from datasheets

Table (3-2) - Sensor design #2 approximate losses at 1319 nm

If we add up all of the estimated losses of the double-pass dual collimator voltage sensor, we find that the insertion loss is approximately 9.53 db. This means that if 100 mW of optical power were sent into the sensor, we would receive about 11 mW. This is an improvement in the insertion loss of the sensor of about five times when compared to the first sensor design

The polarization state of the light passing through each of these sensor configurations can be mathematically described using Jones calculus. This work is given in the Appendix at the end of this thesis.

Working prototype BGO and ZnSe voltage sensors were fabricated using the technique described in the first part of this chapter, specifically the configuration shown in Figure (3-6). A photo of a BGO prototype voltage sensor is presented below in Figure (3-11).

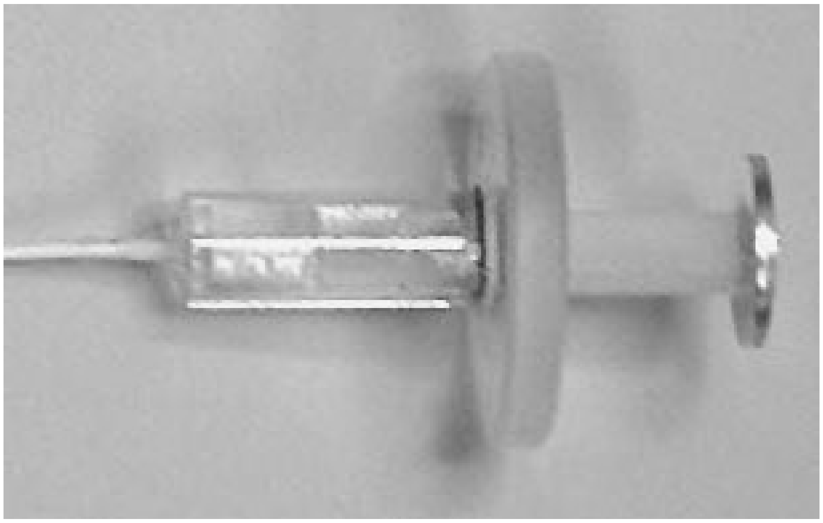

Figure (3-11) – Prototype BGO voltage sensor (design #1)

Working prototype BGO and BSO voltage sensors utilizing the second technique, as shown in Figure (3-10), were also fabricated. A photo of a BGO prototype voltage sensor using the second design is presented in Figure (3-12).

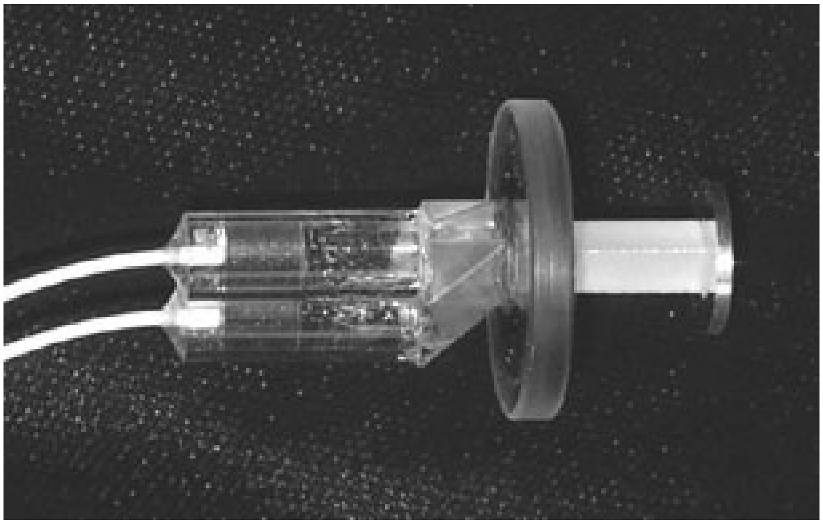

Figure (3-12) – Prototype BGO voltage sensor (design #2)

Sensor Implementation

The primary use of these electro-optic voltage sensors is to determine the position of the electron beam in relation to the center of the beam pipe. This is accomplished by mounting four sensors around the perimeter of the beam pipe in the same configuration described for the B-dot beam position monitor in the introduction. Figure (3-13) shows the configuration for four electro-optic sensors working as a beam position monitor (BPM).

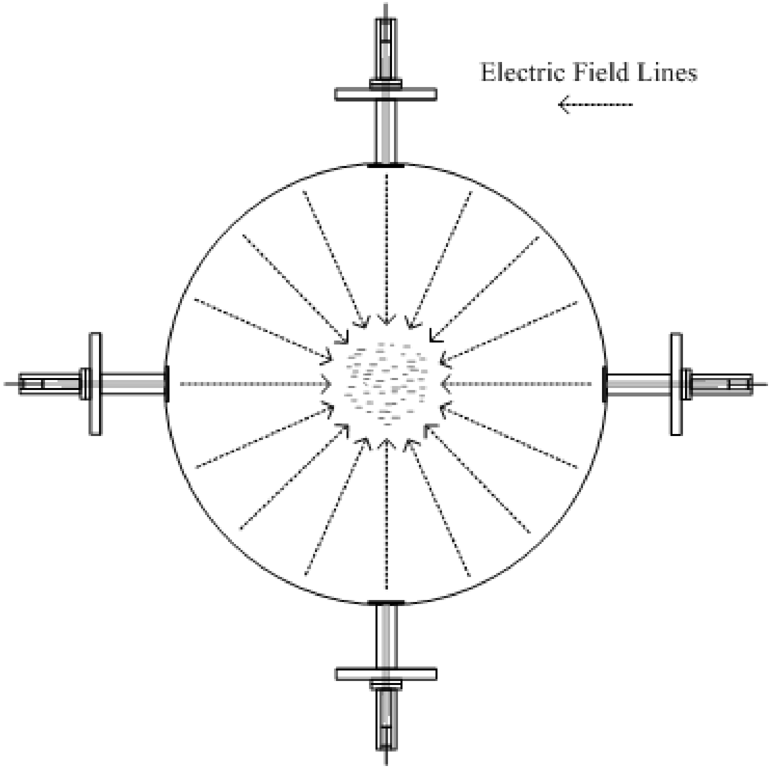

Figure (3-13) – Electro-optic beam position monitor

As the electron beam passes through the center of the BPM it will induce the exact same signal on each calibrated voltage sensor. If the beam is not directly in the center of the BPM, the electron beam to sensor electrode capacitance will not be the same for each sensor and as such they will measure different beam voltages. This leads to a difference in calibrated sensor output and can be converted into a position reading of the beam location within the accelerator pipe. Electro-optic voltage sensors, utilizing sensor design #2 and operating at 1319 nm, have been adopted by Los Alamos National Labs and work is ongoing to incorporate these sensors as beam position monitors for the second axis of DARHT. Prototype sensor results and beam position monitor work has been reported in the literature.(12,13,14,15)

Sensor Voltage

Now that we have looked at how voltage sensors are used on an electron particle accelerator, we can look at how they really work. Figure (3-14) shows the location of a voltage sensor to the electron beam of an accelerator. A special housing is used to physically support, maintain vacuum, and align and protect the voltage sensor as it interfaces with the accelerator wall, commonly referred to as the beam pipe. Numerous housing designs have been reported in the literature.(12,13,14,15)

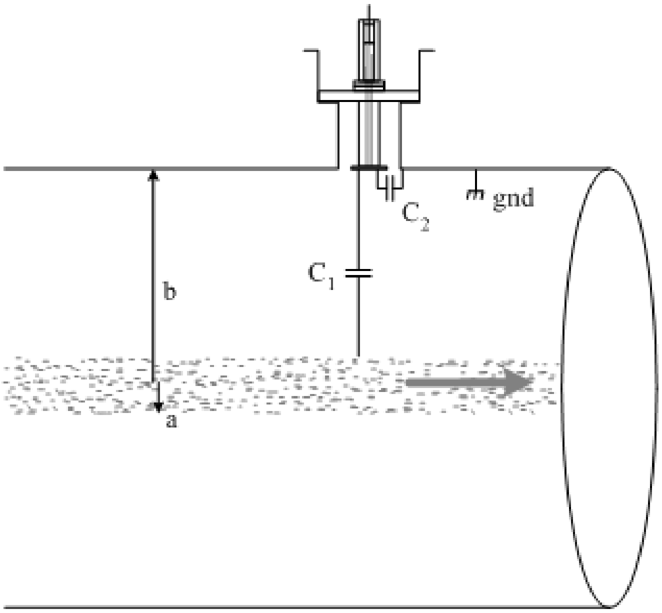

Figure (3-14) – Electro-optic voltage sensor mounted on accelerator

To describe how the sensor actually 'senses' the electrons as they pass beneath the electrode of the Pockels cell, we start by making a few assumptions. We shall approach this problem electro-statically and shall think of the electrons as frozen in time. Each electron has an individual charge, q, associated with it and we can relate this charge to the electric field created by the particle using Coulomb's law.

$$E = \frac{q}{4\pi \varepsilon r^2} \tag{3-6}$$

where ε is the permittivity of the medium surrounding this charge and E is the strength of the electric field created by q at a distance r.

Equation (3-6) holds for the case of a single electron. In an accelerator there is a long stream of many electrons. We shall assume that to the sensor, this long stream can be considered to be infinitely long. If we do this, we can use Gauss' law for an infinitely long line of charge to determine the strength of the electric field created at a Gaussian cylinder of radius r.

$$E = \frac{q_l}{2\pi \varepsilon_o r} \tag{3-7}$$

where q_l is the charge density of the beam, assumed to be uniform and constant, and ε_o is the permittivity of free space. We note that for the geometry assumed, the electric field strength is inversely proportionate to distance. The direction of the electric field is graphically shown in Figure (3-13). Equation (3-7) gives the electric field strength at the wall of the beam pipe due to the electron beam. We are able to determine the electric potential at the wall of the beam pipe if we integrate the electric field from the edge of the electron beam to the pipe wall.

$$V = -\int_a^b E \cdot dr \tag{3-8}$$

and upon substitution

$$V = -\int_a^b \frac{q_l}{2\pi\varepsilon_o r} \cdot dr \tag{3-9}$$

We are able to move part of the expression outside of the integral to get

$$V = -\frac{q_l}{2\pi\varepsilon_o} \int_a^b \frac{1}{r} \cdot dr \tag{3-10}$$

which evaluates to

$$V = -\frac{q_l}{2\pi\varepsilon_o} \ln(r)\Big|_a^b \tag{3-11}$$

and becomes

$$V = \frac{q_l}{2\pi\varepsilon_o} \left[\ln(b) - \ln(a)\right] \tag{3-12}$$

We are finally left with the expression for the electric potential between the beam pipe and the electron beam.

$$V = \frac{q_l}{2\pi\varepsilon_o} \ln\left(\frac{b}{a}\right) \tag{3-13}$$

where *a* and *b* are the radius of the electron beam and beam pipe respectively. The wall of the beam pipe is typically grounded, thus Equation (3-13) is an expression for the electric potential, or voltage, of the electron beam.

As the electrons travel down the accelerator pipe and pass under the electrode of the sensor, their charge is capacitivly coupled to the sensor electrode. The geometry of the system shown in Figure (3-14) determines the beam to electrode capacitance, C_1 and the electrode to ground capacitance, C_2. They form a capacitive divider circuit from the electron beam to ground through the sensor electrode. We are able to determine the induced voltage on the sensor electrode by the following equation.$^{(13)}$

$$V_{electrode} = \left({C_1}\middle/{C_2} \right) V_{beam} \tag{3-14}$$

where Equation (3-13) gives the electron beam voltage.

We are able to relate the electron beam voltage to the beam current by defining the charge density as

$$q_l = \frac{I_{beam}}{\beta c} \tag{3-15}$$

where I_{beam} is the beam current, c is the speed of light and β is the relativistic speed factor of the electron beam. Substitution of this equation into Equation (3-13) yields

$$V_{beam} = \frac{I_{beam}}{2\pi\varepsilon_o \beta c} \ln\left(\frac{b}{a}\right) \tag{3-16}$$

By substituting Equation (3-16) into Equation (3-14), we are now able to give the relationship between the induced sensor electrode voltage and the current of the electron beam.

$$V_{electrode} = \left({}^{C_1}\!\!/_{C_2} \right) \frac{I_{beam}}{2\pi\varepsilon_o \beta c} \ln\left(\frac{b}{a}\right) \tag{3-17}$$

The geometry of the sensor and its housing was designed such that approximately 2 kA of beam current would induce between 500 V and 2 kV on the electrode of the sensor, given a particular accelerator configuration.(14) Finite element modeling of the system capacitances for the second axis of DARHT was performed by M. Brubaker of LANL and yielded an expected sensor electrode voltage of 1.5 kV for a beam current of 2 kA.(15) This induced voltage is within the nominal design range of the sensor.

We shall now use a simplified second approach to determine a first approximation of the induced voltage on the sensor electrode. We begin by using Equations (3-7) & (3-15) to give an expression of the electric field strength at the wall of the accelerator beam pipe for a given beam current.

$$E = \frac{I_{beam}}{2\pi\varepsilon_o r \beta c} \tag{3-18}$$

We remember that the electric flux density, *D*, is related to the electric field strength by

$$D = \varepsilon E \tag{3-19}$$

where $\varepsilon = \varepsilon_o$ for the vacuum of the accelerator. This relationship allows us to determine the electric flux density at the wall of the accelerator pipe.

$$D_{pipe} = \frac{I_{beam}}{2\pi r \beta c} \tag{3-20}$$

If we make the assumption that the D-field is continuous from the inside of the accelerator pipe through the electro-optic crystal of the sensor, we can write the following.

$$D_{crystal} = D_{pipe} \tag{3-21}$$

which leads to

$$D_{crystal} = \frac{I_{beam}}{2\pi r \beta c} \tag{3-22}$$

We can now use the relationship given in Equation (3-19) to write the expression for the electric field strength across the electro-optic crystal of the sensor.

$$E_{crystal} = \frac{I_{beam}}{2\pi r \varepsilon_{crystal} \beta c} \tag{3-23}$$

where $\varepsilon_{crystal} = \varepsilon_r \varepsilon_o$. If we integrate the electric field from one end of the crystal to the other, we can find the voltage potential across the crystal. This integration simply yields

$$V_{crystal} = E_{crystal} L \tag{3-24}$$

where L is the length of the electro-optic crystal. The voltage across the electro-optic crystal is equal to the induced voltage on the electrode of the sensor, thus

$$V_{electrode} = \frac{I_{beam} L}{2\pi r \varepsilon_{crystal} \beta c} \tag{3-25}$$

This expression does not take into account the finite dimensions of the actual sensor, save the length of the crystal. It gives the voltage on the electrode of a tube of sensor material around the outside of the beam pipe due to the assumptions used for the Gaussian expression of the electric field in Equation (3-7). Finite element modeling can be used to factor in the boundary conditions of a finite sensor and obtain a more accurate value of the induced electrode voltage.

We can use Equation (3-25) to calculate a rough first approximation of the expected voltage induced on the electrode of the sensor. The second axis of DARHT has a relativistic beam of electrons traveling down a 10” beam pipe with a current of 2 kA. The electro-optic crystal of the sensor has a length of 1 cm and a relative permittivity of 16. This configuration yields an induced electrode voltage of approximately 590 V. This value still falls within the design criteria for the sensor and one would expect this value to increase when the geometry of a finite sensor is taken into consideration.

Minimum Detectable Voltage

In order for the performance of the electro-optic sensor system to be comparable to current diagnostics for the second axis of DARHT, we have a signal to noise ratio (SNR) requirement of 100:1.(15) It will be shown in Chapter 5 that the optical transmission through an ideal double-pass voltage sensor of design #2 can be approximated at voltages much smaller than the half-wave voltage by the following equation.

$$T \approx \frac{1}{2}\left(1 + 2\pi \frac{V}{V_\pi}\right) \tag{3-26}$$

where V is the applied electrode voltage and T is the optical power out of the sensor divided by the optical power launched into the sensor. We shall replace the ideal loss of the sensor with the actual loss of the sensor to provide more realistic results. The ideal loss of one half is replaced by an expression relating to the dB loss of the sensor. We are now able to re-write Equation (3-26) to give an expression that allows us to calculate how much optical power will be sent to a receiver given an applied electrode voltage.

$$P_{out} \approx P_{in} 10^{\frac{-dB_{loss}}{10}}\left(1 + 2\pi \frac{V}{V_\pi}\right) \tag{3-27}$$

where dB_{loss} is the sensor loss in decibels.

For the following example we are interested in a double-pass sensor of design #2, and according to the data reported in Table (3-2) the sensor is likely to have a loss of 9.53 dB. If we assume a 1319 nm source is used with an optical power of 1 mW, we should expect to receive 111.4 μW of power when zero volts are applied to a BGO sensor with a half-wave voltage of 75 kV. If the peak beam induced voltage of 1.5 kV is applied to the electrode, we expect an optical power of 125.4 μW at the receiver. The difference between these two values is 14 μW and is the signal of interest. This signal must be 100 times larger than the noise equivalent optical power in the system if we are to maintain a SNR of 100:1.

To find the noise of the system, we start by using the expression for the photocurrent generated by a given optical signal of power, *P*.

$$i_{\lambda} = \frac{\eta P e \lambda}{hc} \tag{3-28}$$

where η is the quantum efficiency of the detector, e is the charge of an electron, λ is the wavelength of incident light, h is Planck's constant, and c is the speed of light. The shot noise photocurrent of the optical signal, which is the random variation of the arrival time of the photons of an optical signal with average power, P, is given by

$$\Delta i_{\lambda shot} = \sqrt{2 i_{\lambda} e B} \tag{3-29}$$

where B is the bandwidth of the receiver.

The optical receiver used on the second axis of DARHT to measure the return signal from the sensor is a shot noise limited receiver with a bandwidth of 100 MHz. This means that the largest source of noise in the system is due to shot noise and we can ignore all other sources of noise. We shall assume the photo-diode in the receiver has a quantum efficiency of 75%.

To continue with our example, we are looking to find the noise in the system due to a given optical signal. The maximum light we expect to receive at the photo-detector is 125.4 μW, which gives a signal current of 998.8 μA and a shot noise photocurrent of 56.53 nA. We would like to express this noise current as a function of optical input power. This expression is called the noise equivalent power (NEP) and is defined as the amount of optical power that would generate a photocurrent equal to the noise photocurrent of the system. We use Equation (3-28) and find that the NEP of our system is 71 nW at peak beam current.

We are now able to find the signal to noise ratio of our system. The expression for SNR is given as

$$SNR = \frac{\Delta I_{\max}}{NEP} \tag{3-30}$$

In order for our system to maintain a signal to noise ratio of 100:1, we need the NEP of our system to be less than or equal to 140 nW. We have just shown that our actual NEP is 71 nW and have attained a SNR of 197:1, thus meeting our 100:1

requirement. Other noise sources will ultimately affect the SNR of the system, but for the purposes of this example, shot noise was assumed to be the limiting factor.

Now that we know what the NEP of our system is, we can calculate what induced electrode voltage will give an output signal that is equal to our NEP. This induced electrode voltage is the minimum detectable voltage of the sensor. We are able to rewrite Equation (3-27) in order to calculate the minimum detectable sensor voltage.

$$P_{out-zero} + NEP \approx P_{in} 10^{\frac{-dB_{loss}}{10}} \left(1 + 2\pi \frac{V_{min}}{V_{\pi}} \right) \tag{3-31}$$

where

$$P_{out-min} = P_{out-zero} + NEP \tag{3-32}$$

We are able to rewrite Equation (3-31) to obtain a complete expression of the minimum detectable sensor voltage in terms of the NEP, V_{π}, sensor insertion loss and source output power.

$$V_{min} = \frac{\left(\dfrac{NEP}{P_{in} 10^{\frac{-dB_{loss}}{10}}} \right) V_{\pi}}{2\pi} \tag{3-33}$$

Upon substituting the known values, we find that for an NEP of 71 nW the minimum detectable sensor electrode voltage is 7.6 volts. If 1.5 kV is the maximum voltage on the electrode, we are able to detect changes in the electrode voltage on the order of 0.5%. The relationship between the induced electrode voltage and the electron beam current is proportional, meaning that a 0.5% change in beam current will induce a 0.5% change in the electrode voltage. Thus, the sensor system described in the above example is capable of detecting 0.5% changes in the electron beam current. The requirement on beam current detection for the second axis of DARHT is 2%.(15)

We are able to generate graphs of minimum detectable electrode voltage versus the half-wave voltage of a crystal using Equation (3-33). Using the examples above, we have plotted the lines that correspond to an NEP of 71 nW and 140 nW. These lines both refer to a BGO crystal system with a half-wave voltage of 75 kV. In order to meet the design criteria, a sensor system utilizing any electro-optic crystal must operate below the grey dashed line in Figure (3-15). This line refers to our requirement of 100:1 SNR or 15 volts measured with 1.5 kV applied to the sensor.

We can see from Figure (3-15) that the relationship between V_{min} and V_π is a linear one, whose slope depends upon the input optical power, sensor insertion loss and the noise equivalent power of the photo receiver. The minimum detectable induced electrode voltage is directly proportional to the noise equivalent power, thus the smaller the NEP the more sensitive the system. It is also evident that smaller values of V_π will also lead to a more sensitive system.

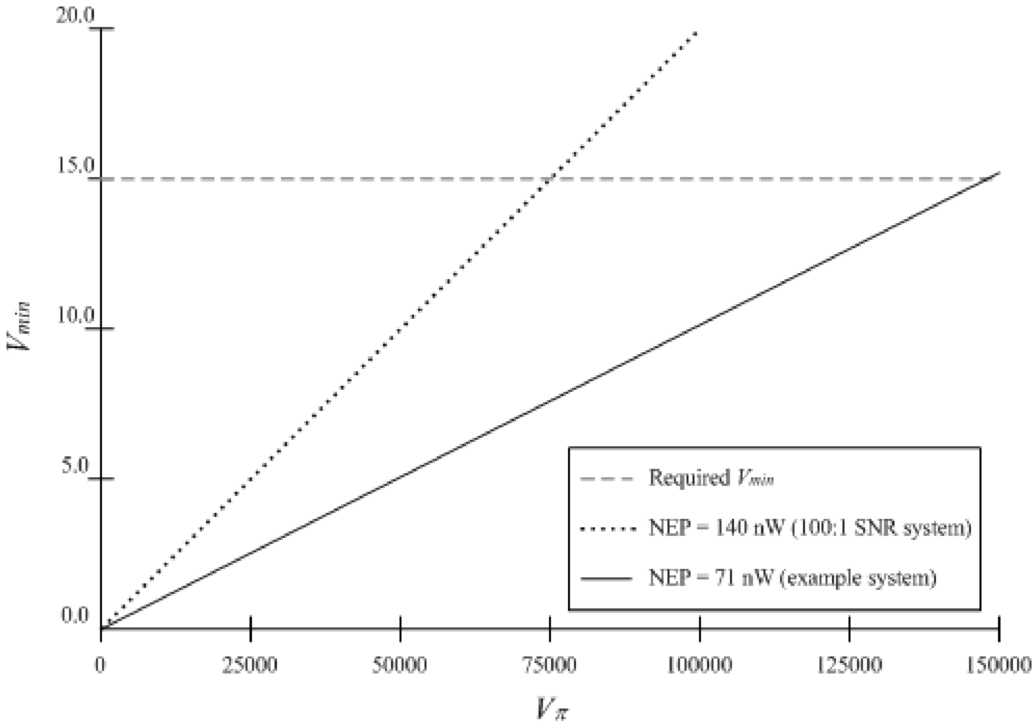

Figure (3-15) – V_π dependence of minimum detectable voltage

CHAPTER 4

EXPERIMENT

Experimental Setup

To test the sensitivity of each crystal candidate, we indirectly measured the V_π values of the crystals. Since we were primarily interested in each crystal's performance when used in an electro-optic Pockels cell voltage sensor, we did not measure the Pockels coefficients or the indexes of refraction of the crystal, just the half-wave voltage of each crystal. This was accomplished by setting up a larger scale laboratory version of a voltage sensor where the alignment of each piece was accurately controlled.

The V_π measurement experiments were performed at two different wavelengths using an 850 nm vertical cavity surface emitting laser (VCSEL) diode and a 1319 nm edge emitting light emitting diode (E-LED). Since these two wavelengths are common telecommunication wavelengths, the polarization optics needed to conduct this experiment were readily available. The experiments were performed at these two wavelengths to determine the operating wavelength that yielded the best performance.

All elements of an actual voltage sensor are present within the experimental bench top setups used to measure V_π. However, we needed to be able to change the orientation of each optical element with respect to every other piece. This was accomplished by using free space optics, multi-axis optical mounts and an optical breadboard. We mounted the polarizers and waveplate on rotation stages that gave us the ability to orient each component to the precise axes of alignment. We also needed to be able to rotate the crystal under test about its optical axis to achieve proper alignment to the waveplate and polarizers. This presented a challenge as the optical path through the crystal needed to be free from obstruction, centered along the optical axis of the system, and still provide the ability to create an electric field along the length of the crystal.

The configuration of the bench top measurement setup is very similar to the actual sensor configurations discussed in the previous chapter, with only a few exceptions. The experiments used to measure V_π utilized a single-pass and double-pass configuration and are shown in Figure (4-1) and (4-2).

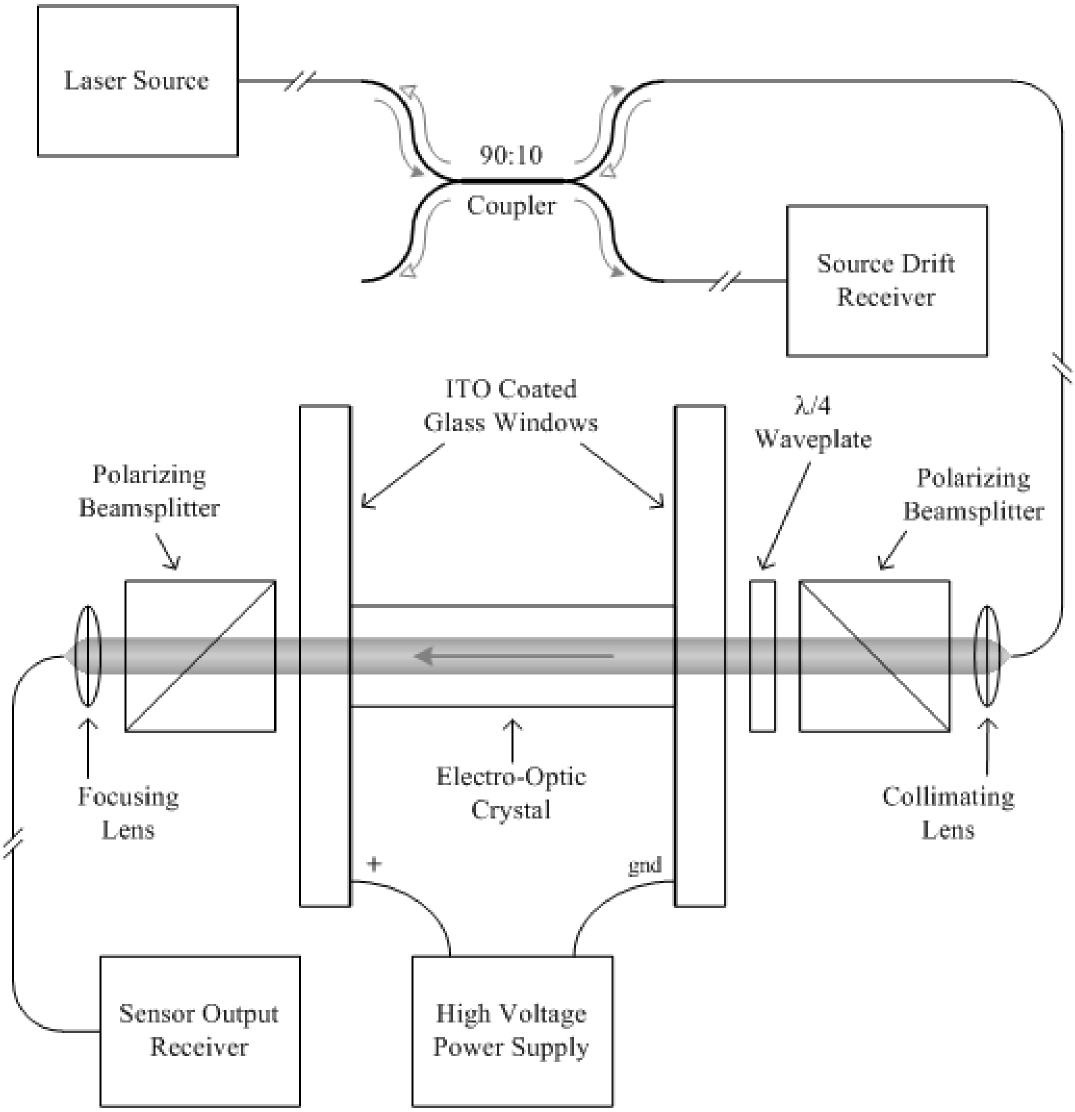

Figure (4-1) – Single-pass bench top experimental configuration

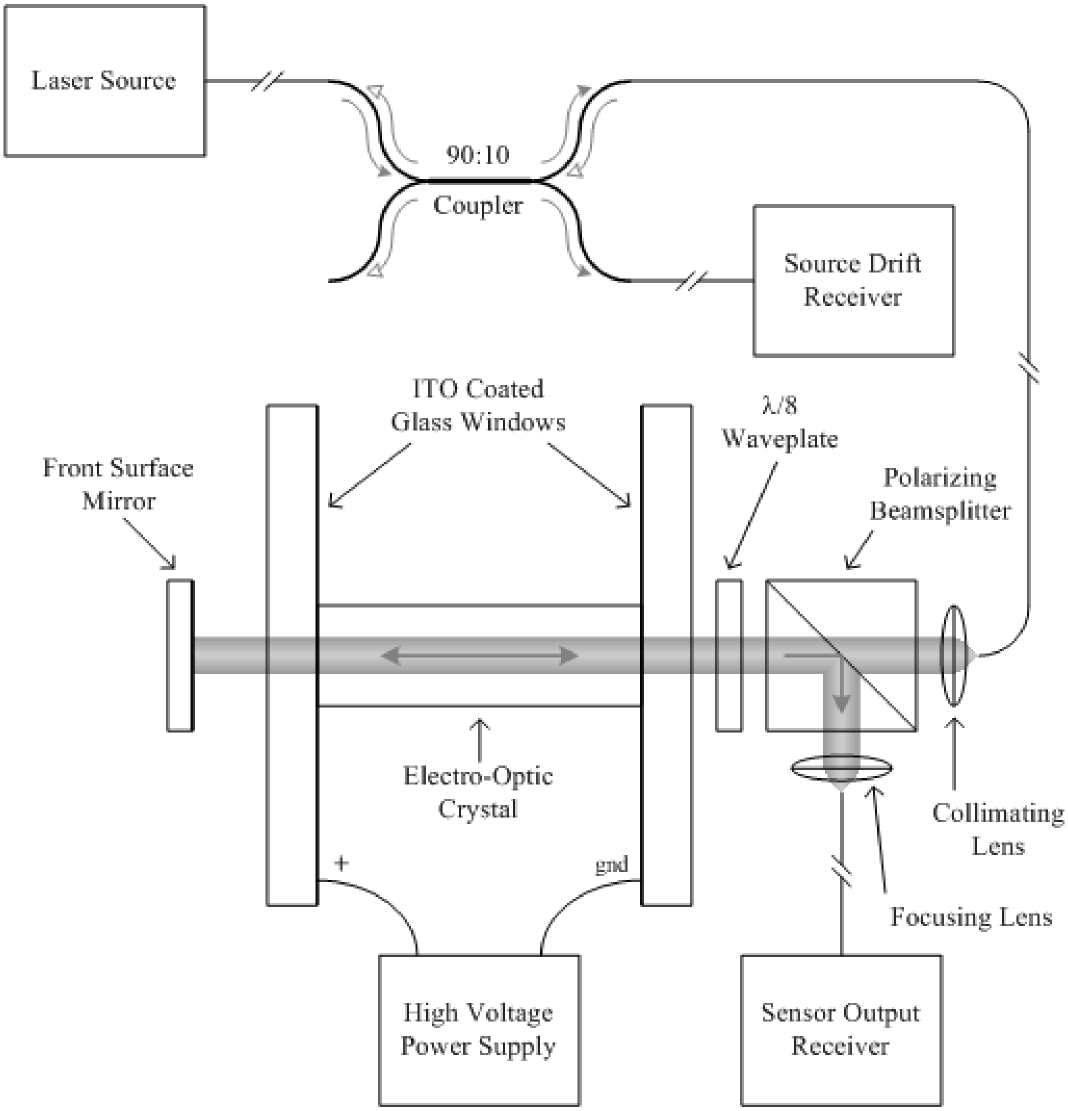

Figure (4-2) – Double-pass bench top experimental configuration

In order to test each crystal we applied a voltage to the Pockels cell and measured the optical output. The voltage source used was a Bertan 205A-01R High Voltage Power Supply that had a variable output from 0 to 1000 volts. The source was only capable of supplying 30 mA of current but the high voltage still raised a few electrical safety concerns. To mitigate any electrical danger, the entire bench top sensor experiment was constructed on a 12” x 12” optical breadboard and placed into a grounded protective enclosure. The enclosure also provided a means of minimizing stray light during the experiment.

A Pockels cell holder that could accommodate the various sample sizes, maintain a centered optical axis and be rotated about that axis, had to be implemented. A versatile crystal holder and special electrodes were designed and fabricated. The Pockels cell holder was machined out of a durable black plastic called Delrin, a material that provided electrical insulation for the electrodes but did not interfere with the electric field across the crystal under test. Figure (4-3) shows a side view of this holder.

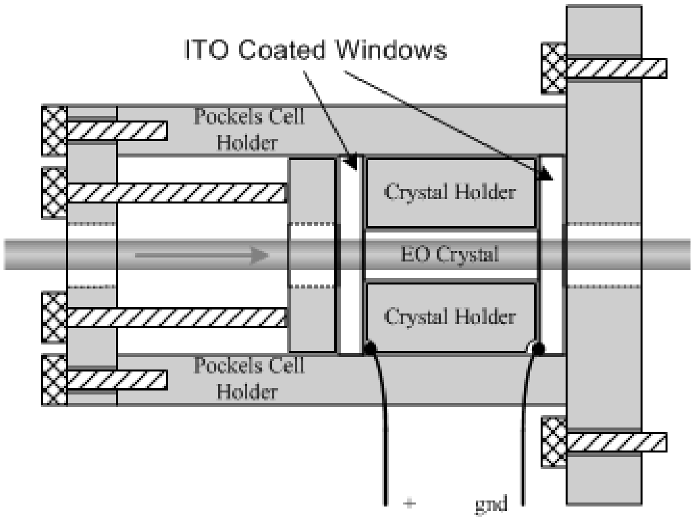

Figure (4-3) – Bench top Pockels cell holder

The Pockels cell holder has three main parts that secure the electro-optic crystal in place during the experiment. The main housing resembles a hollow tube mounted to a flat round base. This piece provides a clear optical path directly through the center of the housing while supporting and centering the entire Pockels cell along the optical axis of the experiment. A second hollow Delrin tube is also used as part of the Pockels cell holder. This one holds the electro-optic crystal itself and centers the crystal's length to the optical axis of the setup. The dimensions of each crystal holder are unique to every crystal sample it supports, with exception to the outside diameter. Each crystal holder is machined to fit inside of the Pockels cell holder. The crystal holder is then placed into the Pockels cell holder between two electrodes that create the electric field. The final piece of the Pockels cell holder is the end cap that secures everything inside of the holder. The end cap is also made from Delrin and is bolted to the sides of the support tube of the holder. It also has a hollow center to allow a clear optical path and has setscrews to hold the Pockels cell in place. Once assembled, the holder is mounted to a rotation stage to provide a means of rotating the crystal about the optical axis.

The two electrodes shown in Figure (4-3) are glass windows with one side coated by a thin layer of conductive transparent material called indium tin oxide (ITO). These windows are the same windows used in the actual sensors described in the previous chapter. Their function is to set up an electric field across the sample crystal while at the same time, providing an uninhibited optical path through the crystal. In order to create an electric field across the crystal, electrical leads were attached to the ITO coating using conductive epoxy. These leads were then connected to the high-voltage power supply by a BNC bulkhead connector mounted on the side of the enclosure.

Aspheric lenses, capable of providing good collimation at both test wavelengths, were used instead of the fiber optic GRIN lens collimators described in the previous chapter. The aspheric collimating lenses were connectorized to provide exact alignment between the end of the fiber optic cable and the lens. By utilizing these collimating lenses instead of GRIN lenses we were able to reduce setup time between experiments.

Polarizing beamsplitter cubes were used as the linear polarizers needed for the single-pass experiments and were also used to split the polarization when acting as the analyzer for the double-pass experiments. This is illustrated in Figures (4-1) and (4-2). The polarizing beamsplitter cubes were broadband coated, but not broad enough to allow the same beam splitter cube to be used at both test wavelengths. When the experiment was performed at a different wavelength, the appropriate beamsplitters were used.

Two different waveplates were used for biasing the amplitude modulator. When the experiment was set up in the single-pass configuration, a quarter waveplate was used to achieve the desired biasing. For the double-pass configuration, an eighth waveplate was used. The waveplates were very narrow band, meaning they provided their specified retardance only over a small band of wavelengths. Therefore, each time the wavelength changed in the experiment, the waveplates had to be replaced with the appropriate ones.

Alignment was critical with this test as we were trying to determine not only the correct value of V_π but also the correct orientation of the crystallographic axes of each crystal sample. Several alignment steps were required and the alignment process for the single-pass setup was different from the double-pass setup. We shall describe the single-pass alignment first.

To begin with, the two collimators were aligned to each other so that a maximum amount of light was collected by the second collimator. Care was also taken to ensure the beam path was as horizontal to the optical breadboard as possible. Second, the polarizing beamsplitter cubes were installed and aligned 90° to each other. When the two cubes were perfectly aligned, a minimum was detected at the receiver. Next, the quarter waveplate was installed between the two polarizers, leaving enough room for the Pockels cell holder.

The quarter waveplate was mounted on a rotation stage that allowed it to be rotated about the optical axis of the system. In order to provide one quarter wave of phase retardance to the incoming light, the input polarization must be aligned 45° to the ordinary and extraordinary axes. Once mounted in the beam path, the waveplate was rotated so that a minimum was detected at the receiver. This orientation did not alter the polarization of the light and coincided with the ordinary or extraordinary axis of the waveplate. The waveplate was then rotated 45°, creating circular polarization.

Finally the Pockels cell was added to the bench top sensor. The cell was placed between the waveplate and the second polarizer. With no electric field across the crystal sample, the polarization state of the incoming light should remain unchanged. Once a field is placed across the crystal, it becomes birefringent and modifies the polarization state of the light. The crystal essentially behaves like a variable waveplate, and like a waveplate, we must locate the ordinary and extraordinary axes in order to properly align it.

Finding these axes of the crystal was a tedious job. A voltage was applied to the Pockels cell and the sensor output was recorded. The Pockels cell was then rotated a few degrees from where it was previously and the sensor output was again noted. Each crystal has four poles, two positive and two negative corresponding to 45° between the birefringent axes of the crystal. When aligned to the positive poles, the optical output from the sensor would increase as the voltage was increased. When aligned to the negative poles, the output would decrease. In a cubic crystal, these poles should be 90° apart from each other, alternating positive and negative. Once one of these poles was identified, the transmission through the system was optimized by reducing refraction loss and the experiments were performed. Figure (4-4) shows the poles of a cross section of crystal in relation to the birefringent axes of the crystal.

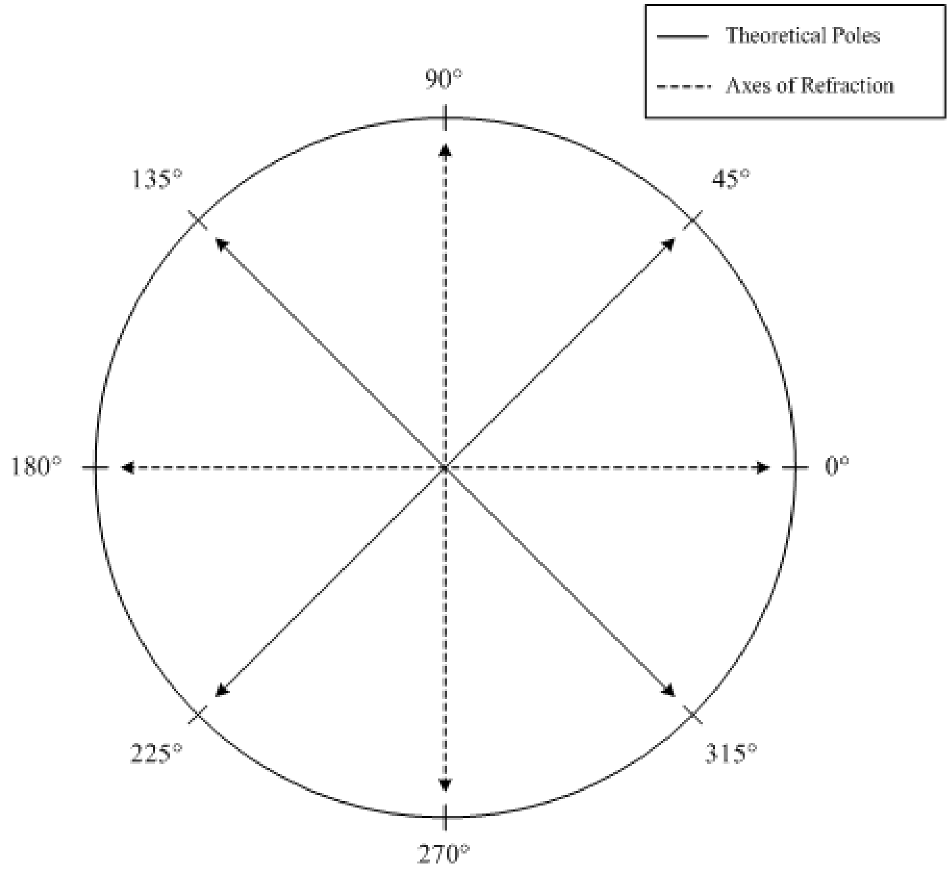

Figure (4-4) – Cubic crystal orientations of interest

Aligning the double-pass setup was a little more complicated. The throughput of the two collimators could not be optimized individually because they were placed at right angles to each other. To optimize the throughput of the system, the gold-surfaced mirror and polarizing beamsplitter cube was installed into the beam path. Because the polarization state of the linearly polarized light traveling back through the beamsplitter cube was in the same state as when it left the cube, no light was transmitted out of the other side of the cube to the second collimator. Before trying to optimize the location of the second collimator, the beam traveling through the cube, off the mirror and back through the cube, was aligned so that the returning light was re-coupled back into the first collimator. The second input leg of a fiber optic coupler was used to monitor and maximize the return through the input collimator. This process ensured that the optics were correctly aligned prior to inserting the waveplate and Pockels cell.

To align the second collimator to the beam path, and eighth waveplate was added into the beam path to modify the polarization state of the light and allow some of the light to be passed to the second collimator by the beamsplitting cube. The process of aligning the waveplate used for this setup was essentially the same as that used for the single-pass setup. The ordinary or extraordinary axis of the waveplate was found by maximizing the light returning through the input collimator. It was then rotated 45°, creating elliptically polarized light on its first pass and circularly polarized light on its second pass. The polarizing beamsplitter halved the light, sending 50% of it to the second collimator. The position of the second collimator was optimized to receive as much light as possible. Once all of the optics had been aligned, the Pockels cell was inserted between the mirror and waveplate. The refraction losses were minimized, and voltage was applied to the crystal to determine its poles. Once they were discovered, the experiment was performed.

A greater emphasis was placed on finding the V_π value of BGO than on BSO or ZnSe, primarily because BGO had already been reported to perform well in harsh environments. Therefore two different samples of BGO crystal were tested to determine a more accurate value of its V_π. Only one sample each of ZnSe and BSO was tested, mainly due to availability. A photo of these crystal samples is shown below in Figure (4-5).

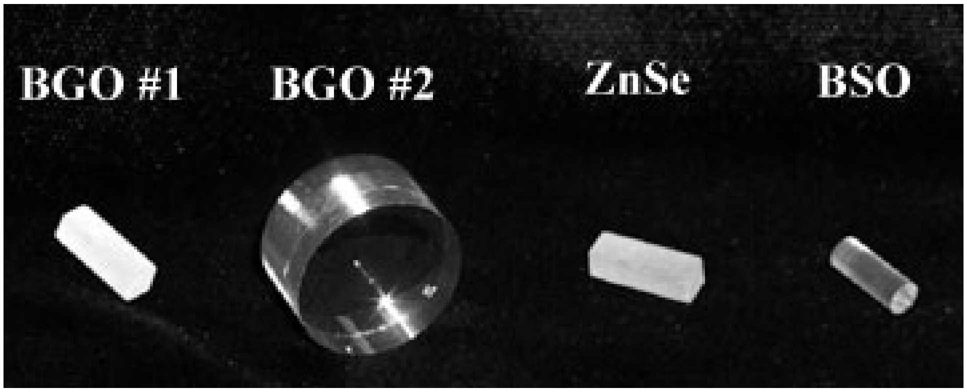

Figure (4-5) – Electro-optic crystal samples

The BGO and ZnSe samples were tested using the single-pass method while the BSO sample was tested using the double-pass method. This was done primarily because BSO has an intrinsic optical property called optical activity, which causes the polarization state of the light to rotate as it passes through the crystal. A second pass back through the crystal removes this rotation and allows us to keep the same orientation for the optics of the double-pass system.

Jones calculus has been used to mathematically analyze the polarization state of the light passing through both bench top experiments, with specific attention being given to the BSO double-pass experiment. These mathematical descriptions are presented in the Appendix at the end of this thesis.

The crystal samples were tested at 1319 nm then at 850 nm. Instead of switching back and forth from 1319 nm to 850 nm for each sample, all of the samples were tested at one wavelength first. Switching the crystal samples between experiments took less time and was prone to fewer alignment errors than swapping the laser source, receiver and all of the wavelength-sensitive optics.

Measuring V_π

Once the poles of the crystal sample were mapped out, extensive testing began at each pole. A block diagram of each test setup is shown in Figures (4-1) and (4-2). From these figures you can see that there is a 90:10 fiber-optic coupler on the input side of the test setup. This coupler served two purposes: it allowed a return measurement while setting up the double-pass test configuration, and it provided a means of monitoring the source power.

For every data point recorded for the V_π measurements, a corresponding reference source value was recorded to correct any irregularities in the data due to source variation and drift. This is very helpful in correcting the data because the output of the voltage sensor is intensity modulated and if the source power fluctuates, that error directly affects the output value measured.

In order to determine the value of V_π for a crystal sample, we recorded many data points while changing the voltage applied to the crystal. The electrodes of the Pockels cell and a digital voltmeter were connected to the high-voltage power supply. The applied voltage was stepped up from zero volts up to one thousand volts and back to zero at an interval of 100 volts. This process was repeated fifteen times for each of the four poles of the crystal.

Once the crystal sample had been measured, it was replaced with the next sample. Once all of the crystal samples had been studied, the wavelength of the light source and all of the polarization optics were changed and set up for the next series of tests. The poles of each crystal had to be again found and tested. As you might imagine, the process of taking such a large amount of raw data was very time consuming. The author recommends automating this process if it is ever repeated.

The V_π measurement process contained many sources of error. Measurement uncertainty and variations in applied voltage affect the measurement process but are assumed to be small sources of error. Optical misalignment and thermal instability were likely the most dominant sources of error in the V_π experiments.

The light sources used for the bench-top test sensor were very susceptible to power fluctuations caused by direct and ambient temperature variations. To counter this, a large thermal mass was attached to the laser diode housing. This greatly reduced the higher frequency thermal fluctuations of the source but did not eliminate them completely. According to the data, the average error in V_π attributed to thermal fluctuations was approximately 1.13%.

Likely the largest source of error in the experiments was misalignment of the optical components, specifically the misalignment of the EO crystal to the proper direction of polarization. The process by which we determine the half-wave voltage depends wholly upon the change in sensor output given an applied voltage. If the polarization optics are not perfectly aligned, we will measure a smaller change in sensor output and will calculate a larger half-wave voltage. From experimental trials in BGO, we saw that if the electro-optic crystal pole was misaligned from the correct polarization axis by 1° the average error in the measured value of V_π was 0.83%.

Thermal instability caused uncertainty in the measured sensor output, thus leading to an uncertainty in calculated half-wave voltage. Optical misalignment caused inaccuracy in the measurement of sensor response leading to an inaccurate calculation of the half-wave voltage. Both of these errors are additive and it is easy to see that attaining proper optical alignment and thermal stability are critical in determining an accurate half-wave voltage.

CHAPTER 5

DATA AND RESULTS

Data Processing

In finding the value of V_π for each crystal, hundreds of data points were recorded in an effort to determine V_π as accurately as possible. As mentioned in the previous chapter, each crystal has four poles at which data is recorded. For a cubic crystal, each pole should be 45° between the ordinary and extraordinary axes of the birefringent crystal. Figure (4-4) shows how the poles of a cubic electro-optic crystal are oriented to the ordinary and extraordinary axes of a cylindrical crystal sample.

Once the location of a pole was identified, the voltage applied to the Pockels cell was stepped up and then down fifteen times. From each data set, we were able to determine V_π at that pole location by using the slope of the intensity vs voltage curve traced out by the data. Once all four poles had been measured and all 60 data points were calculated, and average V_π value for the crystal was determined.

The single-pass method for approximating V_π will be presented first, followed by the double-pass V_π approximation method. Recall the biased amplitude modulator transmission equation from Chapter 2 as

$$T = \sin^2\left(\frac{\pi}{2}\frac{V}{V_\pi} + \frac{\pi}{4}\right) \tag{5-1}$$

We can rewrite this equation to

$$T = \frac{1}{2}\left[1 - \cos\left(2\left(\frac{\pi}{2}\frac{V}{V_\pi} + \frac{\pi}{4}\right)\right)\right] \tag{5-2}$$

by the power relation

$$\sin^2\theta = \frac{1}{2}(1 - \cos\theta) \tag{5-3}$$

We are now able to express Equation (5-2) as

$$T = \frac{1}{2}\left[1 - \cos\left(\pi\frac{V}{V_\pi}\right)\cos\left(\frac{\pi}{2}\right) + \sin\left(\pi\frac{V}{V_\pi}\right)\sin\left(\frac{\pi}{2}\right)\right] \tag{5-4}$$

by the angle-sum relation

$$\cos(\theta + \beta) = \cos\theta\cos\beta - \sin\theta\sin\beta \tag{5-5}$$

and can simplify this to

$$T = \frac{1}{2}\left(1 + \sin\left(\pi\frac{V}{V_\pi}\right)\right) \tag{5-6}$$

If we also recall our applied voltage limitation of

$$V << V_\pi \tag{5-7}$$

we can approximate Equation (5-6) to be

$$T \approx \frac{1}{2}\left(1 + \pi \frac{V}{V_\pi}\right) \tag{5-8}$$

by the small angle approximation

$$\sin\theta \approx \theta \tag{5-9}$$

provided

$$\theta << 2\pi \tag{5-10}$$

Equations (5-2), (5-6) and (5-8) are shown graphically below in Figure (5-1).

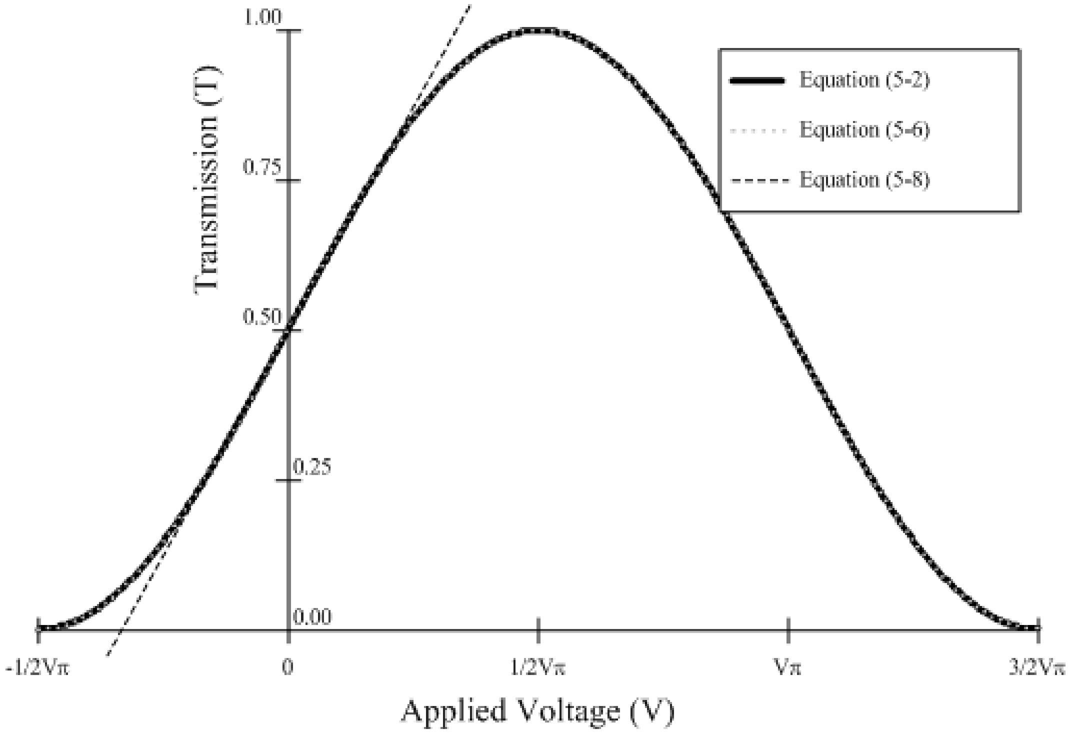

Figure (5-1) – Single-pass transmission curves and approximation

It can be seen that by following the guidelines of Equation (5-7) we can closely approximate the actual transmission curve of the single-pass biased amplitude modulator.

In order to solve for V_π we can expand Equation (5-8) by substituting for V and T.

$$T_1 = \frac{I_1}{I_i} \approx \frac{1}{2}\left(1 + \pi \frac{V_1}{V_\pi}\right)$$
$$T_2 = \frac{I_2}{I_i} \approx \frac{1}{2}\left(1 + \pi \frac{V_2}{V_\pi}\right) \tag{5-11}$$

If we solve one of the above equations for I_i we can substitute it into the other equation and obtain an expression for V_π.

$$I_i \approx \frac{I_1}{\frac{1}{2}\left(1 + \pi \frac{V}{V_\pi}\right)} \tag{5-12}$$

Equation (5-12) is substituted into the second half of Equation (5-11) to get

$$\frac{I_2}{I_1} \frac{1}{2}\left(1 + \pi \frac{V_1}{V_\pi}\right) \approx \frac{1}{2}\left(1 + \pi \frac{V_2}{V_\pi}\right) \tag{5-13}$$

and by multiplying through by V_π and reordering and simplifying the terms we get an equation that approximates V_π.

$$V_\pi \approx \frac{\pi\left(V_2 I_1 - V_1 I_2\right)}{I_2 - I_1} \tag{5-14}$$

This equation holds for estimating V_π over two data points. In order to more closely approximate V_π we would like to incorporate the slope,

$$m = \frac{I_2 - I_1}{V_2 - V_1} \tag{5-15}$$

of a set of data points. We can do this by dividing the top and bottom parts of Equation (5-14) by V_2 - V_1.

$$V_\pi \approx \frac{\pi \dfrac{V_2 I_1 - V_1 I_2}{V_2 - V_1}}{m} \tag{5-16}$$

This equation greatly simplifies if we start our slope data at $V_1 = 0$.

$$V_\pi \approx \frac{\pi I_1}{m} \tag{5-17}$$

This is the equation used to approximate V_π for the single-pass measurements using the slope and initial intensity measurement from each data set.

In order to find the equation that approximates V_π for the double-pass measurements we recall Equation (3-4) as

$$T = \sin^2\left(\frac{\pi V}{V_\pi} + \frac{\pi}{4}\right) \tag{5-18}$$

and by the power relationship of Equation (5-3) and angle sum relationship of Equation (5-5) we can rewrite Equation (5-18) to

$$T = \frac{1}{2}\left(1 + \sin\left(2\pi \frac{V}{V_\pi}\right)\right) \tag{5-19}$$

We can approximate this equation by the small angle approximation of Equation (5-9) to

$$T \approx \frac{1}{2}\left(1 + 2\pi \frac{V}{V_\pi}\right) \tag{5-20}$$

Figure (5-2) graphically shows Equations (5-18) and (5-19) and how Equation (5-20) approximates them.

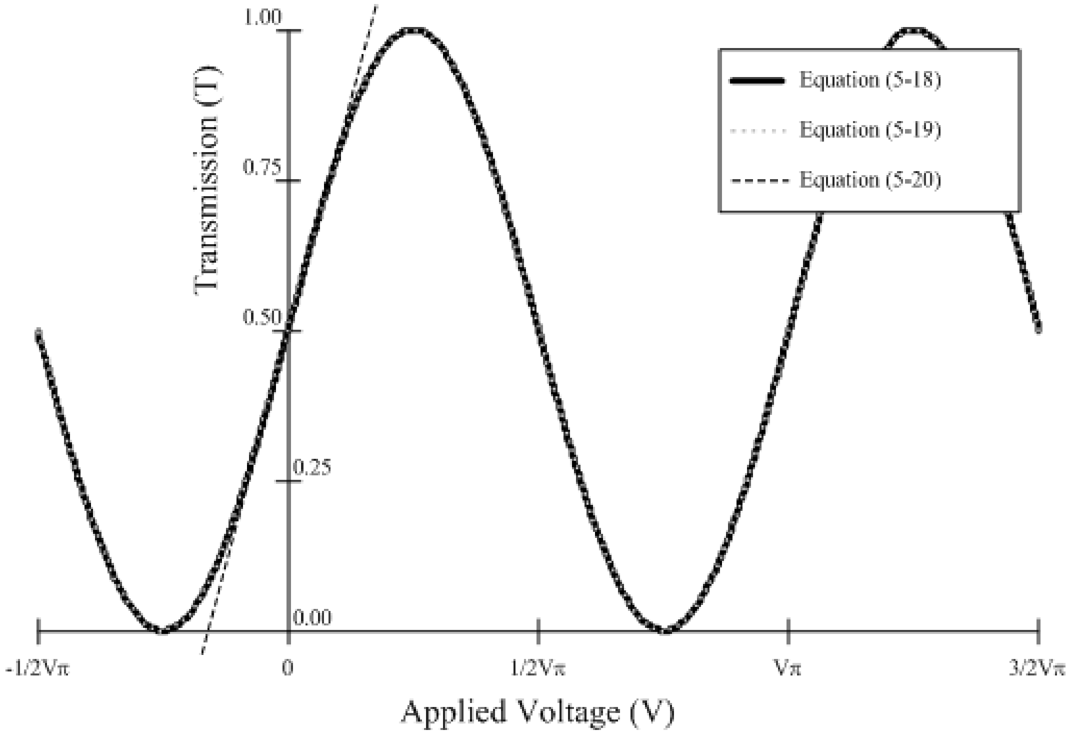

Figure (5-2) – Double-pass transmission curves and approximation

We are now able to derive an approximation for V_π for the double-pass experiment by the same techniques used for Equations (5-8) through (5-17).

$$V_\pi \approx \frac{2\pi I_1}{m} \tag{5-21}$$

Data Correction

Now that we have simple equations that can approximate V_π based on the sensor output at $V = 0$, we must determine the slope of the output vs. voltage curve for each data set. Before V_π can be calculated however, the individual data points need to be corrected for source drift to ensure an accurate calculation of the slope.

The 90:10 fiber-optic coupler shown in Figure (4-1) and Figure (4-2) was used to monitor a portion of the laser source power for intensity fluctuations. As the applied voltage was increased and data points were taken for sensor output, a measurement of the source stability was taken and used to correct for any source drift at that data point. Table (5-1) shows a sample data set with source drift correction.

Applied Voltage (V)	Measured Output (μW)	Measured Drift (μW)	Drift Correction Factor	Drift Output (μW)
0	12.57	10.95	1.0000	12.5700
100	12.62	10.95	1.0000	12.6200
200	12.67	10.94	1.0009	12.6816
300	12.72	10.94	1.0009	12.7316
400	12.77	10.94	1.0009	12.7817
500	12.82	10.94	1.0009	12.8317
600	12.87	10.94	1.0009	12.8818
700	12.92	10.93	1.0018	12.9436
800	12.96	10.93	1.0018	12.9837
900	13.02	10.93	1.0018	13.0438
1000	13.06	10.93	1.0018	13.0839
900	13.01	10.93	1.0018	13.0338
800	12.95	10.92	1.0027	12.9856
700	12.90	10.92	1.0027	12.9354
600	12.84	10.91	1.0037	12.8871
500	12.79	10.91	1.0037	12.8369
400	12.73	10.91	1.0037	12.7767
300	12.68	10.91	1.0037	12.7265
200	12.63	10.91	1.0037	12.6763
100	12.57	10.90	1.0046	12.6277
0	12.50	10.89	1.0055	12.5689

Table (5-1) – Sample data set corrected using source drift data

Since we are operating along the linear portion of the sensor transmission curve, we should expect to see the measured data form a straight line from 0 to 1000 volts and then trace itself back down to 0 volts. The uncorrected data in the above data set does not do this, but when we correct for source drift we achieve this goal. Figure (5-3) shows the uncorrected and corrected sensor output vs. applied voltage curves of the sample data in Table (5-1).

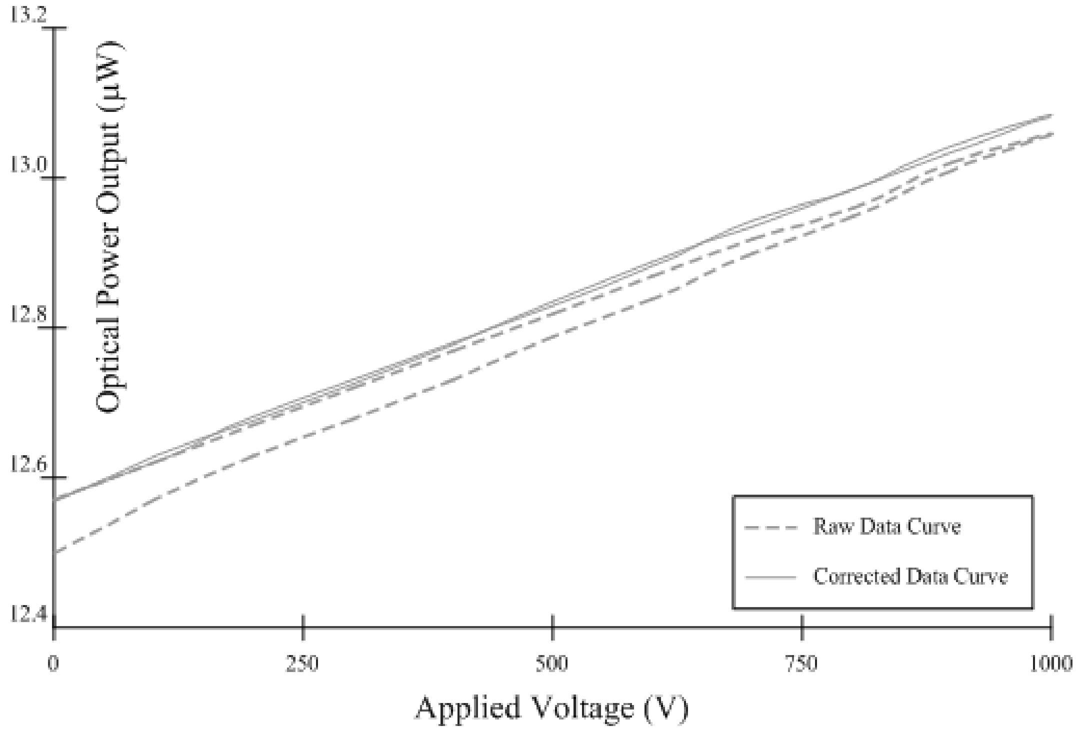

Figure (5-3) – Sample data set with drift correction

Using the corrected data, we can calculate a slope value and determine V_π using either Equation (5-17) or (5-22), depending on the experimental setup. We do this for each of the fifteen data sets and average them to determine the half-wave voltage of the crystal at that pole. Once we have processed all four poles, we can look at the distribution of half-wave voltages to determine if the measurements were taken at the correct pole locations. Ideally, each data set from all four poles should yield the same half-wave voltage. To determine the final half-wave voltage for the crystal, all 60 calculated values of V_π are averaged.

In order to better visually interpret the data for each crystal we can normalize each data set to the same scale as the transmission curves shown in Figure (5-1) and

Figure (5-2) and plot the ideal system response with the actual data set. To do this, we make the assumption that at zero applied volts, we are receiving half of the light that was sent into the sensor. We then divide each corrected sensor output data point by twice the value of the initial sensor output and are left with a normalized transmission value through the system. Figure (5-4) shows the normalized uncorrected and corrected transmission curves of the data set in Table (5-1) with the measured transmission curve for that pole, calculated using the average half-wave voltage determined for that particular pole of the crystal.

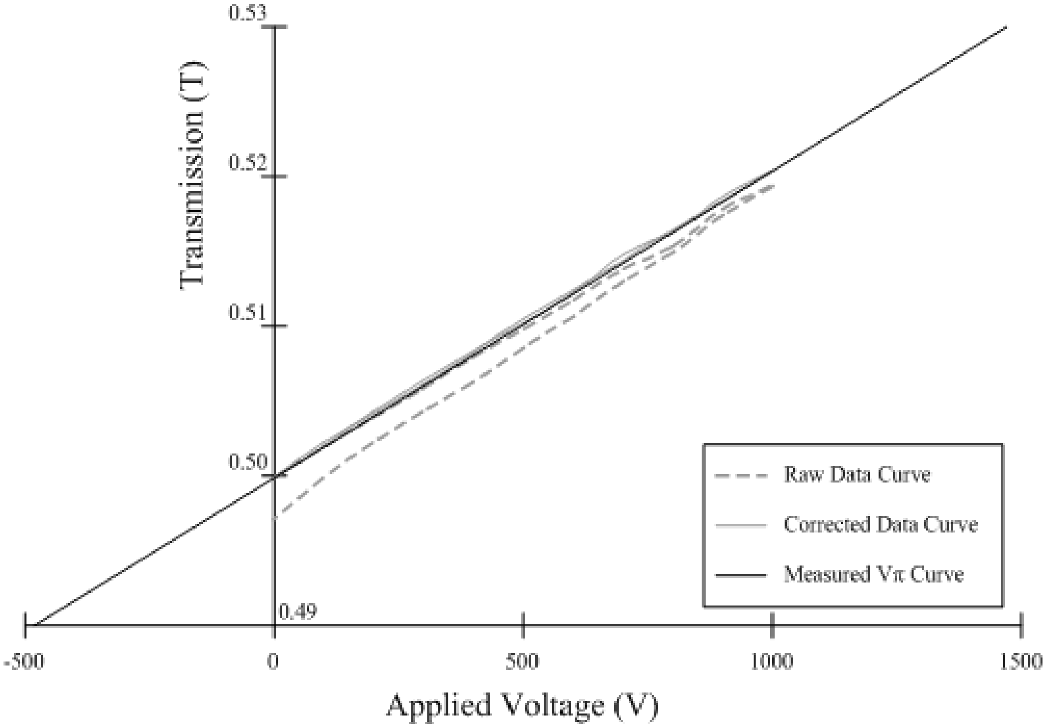

Figure (5-4) – Normalized raw vs. corrected data curves

BGO Results

Now that we have shown how the half-wave voltage of a crystal is determined we can use these methods to find values for each of our crystal samples. We are able to use data previously reported in the literature to predict the values of V_π we are likely to obtain for BGO. Table (5-2) lists values of V_π for BGO that have either been directly stated or have been calculated using Equation (2-37) and the data reported in the literature.

Source	Wavelength (nm)	Index of Refraction	Pockels Coefficient (pm/V)	V_π (V)
Bortfeld(53)	405	2.218*	0.82	22632
Bortfeld(53)	440	2.181*	0.85	24948
Bortfeld(53)	495	2.142*	0.89	28296
Bortfeld(53)	542	2.122*	0.92	30828
Bortfeld(53)	631	2.098*	0.95	35963
Kamada(21)	855	2.065	1.09	44540
Kamada(21)	633	2.098	1.01	33934
Montemezzani(34)	632.8	2.097	0.96	35741
Montemezzani(34)	514.5	2.135	0.89	29701
Montemezzani(34)	488.9	2.148	0.86	28681
Montemezzani(34)	457.9	2.167	0.83	27107
Montemezzani(34)	363.9	2.268	0.62	25155
Montemezzani(34)	351.1	2.291	0.57	25612
Montemezzani(34)	334.5	2.326	0.49	27123
Montemezzani(34)	305.4	2.41	0.33	33058
Nitsche(35)	450	2.07	1.03	24628
Nitsche(35)	535	2.07	1.03	29280
Nitsche(35)	620	2.07	1.03	33932
Santos(31)	632.8	-	1.03	34200
Williams(20)	1000	2.0578	1.11	51694
Williams(20)	950	2.0601	1.11	48945
Williams(20)	900	2.0635	1.11	46140
Williams(20)	850	2.0678	1.11	43305
Williams(20)	800	2.0723	1.1	40861
Williams(20)	750	2.0786	1.08	38663
Williams(20)	633	2.0972	1.07	32068
Williams(20)	600	2.1058	1.06	30308
Williams(20)	550	2.1204	1.05	27472
Yakymyshyn(8)	850	2.07	1.03	46520

* Estimated based on reported values(53)

Table (5-2) – Reported values of V_π for BGO

If we assume there is a linear relationship between V_π and wavelengths longer than about 400 nm, and the change in the Pockels coefficient and index of refraction are minimal, we are able to predict values of V_π for BGO at 850 nm and 1319 nm.

Figure (5-5) shows a plot of the V_π values from Table (5-2) with a linear fit to the data reported by Williams(20). We can use the equation of this trendline to extrapolate a predicted value of V_π and should expect it to be approximately 43,592 volts at 850 nm and 68,581 volts at 1319 nm.

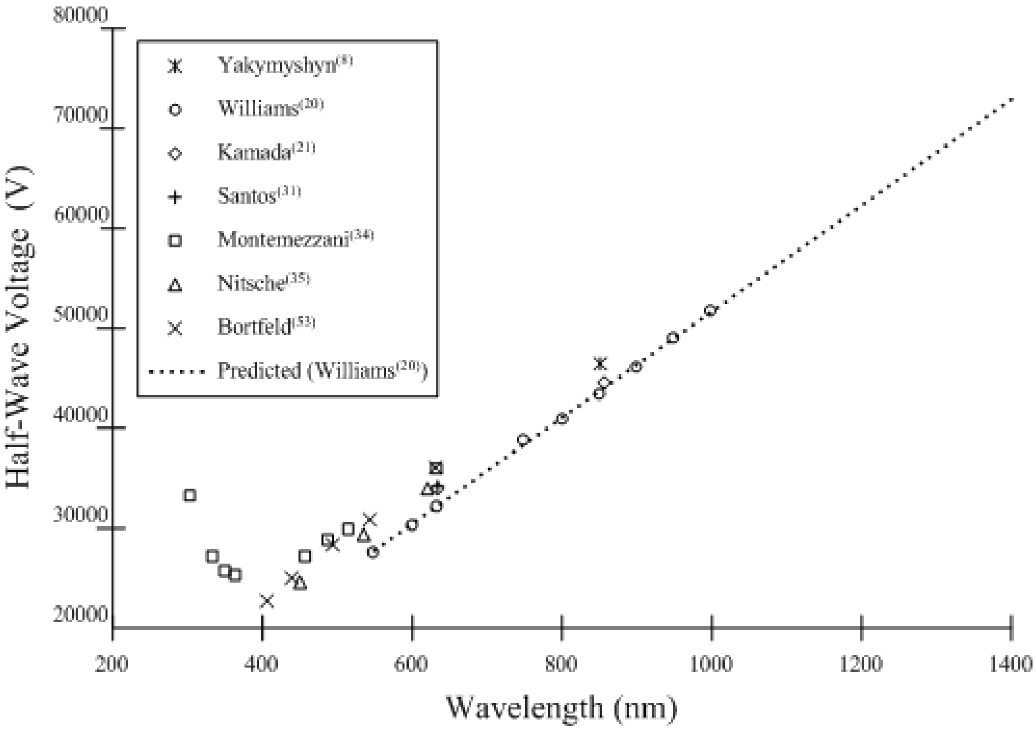

Figure (5-5) – BGO V_π literature data

Two different BGO crystals were tested using the single-pass bench top experiment at 1319 nm. The first BGO sample was a 3.5 mm x 3.5 mm x 10 mm rectangular piece cut from a large-diameter crystal rod that originally came from a crystal company in China. This crystal rod had been previously divided into smaller pieces to make early prototype BGO sensors. The second BGO sample was an 18 mm diameter 12 mm long crystal rod that came from a commercial crystal company in Germany. They were both tested at 1319 nm to obtain a comparison between the first crystal, which had already been tested for performance, and the second.

Before the crystals could be tested, their ordinary and extraordinary indexes of refraction were determined by locating the orientations that yielded zero change in sensor output for an applied voltage of 1000 volts. The locations of the poles of each crystal were found by finding the orientations that yielded maximum change in sensor output for an applied voltage of 1000 volts. Using the Jones calculus model of the single-pass experiment presented in the Appendix, we are able to plot the absolute value of the change in sensor output to an applied voltage of 1000 volts as a function of EO crystal rotation. We shall refer to this plot as the calculated response lobes of the crystal. The location of the axes and poles for both BGO samples were as expected of a cubic crystal and Figure (5-6) shows the location of all orientations of interest for the sample crystals.

The first BGO crystal sample was tested at 1319 nm and 60 data sets were obtained. These data sets were used to calculate an average half-wave voltage and a standard deviation for the crystal. The measurement error was found by dividing the standard deviation by the average half-wave voltage. Table (5-3) lists this information for BGO #1 at 1319 nm.

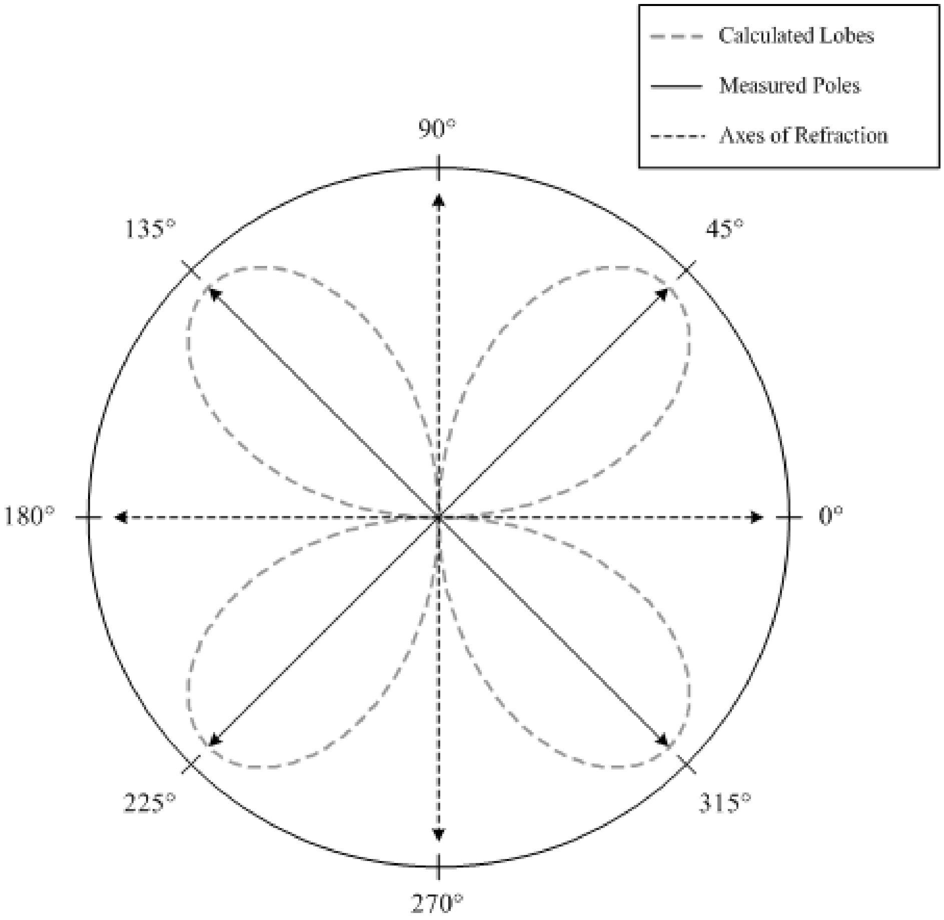

Figure (5-6) – BGO orientations of interested

BGO #1 – 1319 nm	Raw Measured	Drift Corrected*
Median Vπ (V)	75681	-
Standard Deviation (V)	2350	-
Error (%)	3.1%	-

* reference coupler unavailable; drift corrected values not calculated

Table (5-3) – BGO sample #1 V_π results at 1319 nm

We are now able to generate transmission curves based on the measured and predicted half-wave voltages of the crystal using Equation (2-40) to better compare the two values. We are also able to normalize the average data curves at each pole location and plot them on the same graph with the measured and predicted transmission curves to better observe the over-all measurement deviation. Figure (5-7) shows the measured and predicted transmission curves of BGO #1 at 1319 nm and Figure (5-8) shows them with the normalized pole data curves.

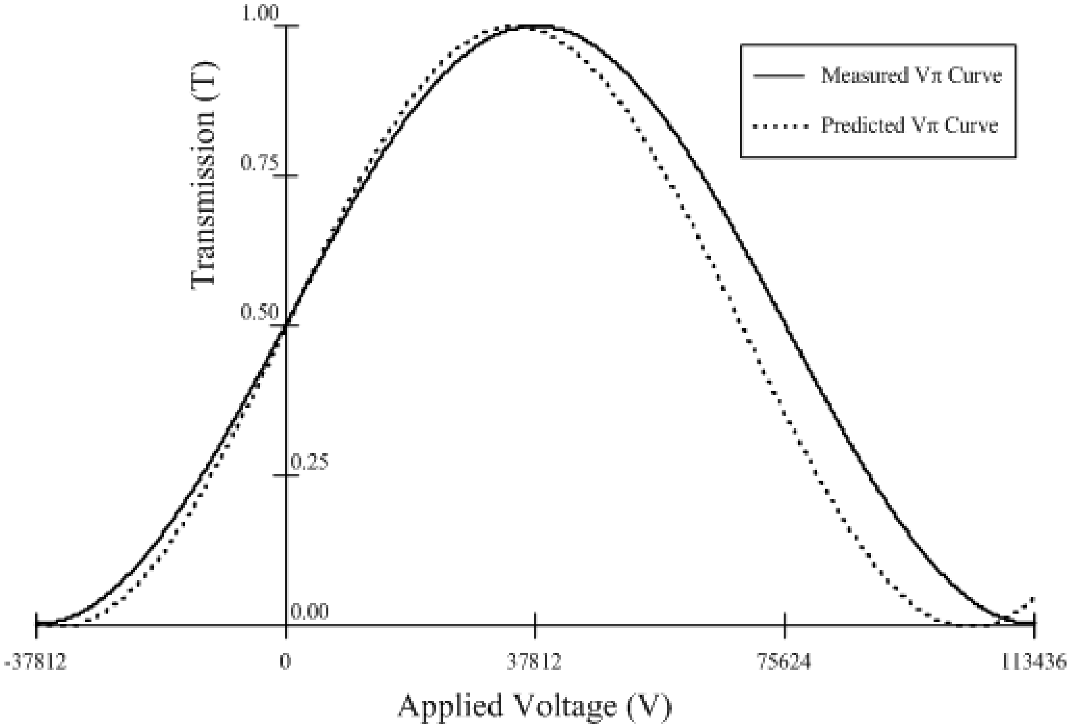

Figure (5-7) – Transmission curves for BGO #1 at 1319 nm

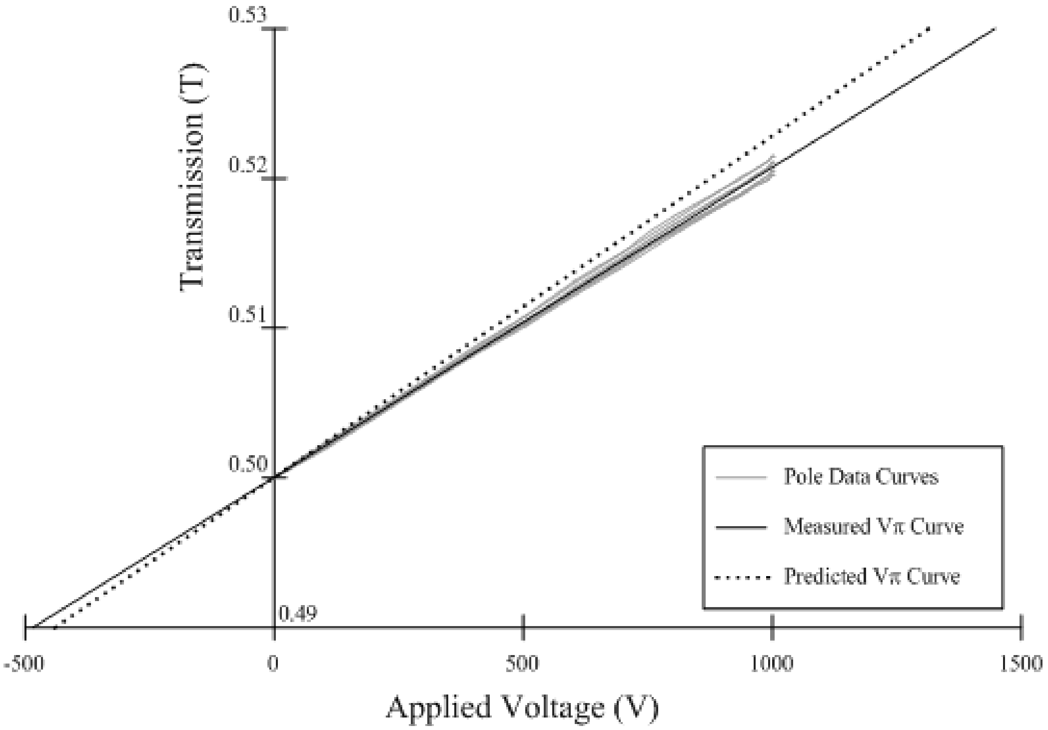

Figure (5-8) – Pole data and transmission curves for BGO #1 at 1319 nm

The first BGO sample was tested at 1319 nm and had an uncorrected half-wave voltage of 75,681 volts with a 3.1% measurement uncertainty. A reference coupler was not available during the testing of this sample, thus drift correction was not possible. When compared to the predicted value obtained using the data by Williams(20), we see that our half-wave voltage value is approximately 10.4% larger than predicted.

BGO sample #2 was also tested at 1319 nm. For this crystal, source drift correction was used to more accurately determine half-wave voltage. Sixty data sets were taken in this single-pass bench-top experiment and the processed results are given in Table (5-4).

BGO #2 – 1319 nm	Raw Measured	Drift Corrected
Median Vπ (V)	75596	75544
Standard Deviation (V)	1333	1961
Error (%)	1.8%	2.6%

Table (5-4) – BGO sample #2 V_π results at 1319 nm

We again are able to use Equation (2-40) to generate transmission curves for this crystal sample based upon the measured and predicted half-wave voltages. These curves are shown in Figure (5-9). The fifteen data curves for each pole were normalized and averaged and are presented in Figure (5-10) with the transmission curves of Figure (5-9).

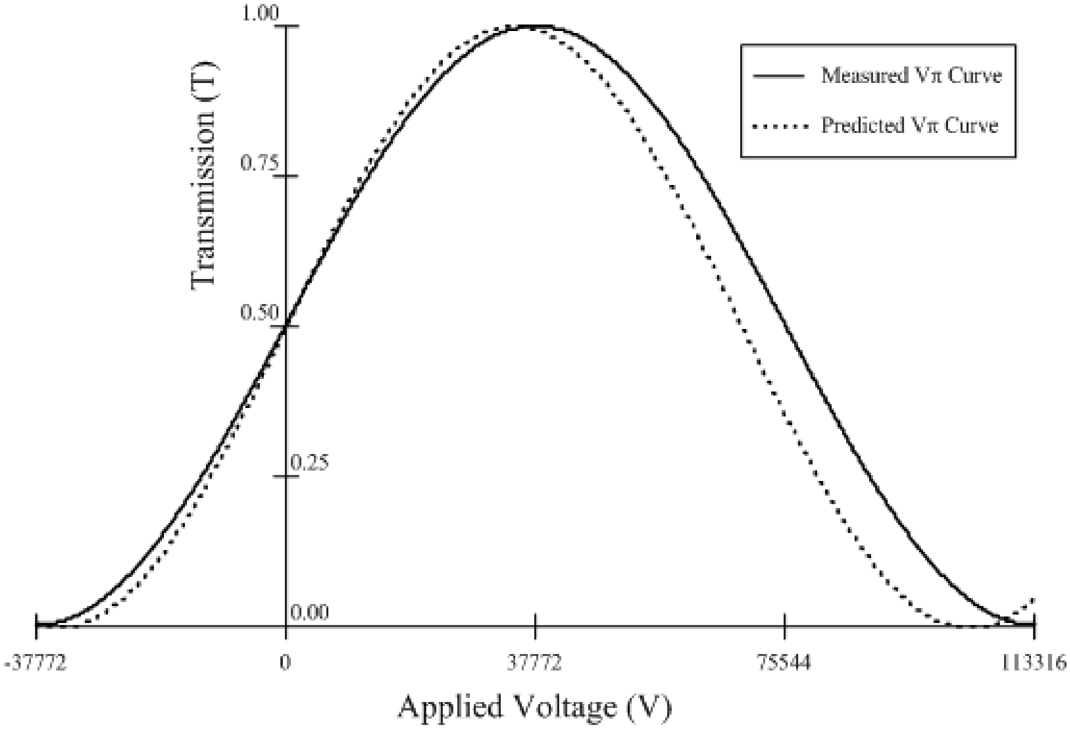

Figure (5-9) – Transmission curves for BGO #2 at 1319 nm

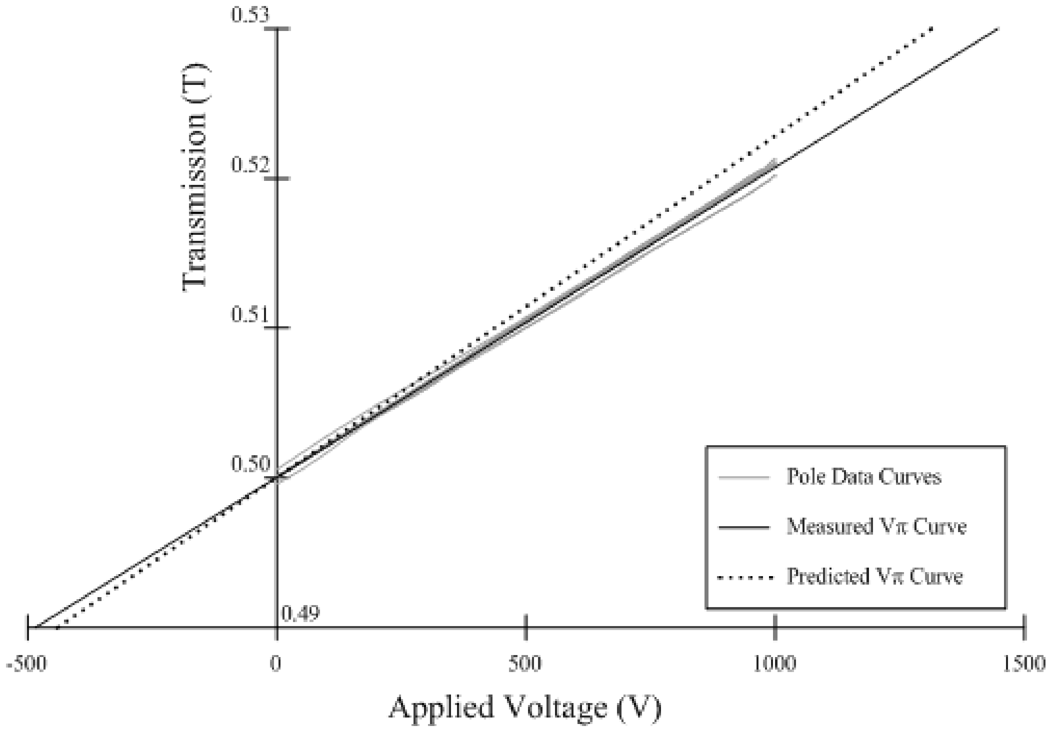

Figure (5-10) – Pole data and transmission curves for BGO #2 at 1319 nm

This BGO sample at 1319 nm had a raw half-wave voltage of 75,596 volts measured with a 1.8% uncertainty and a drift-corrected half-wave voltage of 75,544 volts with a measurement uncertainty of 2.6%. The difference between our measured half-wave voltage and the predicted value of 68,581 volts is 10.2%. The results of the second BGO crystal compare almost exactly with that of the first. For this reason, the first BGO crystal was not tested further.

The second BGO crystal was also tested using the single-pass bench top setup at 850 nm. The orientations of interest were again located and coincided with those found from the 1319 nm experiments. Thus Figure (5-6) is accurate for BGO at both

1319 nm and 850 nm. The same V_π experiments were performed as for the 1319 nm test and the results obtained are given in Table (5-5).

BGO #2 – 850 nm	Raw Measured	Drift Corrected
Median Vπ (V)	46852	46837
Standard Deviation (V)	3482	3437
Error (%)	7.4%	7.3%

Table (5-5) – BGO sample #2 V_π results at 850 nm

Using the measured and predicted values of the half-wave voltage, we generated transmission curves for BGO at 850 nm. We also normalized, averaged and plotted the pole data curves with the measured and predicted transmission curves. These graphs are shown in Figure (5-11) and Figure (5-12) respectively.

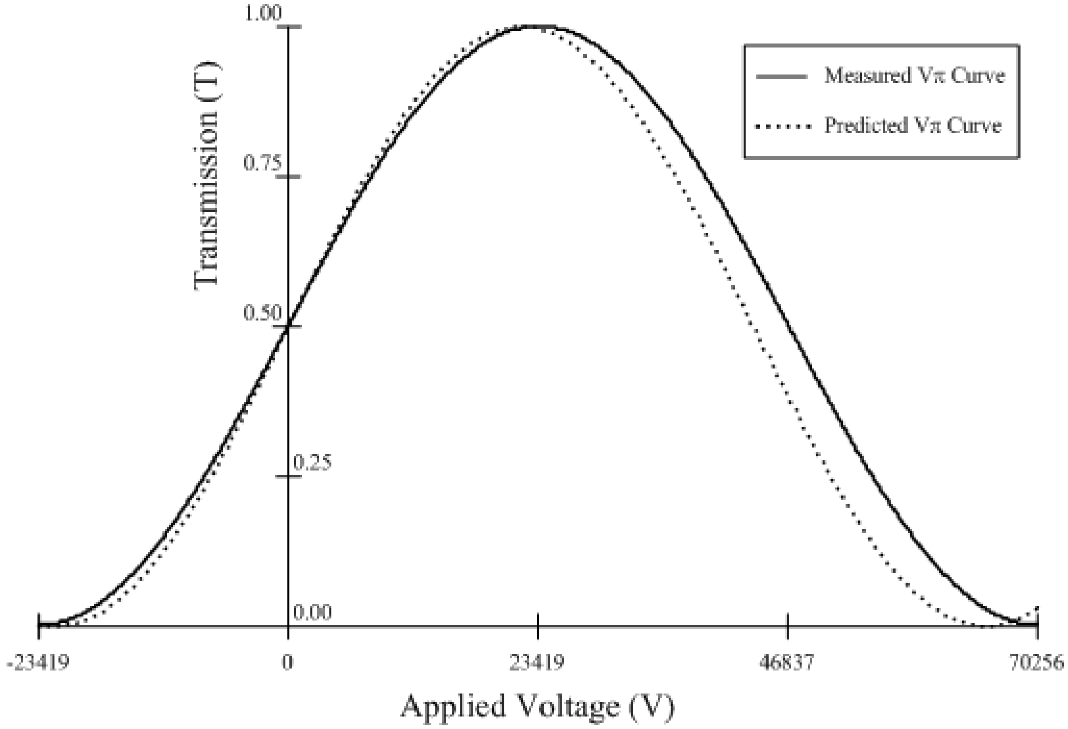

Figure (5-11) – Transmission curves for BGO #2 at 850 nm

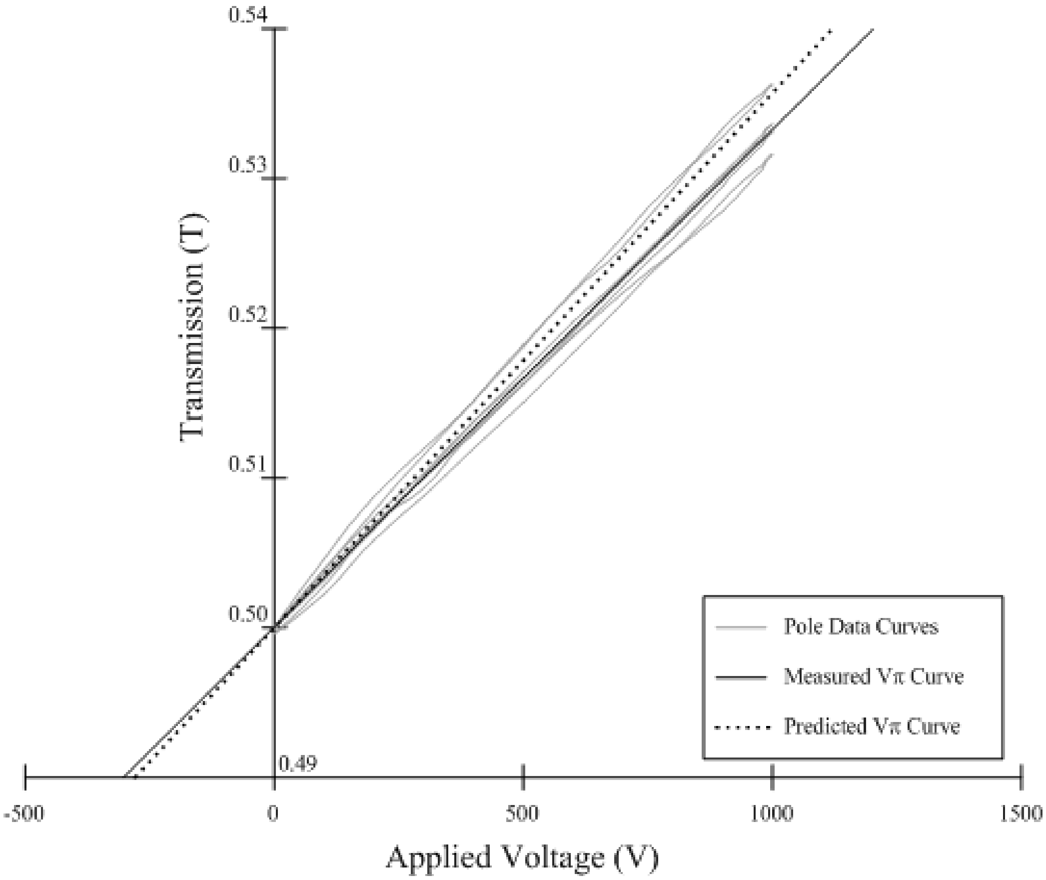

Figure (5-12) – Pole data and transmission curves for BGO #2 at 850 nm

The second BGO sample was tested at 850 nm and was found to have a drift-corrected V_π value of 46,837 volts with an uncertainty of 7.3%. If we compare the average half-wave voltage measured for BGO at 850 nm with the predicted value of 43,592 volts, we see that our measured half-wave voltage is 7.4% higher than we had predicted.

ZnSe Results

We are able to use data previously reported in the literature to try to estimate the values of V_π we are likely to obtain for ZnSe. Table (5-6) lists values of V_π for ZnSe that have either been directly stated or calculated using reported data.

Source	Wavelength (nm)	Index of Refraction	Pockels Coefficient (pm/V)	V_π (V)
Babucke(36,37)	514.5	2.83	1.20	9458
Baillou(39)	546.5	2.66	1.96	7407
Haase(38)	633	2.5688	2.00	9336
Milek(32)	546	2.66	2.00	7253
Yakymyshyn(8)	633	2.6	2.00	9004
Yakymyshyn(13)	850	-	-	12000
Yariv(1)	548	2.66	2.00	7279
Yariv(1)	633	2.6	2.00	9004
Yariv(1)	10600	2.39	2.20	176465

Table (5-6) – Reported values of V_π for ZnSe

We are able to roughly extrapolate for values of V_π for ZnSe at 850 nm and 1319 nm utilizing a trendline fitted to the data reported in Table (5-6). We again make the assumption of a linear relationship between the half-wave voltage and wavelengths longer than about 400 nm. Figure (5-11) shows a plot of the V_π values from Table (5-6) with a linear trendline fit to the data. Using the equation of this linear trendline, we should expect to see a value of V_π for ZnSe at 850 nm of approximately 12,824 volts and 20,693 volts at 1319 nm.

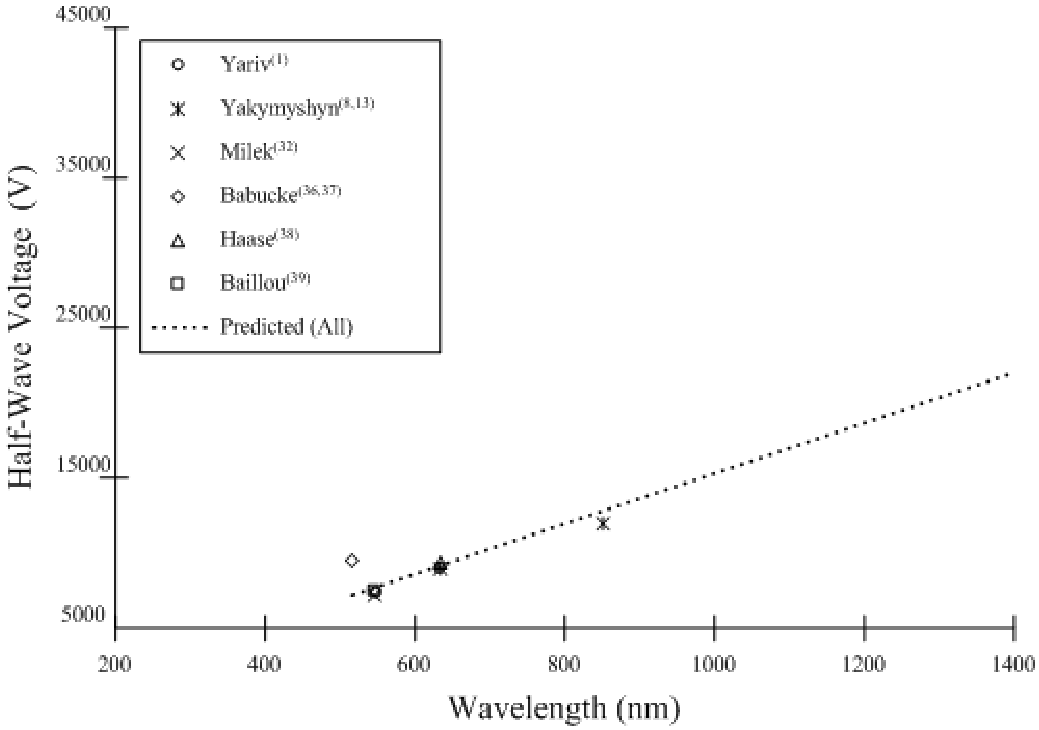

Figure (5-13) – ZnSe V_π literature data

The ZnSe sample was a rectangular cut piece measuring 3.5 mm x 3.5 mm x 10 mm and came from a commercial crystal company in the United States. It was tested using the single-pass method at both 1319 nm and 850 nm. The orientations of interest were located prior to the experiments and ideally they should coincide with those shown in Figure (4-4). The deviation observed here is only slight, on the order of a few degrees. Since the locations shown in Figure (5-12) are where the greatest response was measured, the sensor response data was taken there. Table (5-7) presents the measurement results obtained for ZnSe at 1319 nm.

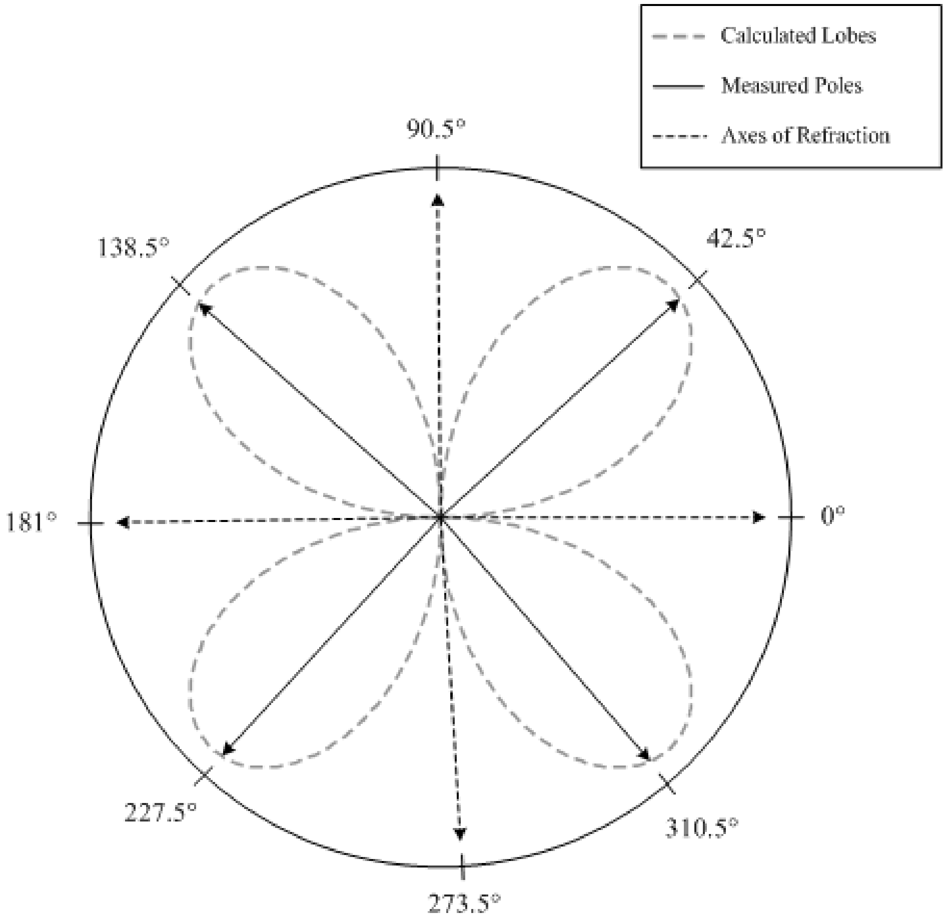

Figure (5-14) – ZnSe orientations of interest

ZnSe – 1319 nm	Raw Measured	Drift Corrected
Median Vπ (V)	43572	43469
Standard Deviation (V)	5135	5105
Error (%)	11.8%	11.7%

Table (5-7) – ZnSe V_π results at 1319 nm

As we did in the BGO analysis, we are able to generate and plot the transmission curves utilizing the measured and predicted V_π values as well as show the normalized pole data with these transmission curves. These graphs are shown in Figure (5-15) and Figure (5-16) respectively.

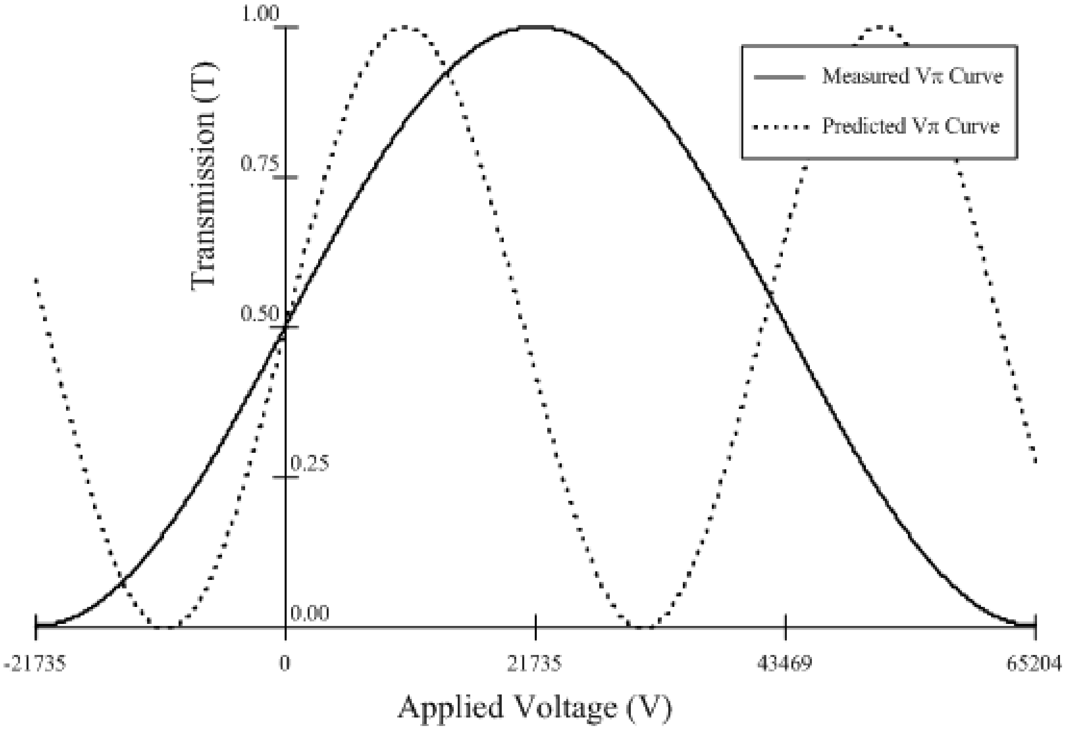

Figure (5-15) – Transmission curves for ZnSe at 1319 nm

As you can see from the above figure, our measured transmission curve is quite different from that which was predicted. This is attributed to an gross measurement or setup error.

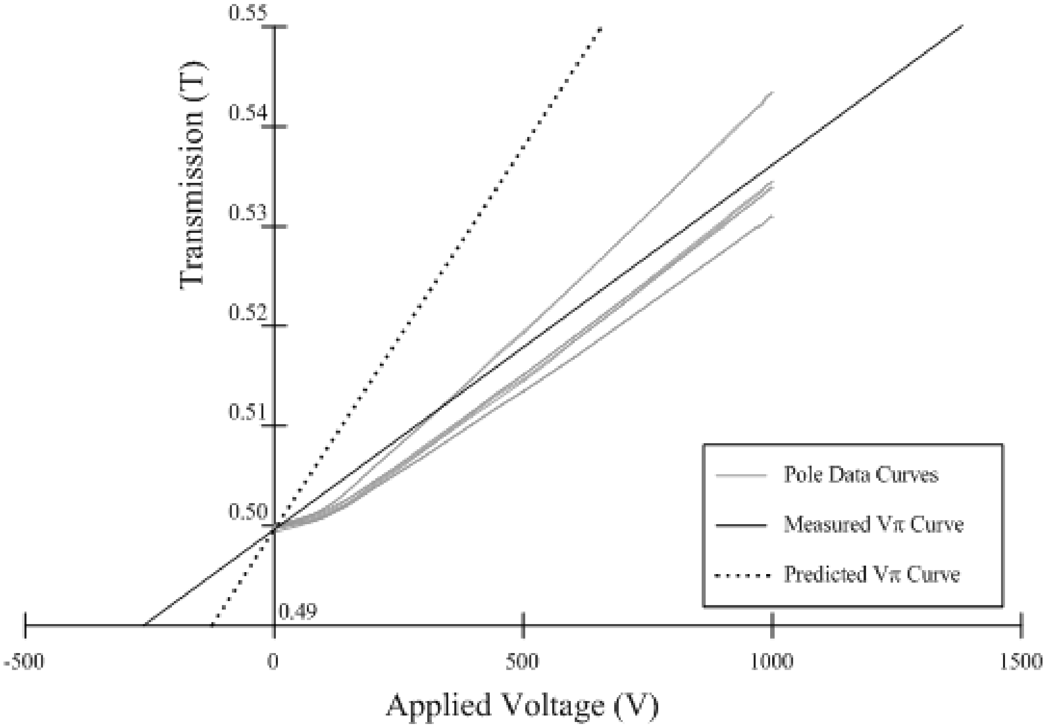

Figure (5-16) – Pole data and transmission curves for ZnSe at 1319 nm

The distribution seen between pole data curves is very pronounced in the data shown in Figure (5-16). This distribution is also noticed in the overall standard deviation reported in Table (5-7). The end result is a high uncertainty error in the measured half-wave voltage of ZnSe. Although the locations of maximum response within the crystal were carefully determined, the data collected at those locations does not yield plausible results.

The most striking feature of Figure (5-16) is the fact that the data curves don't appear to become linear in response until the applied voltage reaches approximately 300 volts. Due to the DC measurement process, it is suspected that the build-up of space charge within the ZnSe crystal is likely to blame for this nonlinearity. Space charge build-up will effectively reduce the strength of the electric field within the crystal, leading to lower sensor response and a larger half-wave voltage measurement.(45)

Using all of the data recorded for the ZnSe sample at 1319 nm, we find that our sample had a drift-corrected V_π of 43,469 volts with an uncertainty of 11.7%. When compared to what was extrapolated we see that we are about 110% larger than predicted. If we use only the data taken from 300 to 1000 volts at the location of greatest response we can make the argument that we measured a half-wave voltage of 34,055 volts and are only 65% larger than predicted.

This ZnSe crystal sample was also tested at 850 nm. The results of this experiment are presented in Table (5-8). The transmission curves generated by using the measured and predicted half-wave voltage for ZnSe at 850 nm are shown in Figure (5-17). The locations of greatest response were found to be identical to those shown in Figure (5-14) and the data taken at these poles were normalized and averaged and are plotted with the measured and predicted transmission curves in Figure (5-18).

ZnSe – 850 nm	Raw Measured	Drift Corrected
Median Vπ (V)	33108	33028
Standard Deviation (V)	2350	2624
Error (%)	7.1%	8.0%

Table (5-8) – ZnSe V_π results at 850 nm

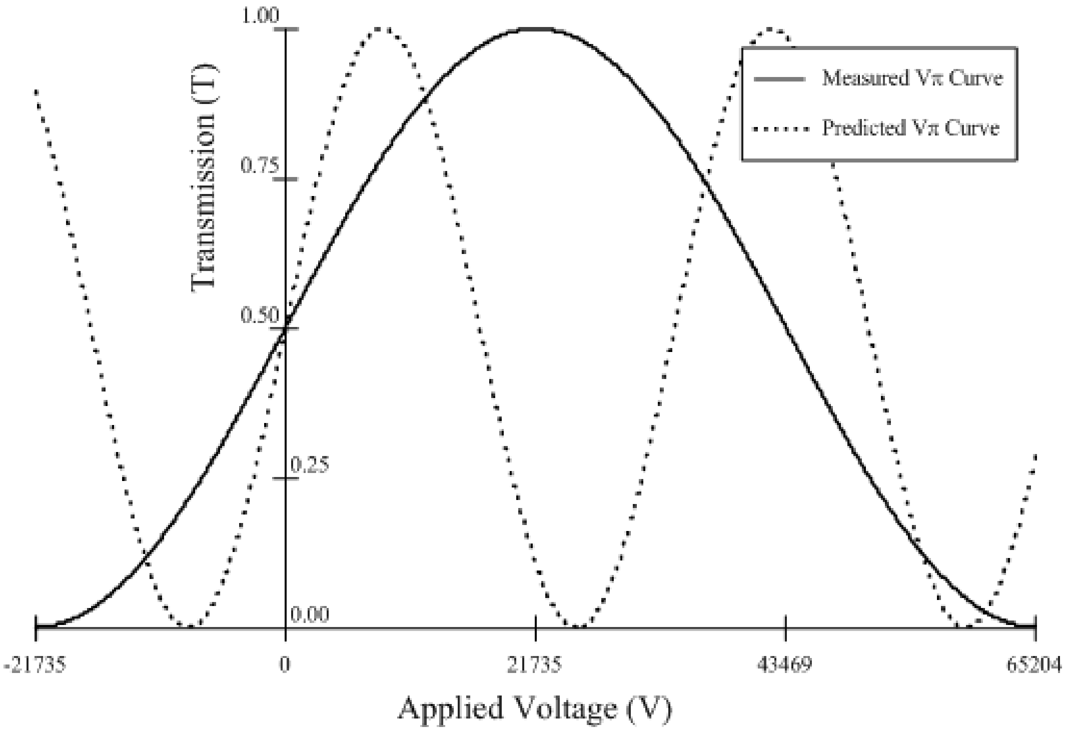

Figure (5-17) – Transmission curves for ZnSe at 850 nm

We again see a striking difference between the measured transmission curve and the predicted curve. In seeing the same large error in both the 1319 nm experiment and in the 850 nm experiment, we are more inclined to believe that our measurement process was in error.

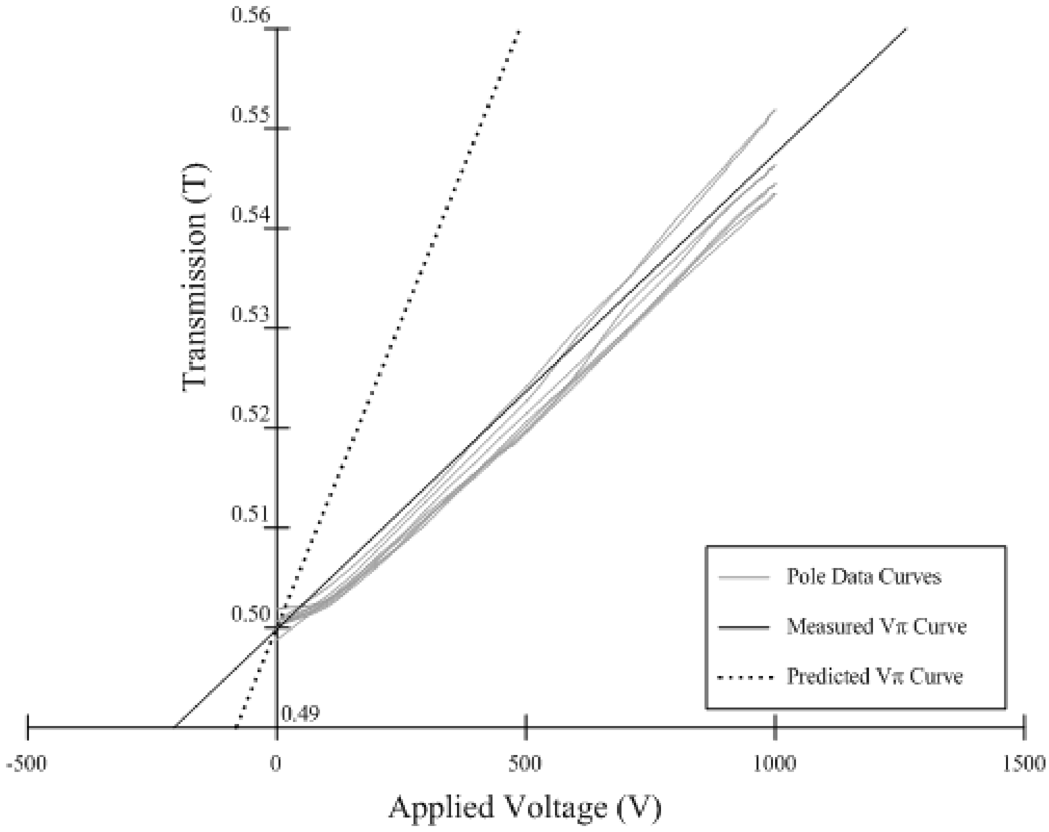

Figure 5-18 – Pole data and transmission curves for ZnSe at 850 nm

We notice that the data curves in Figure (5-18) are still not fully linear at voltages less than 300 volts. This leads us to again believe that the build-up of space charge is the likely explanation.(45)

When we use all of the data for the ZnSe sample at 850 nm we find it to have a drift-corrected V_π of 33,028 volts with a measurement uncertainty of 8.0%. If we compare this with the value predicted we are close to 158% larger than expected, but if we use only the data from 300 volts and up, we calculate a half-wave voltage of 28,797 volts that is 125% larger than the predicted value.

BSO Results

Table (5-9) lists values of V_π for BSO that have either been directly reported or have been calculated using Equation (2-37) and the data reported in the literature. We are able to roughly extrapolate the half-wave voltage of BSO at 850 nm and 1319 nm utilizing a trendline fitted to the data reported in Table (5-9). We again make the same assumption of a linear relationship between the half-wave voltage and wavelengths longer than about 400 nm. Figure (5-19) shows a plot of the V_π values from Table (5-9) with a linear trendline fit to the data. Using the equation of this linear trendline, we should expect to measure a half-wave voltage for BSO at 850 nm of approximately 6,211 volts and 10,019 volts at 1319 nm. However, it should be noted that due to the large scatter observed in the reported half-wave voltages, we are only able to linearly fit the data with an accuracy of about 40%. This leads to only a 40% confidence level in our predictions.

Source	Wavelength (nm)	Index of Refraction	Pockels Coefficient (pm/V)	V_π (V)
Aldrich(44)	632.9	2.532	5	3900
Edvold(33)	514.5	2.615	4.52	3183
Grunnet-Jepsen(45)	632.8	2.53	3.7	5280
Grunnet-Jepsen(45)	514.5	2.62	4.3	3326
Grunnet-Jepsen(45)	632.8	2.53	4.35	4491
Henry(46)	650	2.532	4.1	4883
Mallick(41)	578	2.56	3.5	4922
Murillo(42)	532	2.53	4.41	3725
Shepelevich(43)	632.8	2.54	5	3862
Yariv(1)	633	2.54	5	3863

Table (5-9) – Reported values of V_π for BSO

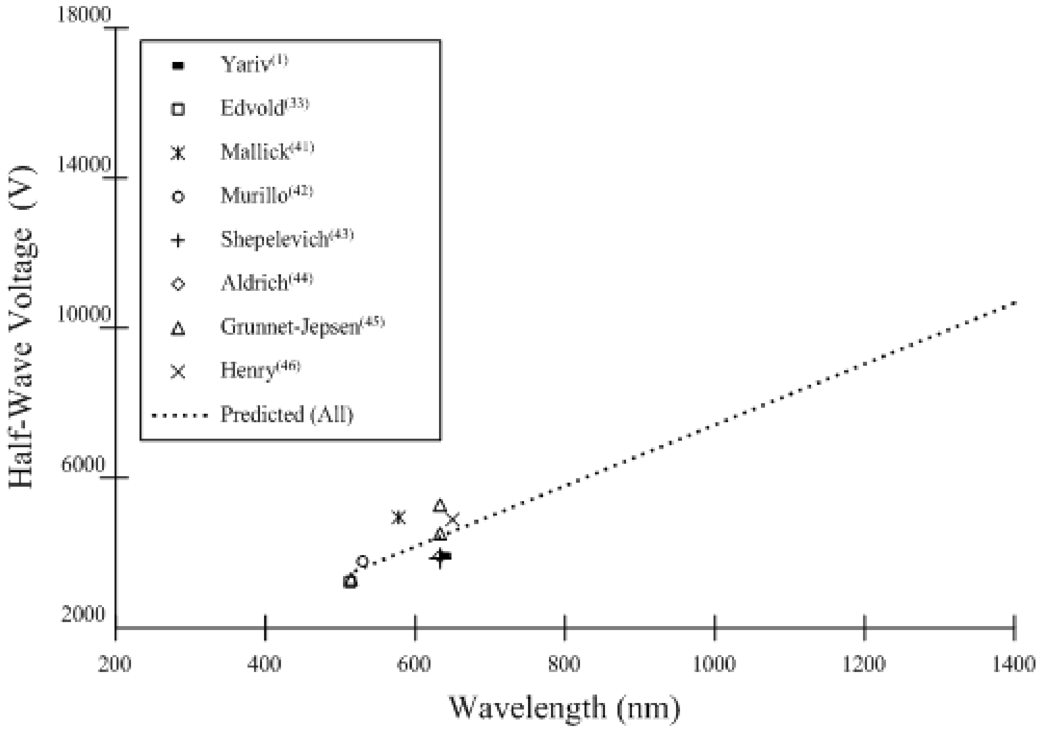

Figure (5-19) – BSO V_π literature data

The BSO sample was obtained from the same commercial crystal company that supplied the second BGO crystal sample. It measured 3.5 mm in diameter, was 10 mm long and was tested using the double-pass method at 1319 nm and 850 nm.

The optical activity of this crystal has caused the locations of the orientations of interest to move from where they would be expected for a non-optically active crystal. We were able to generate calculated response lobes using the Jones calculus analysis of a double-pass sensor system in the Appendix. Figure (5-20) shows these response lobes and the relative locations of the orientations of interest for the BSO crystal at 1319 nm.

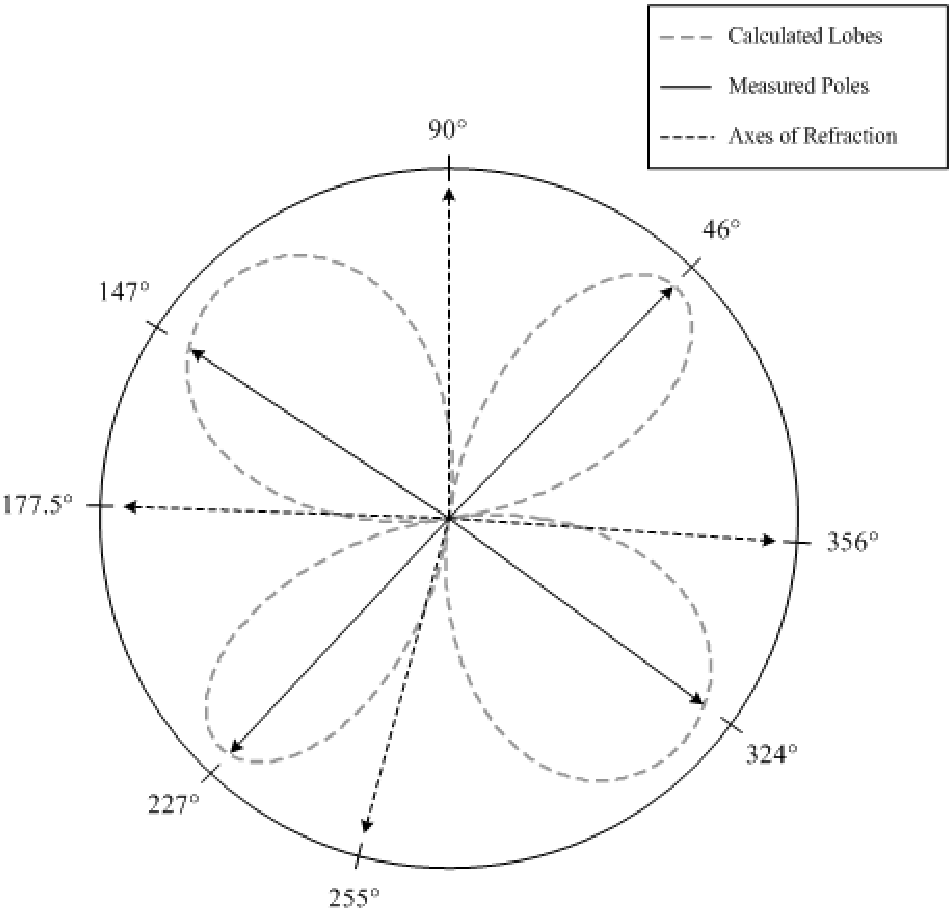

Figure (5-20) – BSO orientations of interest at 1319 nm

Once the poles of the crystal were determined, sensor response data was taken at each location. Not surprisingly, the V_π data exhibited some amount of scatter. The data taken at one positive pole matches well with the other positive pole, as do the negative poles. However, the values measured at the positive poles do not match up very well with those of the negative poles. This can been seen in Figure (5-22), which shows the pole data curves along with the transmission curves generated using the measured and predicted half-wave voltages presented in Figure (5-21). The overall standard deviation was not outrageous however, which led to a reasonable measurement uncertainty error. This can be seen in Table (5-10) along with the measured half-wave voltage of BSO at 1319 nm.

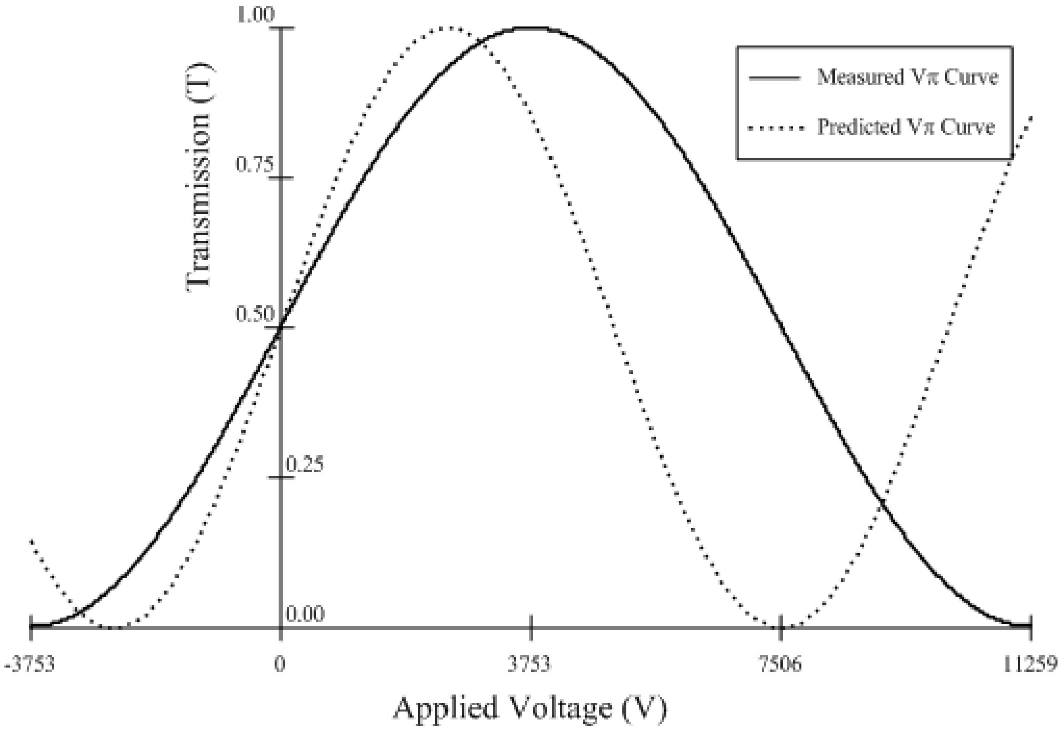

Figure (5-21) – Transmission curves for BSO at 1319 nm

BSO – 1319 nm	Raw Measured	Drift Correction
Median Vπ (V)	15030	15013
Standard Deviation (V)	786	794
Error (%)	5.2%	5.3%

Table (5-10) – BSO V_π results at 1319 nm

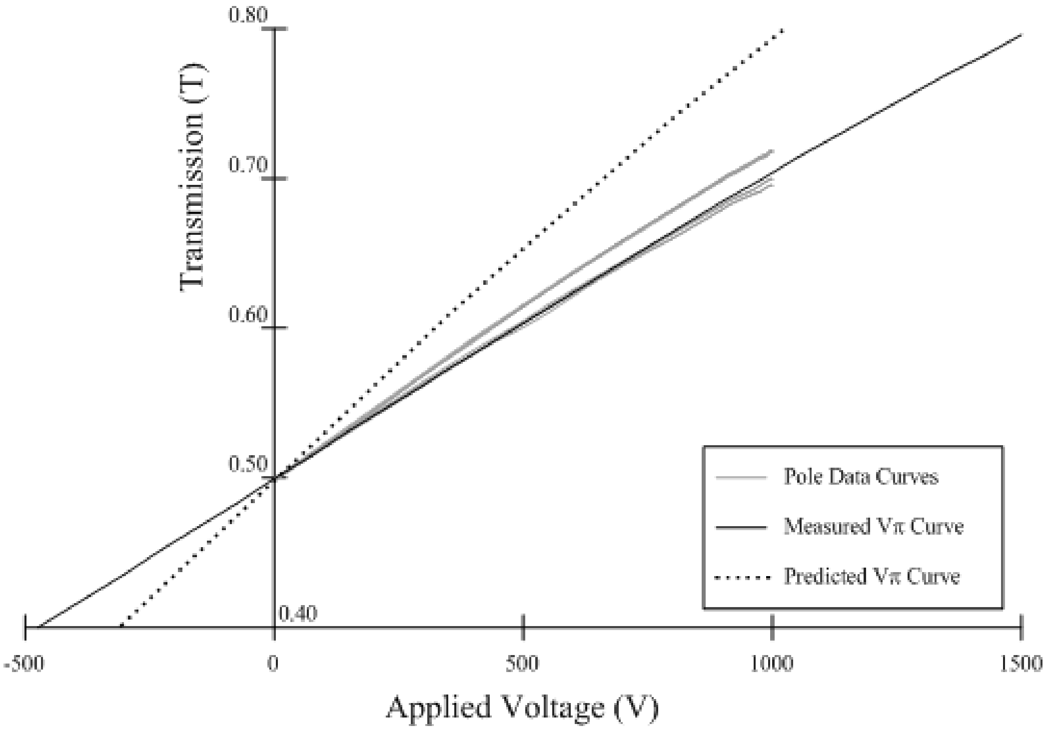

Figure (5-22) – Pole data and transmission curves for BSO at 1319 nm

The BSO sample at 1319 nm yielded a drift-corrected V_π of 15,013 volts with a measurement uncertainty of 5.3%. When compared to the predicted value of 10,019 volts at 1319 nm, we have an error of about 50%. This error is attributed to the low confidence level of our prediction and to the intrinsic optical activity of BSO.

The effects of optical activity on a double-pass bench-top experiment have been investigated in the Appendix at the end of this thesis. We have successfully used this analysis to show the effects of optical activity upon the 850 nm BSO experiment and to correct for these effects. An analysis of the 1319 nm experiment was not performed however, as the optical activity of BSO at 1319 nm was not found in the literature.

The values of V_π obtained for BSO at 850 nm are very uncertain. The locations of the poles and axes of the crystal were different at 850 nm than the ones found at 1319 nm. Figure (5-23) shows the locations of interested for BSO at 850 nm along with calculated response lobes for a double-pass sensor system.

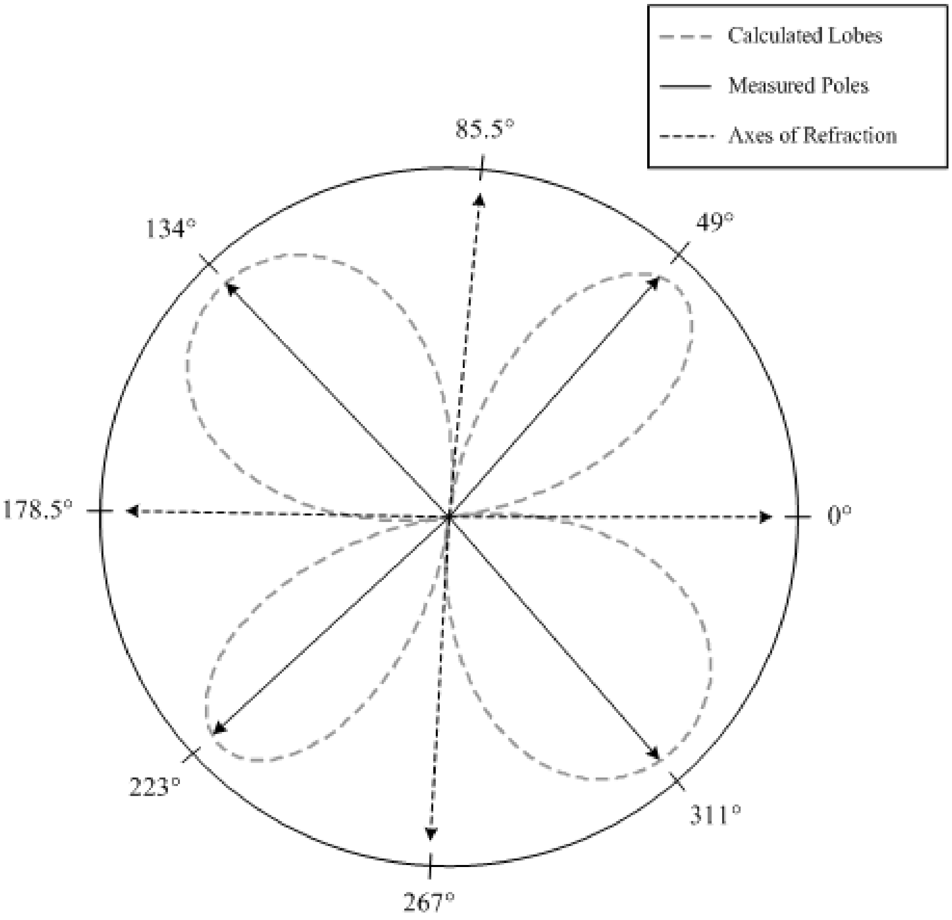

Figure (5-23) – BSO orientations of interest at 850 nm

When we examine the transmission curves generated using the measured and predicted half-wave voltages, we see a large amount of deviation. Figure (5-24) shows these curves and Table (5-11) presents the half-wave voltage found for BSO at

850 nm. The large standard deviation and uncertainty error are easy to see in the pole data curves shown in Figure (5-25).

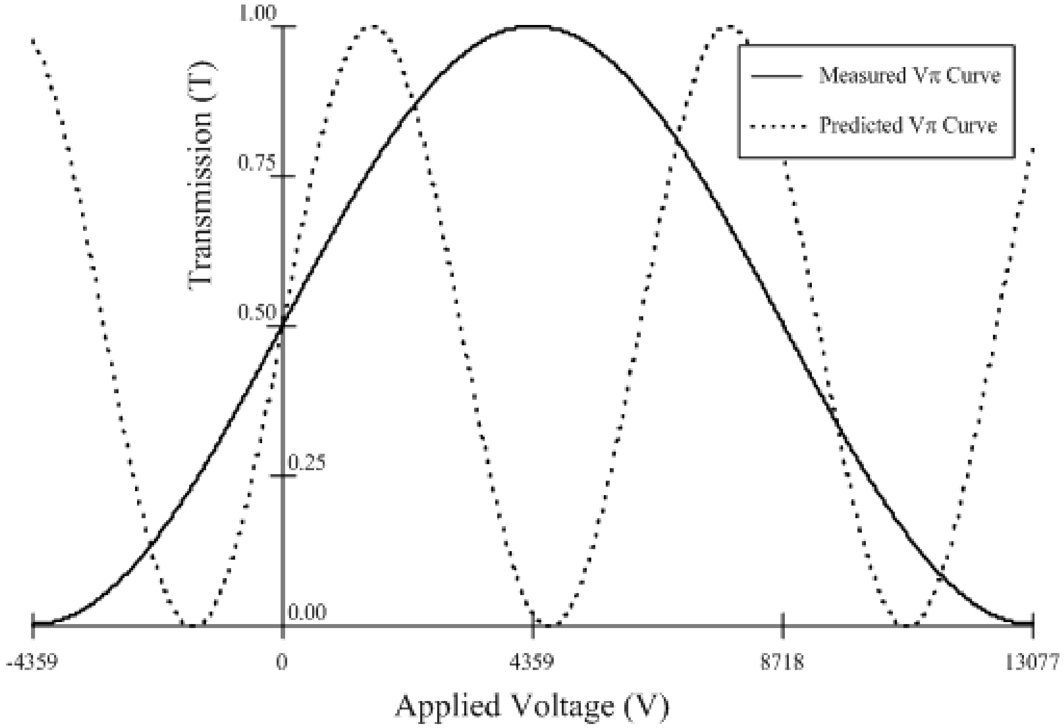

Figure (5-24) – Transmission curves for BSO at 850 nm

BSO – 850 nm	Raw Measured	Drift Correction
Median Vπ (V)	17456	17434
Standard Deviation (V)	4128	4097
Error (%)	23.7%	23.5%

Table (5-11) – BSO Results at 850 nm

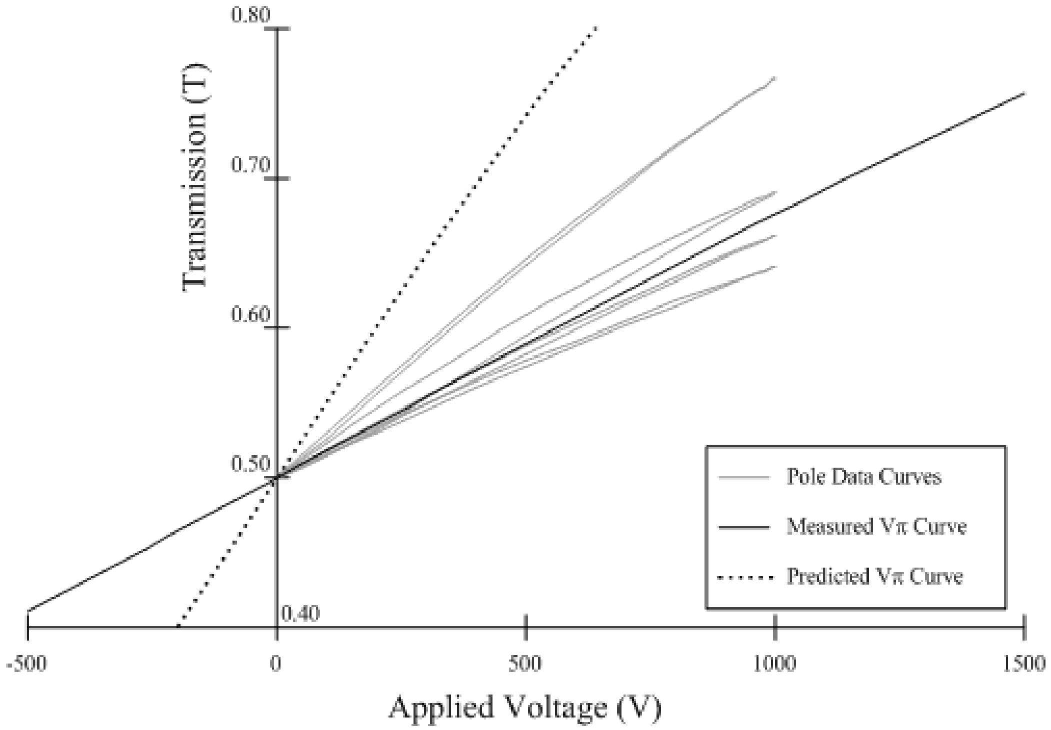

Figure (5-25) – Pole data and transmission curves for BSO at 850 nm

At 850 nm, the BSO sample was found to have a drift-corrected half-wave voltage of 17,434 volts with a measurement uncertainty of 23.5%. These values are about 180% larger than predicted.

The large error seen in the 850 nm BSO experiment is almost wholly attributed to the optical activity of BSO. A Jones calculus analysis of the optical activity of BSO at 850 nm has been performed in the Appendix to quantify the errors seen in this experiment. The end results of this analysis will now be presented and the reader is referred to the Appendix for a thorough description of the method used.

Using the Jones model for the optical activity of BSO at 850 nm, we were able to generate a sensor transmission curve that more closely follows the data we measured. Figure (5-26) shows the measured, predicted and calculated transmission curves for the 850 nm BSO experiment. Figure (5-27) shows how well the calculated transmission aligns to the data curves measured for BSO.

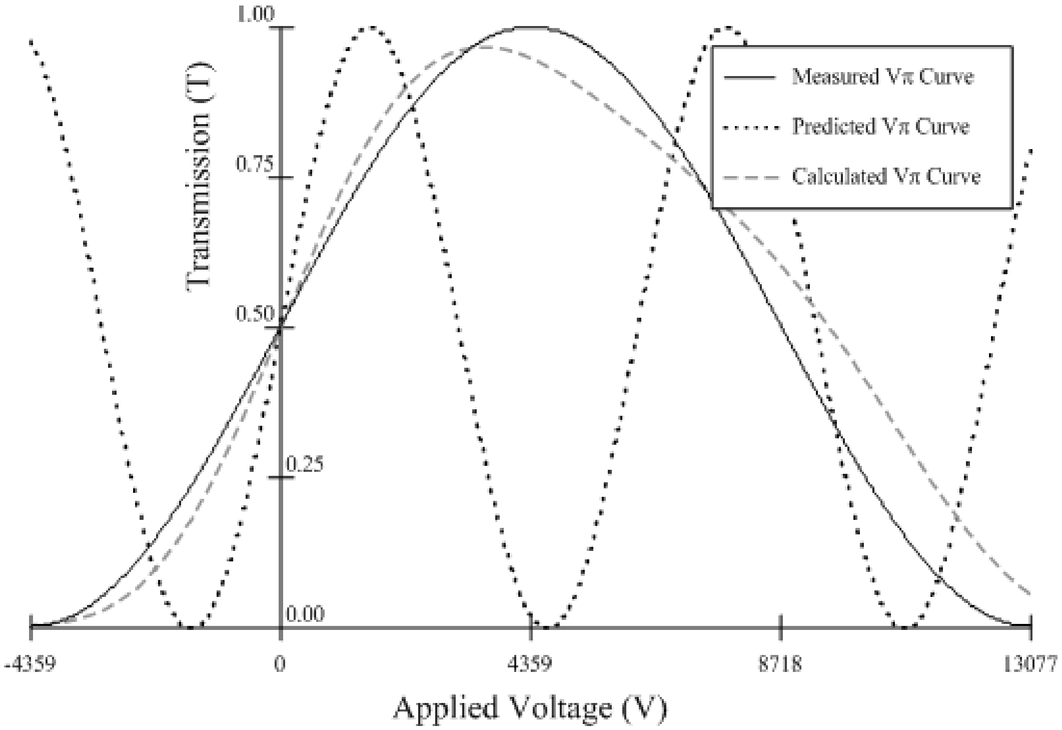

Figure (5-26) – Transmission curves for optically active BSO at 850 nm

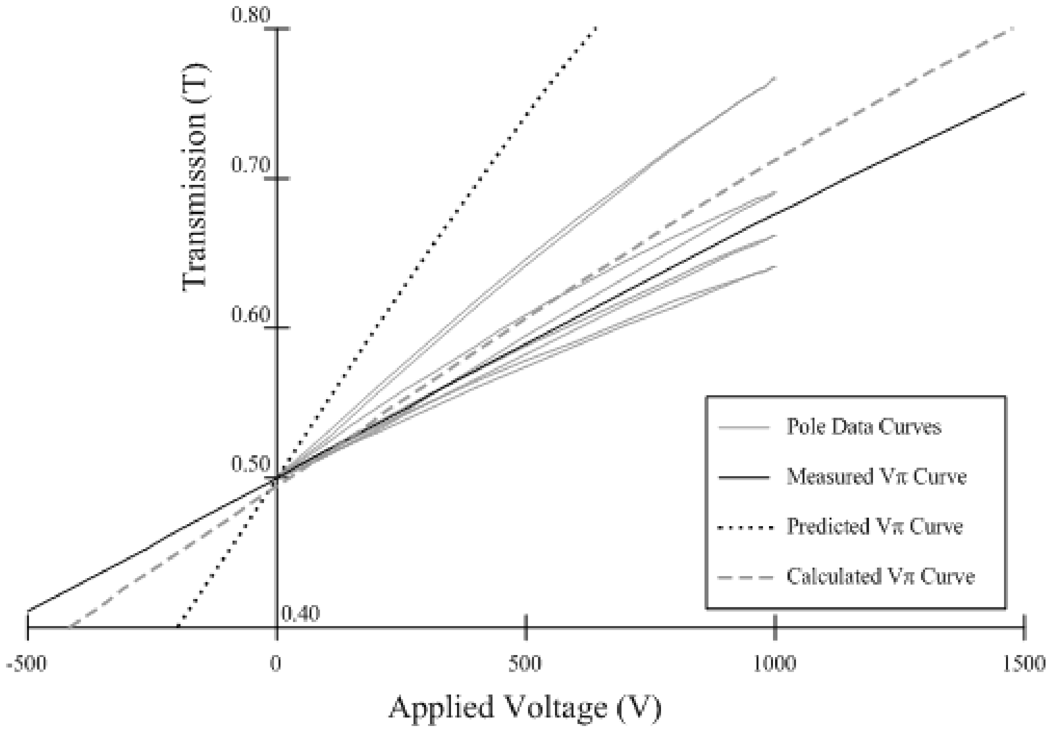

Figure (5-27) – Data curves for optically active BSO at 850 nm

We have used the Jones model for the BSO system to determine a corrected half-wave voltage of 7,025 volts for BSO at 850 nm. This value takes into account the effects of optical activity observed in this experiment. When compared to the originally predicted half-wave voltage for BSO at 850 nm, we find that our corrected value is only 13.1% off.

Sources of Error

While examining the data presented above, several sources of error were determined. The BGO crystal exhibits the least amount of total error. What little error BGO did demonstrate is likely the result of optical misalignment. Another likely source of error is thermal drift. We have already seen that the laser source drifts with temperature, however the receiver, waveplates and the Pockels cell itself are all thermally sensitive. Even though steps were taken to measure and correct for the source drift, the corrected data shows little improvement over the raw data. This could be due to random changes in the laser output polarization giving rise to false coupler readings at the reference detector, as the coupler is polarization sensitive. The thermal dependence of the receiver, waveplates and the Pockels cell were not investigated, however the reader is referred to the literature for the thermal dependence of electro-optic crystals.(20)

The large source of error witnessed in the ZnSe experiments is most likely attributed to an unknown gross measurement error. This experiment yielded consistently inaccurate results and it is recommended that the experiment be more carefully and thoroughly performed in the future.

The optical activity of BSO has been shown to be the primary culprit in the erroneous results obtained for the BSO crystal. BSO is reported to have an intrinsic optical rotatory power of approximately 12° per mm at 850 nm.(61) For our 10 mm crystal sample, this means the polarization angle was rotated by about 120°. The double-pass experiment corrected for this over-all rotation by passing the rotated light back through the crystal. However, the angle of the elliptically polarized light becomes increasingly misaligned to the maximum modulation orientation as it travels through the Pockels cell. This misalignment inside the crystal causes the phase added by the Pockels cell to diminish, which leads to false transmission readings for the sensor and in turn inaccurate calculations of the half-wave voltage. Further explanation of the errors associated with the BSO experiments and a mathematical analysis of the optical activity of BSO is given in the Appendix.

CHAPTER 6

CONCLUSIONS

Electro-optic crystals that exhibit the Pockels effect have been tested for performance and integrated into electro-optic voltage sensors used for noninvasive electron particle accelerator diagnostics. These sensors have been fielded on the second accelerator axis at DARHT and electro-optic sensor work is ongoing at Los Alamos National Laboratory in Los Alamos, New Mexico. New sensor designs and performance data for these sensors are available in the literature.(12,13,14,15)

Of the crystal samples tested for this research, BGO yielded the most promising results even though it was the least sensitive crystal. It demonstrated an average corrected half-wave voltage of 75,531 volts at 1319 nm and 46,832 volts at 850 nm. The results at 850 nm strongly compare to those obtained from the literature and the results at 1319 nm were measured to be within 10% of the value extrapolated using data from the literature. The BGO results measured in this research are added to those in Table (5-2) and are shown below in Figure (6-1). The results from this thesis and those reported of BGO's resilience in harsh environments(17,18,19) make it the best candidate for electro-optic voltage sensors for accelerator diagnostics.

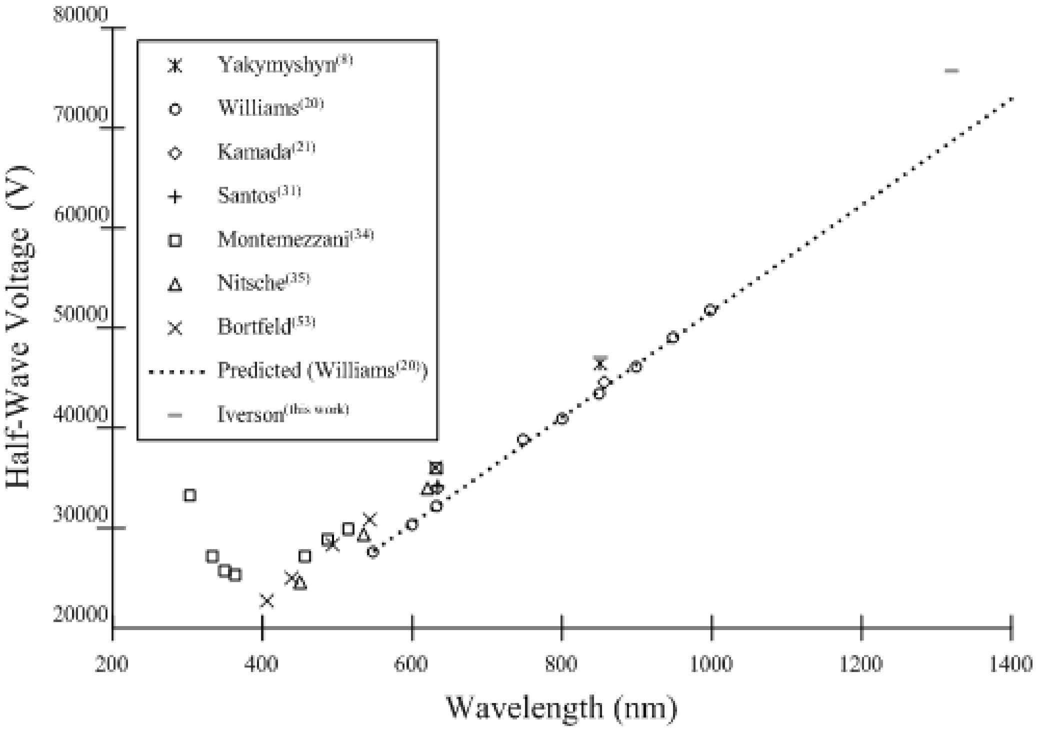

Figure (6-1) – BGO V_π data

Zinc selenide demonstrated an average corrected half-wave voltage of 43,513 volts at 1319 nm and 33,078 volts at 850 nm. The results obtained for ZnSe were found to be very different from what was expected based upon extrapolated values. Measurement errors are suspected to be the cause of this deviation. Regardless, ZnSe is proved to be a sensitive crystal when used for measuring voltages on the order of a few kilovolts. It is likely not a good candidate for electro-optic voltage sensors in accelerator diagnostics due to its low voltage nonlinearity. Further testing is warranted to determine the cause of the errors seen in this experiment. Figure (6-2) presents the ZnSe data from this research along with other half-wave voltages reported in the literature.

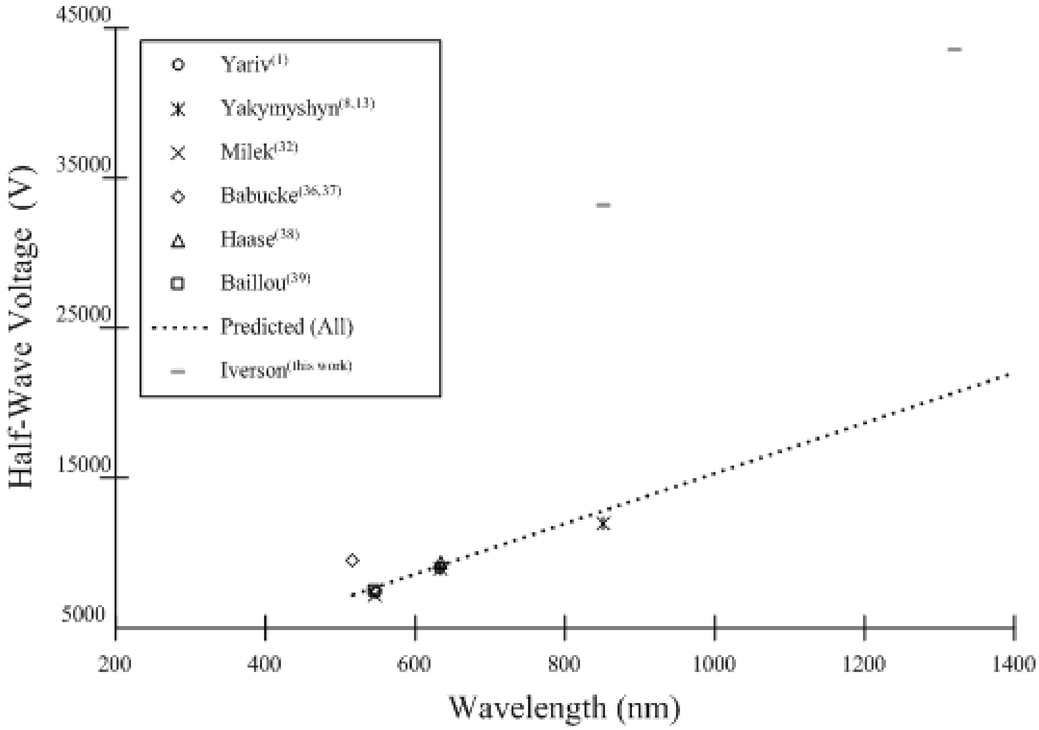

Figure (6-2) – ZnSe V_π data

Bismuth silicon oxide demonstrated a corrected half-wave voltage of 15,020 volts at 1319 nm and 7,025 volts at 850 nm. The half-wave voltage of BSO at 1319 nm was found to be 50% off of what was predicted. Upon careful analysis of the 850 nm experiment, the prediction deviation was reduced from 180% to about 13% when optical activity was taken into account. Although it was shown that the optical activity of BSO can be mathematically corrected for, this intrinsic optical property makes BSO a bad choice for electro-optic sensors. Figure (6-3) shows the results obtained for the BSO experiments along with the reported half-wave voltages given in the literature.

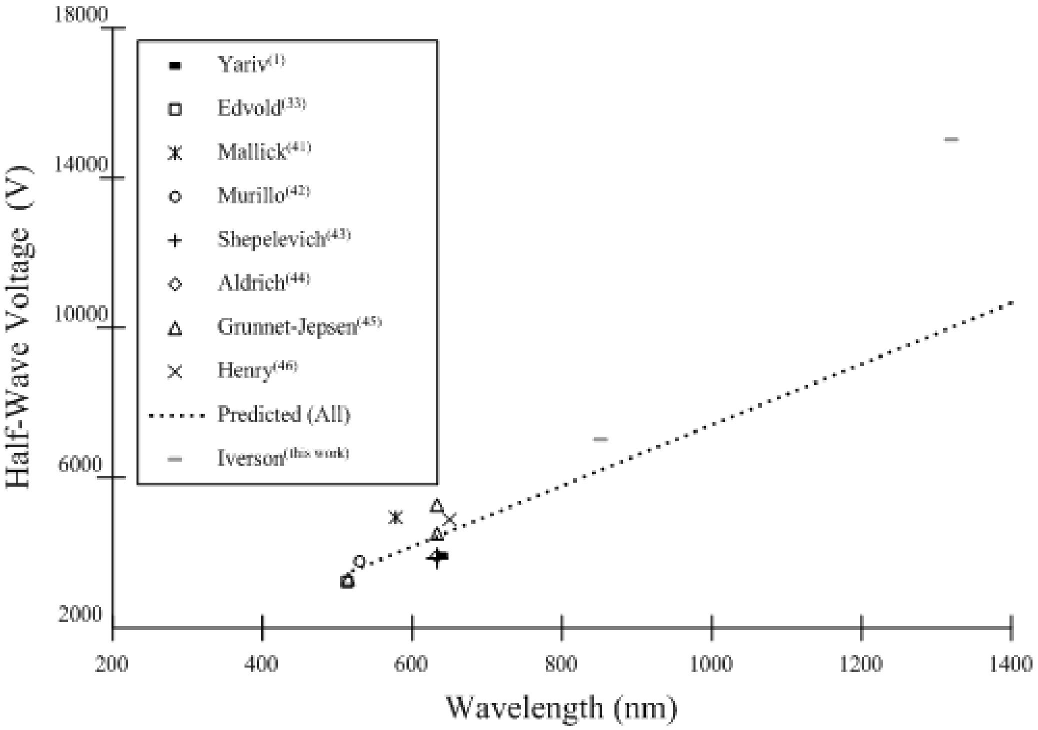

Figure (6-3) – BSO V_π data

An ancillary goal of this research was to compare the sensitivity of the three crystals to each other. Table (6-1) and Figure (6-4) presents the V_π values for the three crystals tested.

	BGO	**ZnSe**	**BSO**
λ = 1319 nm Half-wave Voltage (V)	75531	43513	15020
λ = 850 nm Half-wave Voltage (V)	46832	33078	7025

Table (6-1) – Thesis research results summary

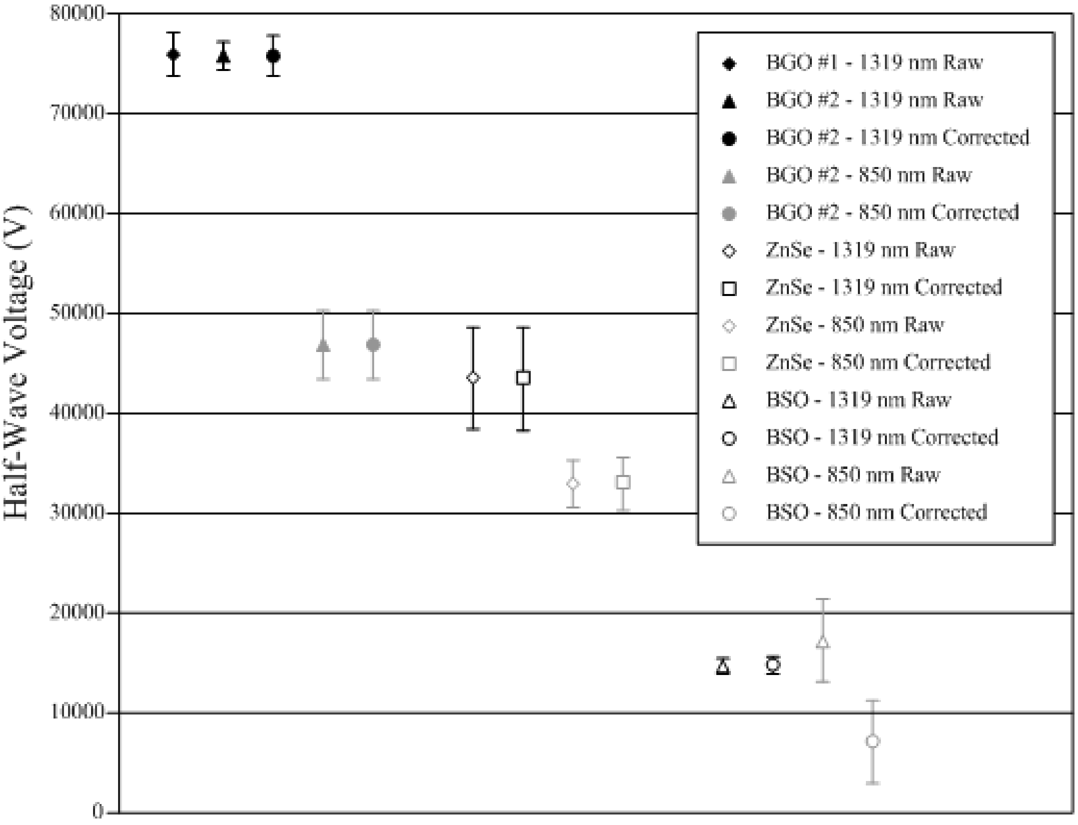

Figure (6-4) – Thesis research results summary

APPENDIX A

JONES CALCULUS

Bench Top Experiment Analysis

We are able to use a method called Jones calculus to describe the state of polarization of the single-pass and double-pass bench top experiments. We shall forgo most of the basics of Jones calculus and assume the reader has a base knowledge of this technique.

Figure (A-1) presents an equivalent optical configuration of the single-pass bench top experiment, where $\theta = 45°$. We shall describe mathematically, using Jones calculus, the state of polarization of the light as it passes through each optical element of this system.

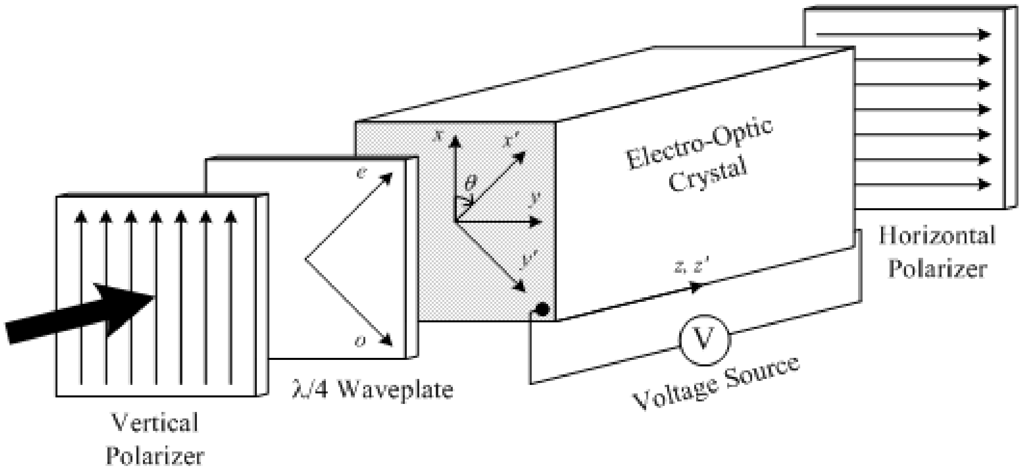

Figure (A-1) – Optical equivalent of the single-pass bench top experiment

Since a Jones vector that describes unpolarized light does not exist, we shall assume we have linearly polarized light, oriented to the *x* axis of the system, emerging from our fiber optic cable and traveling in the positive *z* direction. This is described by the normalized Jones vector

$$J_1 = \begin{bmatrix} 1 \\ 0 \end{bmatrix} \tag{A-1}$$

This light passes through a linear polarizer oriented to the x axis. This linear polarizer is described by the Jones matrix

$$T_{LP1} = \begin{bmatrix} 1 & 0 \\ 0 & 0 \end{bmatrix} \tag{A-2}$$

The Jones vector that describes the polarization state of the light after passing through this polarizer is given by

$$J_2 = T_{LP1} J_1 \tag{A-3}$$

which, upon substitution, becomes

$$J_2 = \begin{bmatrix} 1 \\ 0 \end{bmatrix} \tag{A-4}$$

The light remains linearly polarized along the x direction. It now passes through a quarter waveplate, or quarter-wave retarder, with its extraordinary axis of refraction aligned with the x' axis. This is described by the Jones matrix

$$T_{WR}(\theta,\phi) = \begin{bmatrix} \cos(\theta)^2 + \sin(\theta)^2 e^{-i\phi} & \cos(\theta)\sin(\theta)\left(1 - e^{-i\phi}\right) \\ \cos(\theta)\sin(\theta)\left(1 - e^{-i\phi}\right) & \sin(\theta)^2 + \cos(\theta)^2 e^{-i\phi} \end{bmatrix} \tag{A-5}$$

where ϕ is the amount of retardation and θ is the orientation of the extraordinary axis of refraction to the x axis. For this waveplate, $\phi = \pi/2$ and $\theta = 45°$. Transmission through this element is described by the Jones vector

$$J_3 = T_{WR}(\theta, \phi) J_2 \tag{A-6}$$

which leads to

$$J_3 = \begin{bmatrix} \frac{1}{2} - \frac{1}{2} i \\ \frac{1}{2} + \frac{1}{2} i \end{bmatrix} \tag{A-7}$$

After passing through the quarter waveplate, the linearly polarized light is now right hand circularly polarized. The next element in the single-pass bench top experiment is the Pockels cell. We shall assume that the ITO coated windows do not change the polarization of the light. The Pockels cell, however, acts as a variable waveplate with the amount of retardation, Γ, primarily determined by the voltage applied to the crystal. This retardation is given in Equation (2-31) in the second chapter, but we shall rewrite it as

$$\Gamma = \frac{\pi V}{V_\pi} \tag{A-8}$$

to include the half-wave voltage of the crystal. The crystallographic axes of the Pockels cell are oriented to the x and y axes shown in Figure (A-1). When an electric field is applied to the crystal, the crystal becomes birefringent and develops ordinary and extraordinary axes of refraction. The extraordinary axis of refraction is aligned to the x' axis shown in Figure (A-1). The Jones matrix that describes a Pockels crystal with this orientation is given as

$$T_{PC}(\theta,\Gamma) = \begin{bmatrix} \cos(\theta)^2 + \sin(\theta)^2 e^{-i\Gamma} & \cos(\theta)\sin(\theta)(1-e^{-i\Gamma}) \\ \cos(\theta)\sin(\theta)(1-e^{-i\Gamma}) & \sin(\theta)^2 + \cos(\theta)^2 e^{-i\Gamma} \end{bmatrix} \tag{A-9}$$

The light exiting the Pockels cell is now right elliptically polarized with the amount of ellipticity determined by the voltage applied to the crystal. The Jones vector that describes this polarization is given as

$$J_4 = T_{PC}(\theta,\Gamma) J_3 \tag{A-10}$$

which is

$$J_4 = \begin{bmatrix} \frac{1}{2} - \frac{1}{2} ie^{\left(-i\frac{\pi V}{V_\pi}\right)} \\ \frac{1}{2} + \frac{1}{2} ie^{\left(-i\frac{\pi V}{V_\pi}\right)} \end{bmatrix} \tag{A-11}$$

This partially elliptical light passes through another linear polarizer, this one oriented to the y axis. Its Jones matrix is given by

$$T_{LP2} = \begin{bmatrix} 0 & 0 \\ 0 & 1 \end{bmatrix} \tag{A-12}$$

The Jones vector that describes the light after it passes through this linear polarizer is

$$J_5 = T_{LP2} J_4 \tag{A-13}$$

or

$$J_5 = \begin{bmatrix} 0 \\ \frac{1}{2} + \frac{1}{2} i e^{\left(-i\frac{\pi V}{V_\pi}\right)} \end{bmatrix} \tag{A-14}$$

after substitution. This Jones vector describes the polarization state of the light after it has passed through the single-pass bench top experiment. The second linear polarizer has converted the elliptical voltage dependant polarization into linearly polarized light along the *y* direction where the intensity of the light is now dependant upon the voltage applied to the crystal.

Figure (A-2) shows a configuration that is optically equivalent to the double-pass bench top experiment. For this analysis we shall consider the polarizing beamsplitting cube as a linear polarizer to reduce the complexity of the Jones analysis.

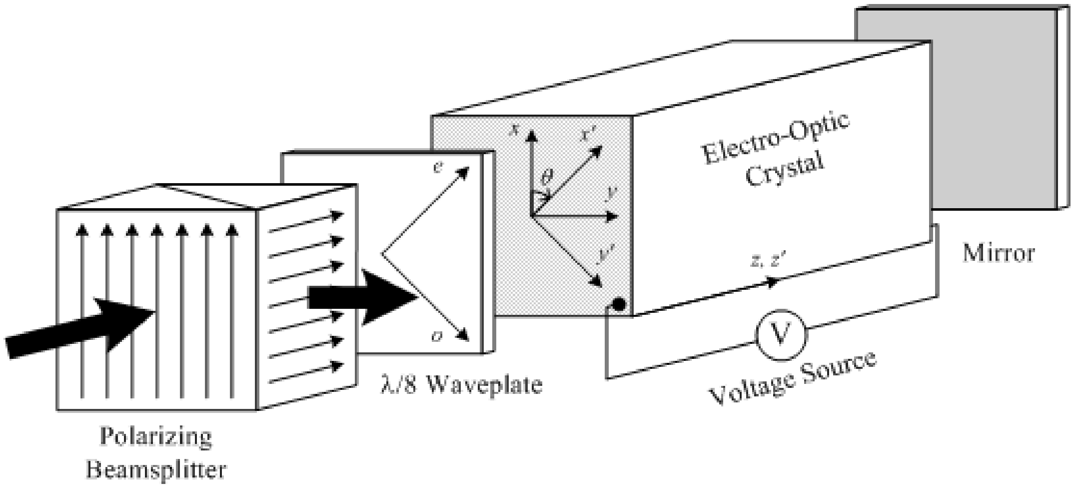

Figure (A-2) - Optical equivalent of the double-pass bench top experiment

The Jones calculus for the double-pass bench top experiment is only slightly different from that of the single-pass configuration. We shall again start with linearly polarized light aligned to the x axis, which is given by Equation (A-1). This light passes through a linear polarizer oriented to the x axis, given by Equation (A-2). The Jones vector describing the light after passing through the polarizer is shown in Equations (A-3) and (A-4). Instead of passing through a quarter waveplate, the light now passes through an eighth waveplate with its extraordinary axis of refraction oriented to the x' axis shown in Figure (A-2). This waveplate is described by the same Jones matrix given in Equation (A-5), only now $\phi = \pi/4$. The Jones vector for the light after passing through the wave retarder is the same as Equation (A-6), but after substitution becomes

$$J_3 = \begin{bmatrix} \frac{1}{2} + \frac{1}{4}\sqrt{2} - \frac{1}{4}i\sqrt{2} \\ \frac{1}{2} - \frac{1}{4}\sqrt{2} + \frac{1}{4}i\sqrt{2} \end{bmatrix} \tag{A-15}$$

The light then passes through the electro-optic crystal described by the Jones matrix in Equation (A-9). This leads to the same expression given by Equation (A-10) but yields

$$J_4 = \begin{bmatrix} \frac{1}{2} + \frac{1}{4}\sqrt{2}e^{\left(-i\frac{\pi V}{V_\pi}\right)}(1 - i)) \\ \frac{1}{2} - \frac{1}{4}\sqrt{2}e^{\left(-i\frac{\pi V}{V_\pi}\right)}(1 - i)) \end{bmatrix} \tag{A-16}$$

after substitution.

Next, we must investigate the effects of a mirror to the state of polarization of the light. Upon a normal incidence reflection from a mirror, both orthogonal electric field vectors of the polarized light switch sign. However, we must now be aware that the Jones vector on the return path through the polarization optics is described by a left handed system, where we have been working in a right handed coordinate system. To correct for this, we write the Jones matrix for a reflector as

$$R = \begin{bmatrix} 1 & 0 \\ 0 & -1 \end{bmatrix} \tag{A-17}$$

so that the right handed coordinate system is maintained on the return path through the system. We must now take care in describing the orientation of the wave retarders, as we have undergone a 180° phase shift of the x axis, $x = -x$. To account for this phase shift, we set $\theta = -45°$ when describing the orientation of the Pockels cell and eighth waveplate to the x axis on the second pass through each component.

The Jones vector of the light after reflecting off of the mirror is given by

$$J_5 = RJ_4 \tag{A-18}$$

and expands to

$$J_5 = \begin{bmatrix} \frac{1}{2} + \frac{1}{4}\sqrt{2}e^{\left(-i\frac{\pi V}{V_\pi}\right)}(1-i)) \\ -\frac{1}{2} + \frac{1}{4}\sqrt{2}e^{\left(-i\frac{\pi V}{V_\pi}\right)}(1-i)) \end{bmatrix} \tag{A-19}$$

We now pass through the Pockels crystal for the second time. The Jones vector for this is given by

$$J_6 = T_{PC}(-\theta, \Gamma)J_5 \tag{A-20}$$

which expands to

$$J_6 = \begin{bmatrix} \frac{1}{2} + \frac{1}{4}\sqrt{2}e^{\left(-i\frac{2\pi V}{V_\pi}\right)}(1-i)) \\ -\frac{1}{2} + \frac{1}{4}\sqrt{2}e^{\left(-i\frac{2\pi V}{V_\pi}\right)}(1-i)) \end{bmatrix} \tag{A-21}$$

This light now passes back through the eight waveplate, denoted by

$$J_7 = T_{WR}(-\theta, \phi)J_6 \tag{A-22}$$

which becomes

$$J_7 = \begin{bmatrix} \frac{1}{2} - \frac{1}{2}ie^{\left(-i\frac{2\pi V}{V_\pi}\right)} \\ -\frac{1}{2} - \frac{1}{2}ie^{\left(-i\frac{2\pi V}{V_\pi}\right)} \end{bmatrix} \tag{A-23}$$

The second pass through the linear polarizer given by the Jones matrix in Equation (A-12) is expressed by the Jones vector

$$J_8 = T_{LP2}J_7 \tag{A-24}$$

and becomes

$$J_8 = \begin{bmatrix} 0 \\ -\frac{1}{2} - \frac{1}{2}ie^{\left(-i\frac{2\pi V}{V_\pi}\right)} \end{bmatrix} \tag{A-25}$$

which is the polarization state of the light exiting the double-pass bench top experiment. This light is linearly polarized along the *y* axis with its intensity dependant upon the voltage applied to the electro-optic crystal.

Sensor Design Analysis

The first voltage sensor design can be analyzed using Jones calculus in a manner almost identical to the double-pass bench top experiment. The polarization analyzer in this sensor is the same *x*-axis oriented linear polarizer used to initially polarize the light entering the sensor. If we swap the Jones matrix for the linear polarizer given in Equation (A-24) with the Jones matrix of Equation (A-2) we shall have aligned polarizers. This will result in a Jones vector for the first sensor design of the following.

$$J_8 = \begin{bmatrix} \frac{1}{2} - \frac{1}{2} ie^{\left(-i\frac{2\pi V}{V_\pi}\right)} \\ 0 \end{bmatrix} \tag{A-26}$$

The analysis of the double-pass bench top experiment happens to be identical to the analysis of the second voltage sensor design. We shall therefore forgo repeating this work and simply state that the Jones vector for the second sensor design is given as Equation (A-25).

BSO Analysis

We are also able to use Jones calculus to analyze the errors seen for BSO at 850 nm in the double-pass bench top experiment intended to measure V_π for the crystal. We are able to show how the optical activity of BSO affected the experimental measurements and use the Jones calculus model to correct for the errors due to optical activity and report a newly corrected half-wave voltage for BSO at 850 nm.

The optical activity in BSO causes the polarization angle of the light passing through it to rotate. This property is commonly called circular birefringence and is a naturally occurring phenomenon in BSO. Because the principal axes of polarization are rotated as they travel through the BSO, they become misaligned to the orientation within the electro-optic crystal that yields the largest linear birefringence. Because of this, attempts to measure the linear birefringence become exceedingly complicated. In fact, for crystals with optical activity the notion of half-wave voltage is inappropriate and only mathematically attained through the use of Equation (2-37), the Pockels coefficient and index of refraction.(40,51) Optical activity also makes the measurement of the Pockels coefficient challenging, evidenced by Figure (A-3), nevertheless techniques have been reported in the literature.(40,45,46,47,48,49,51)

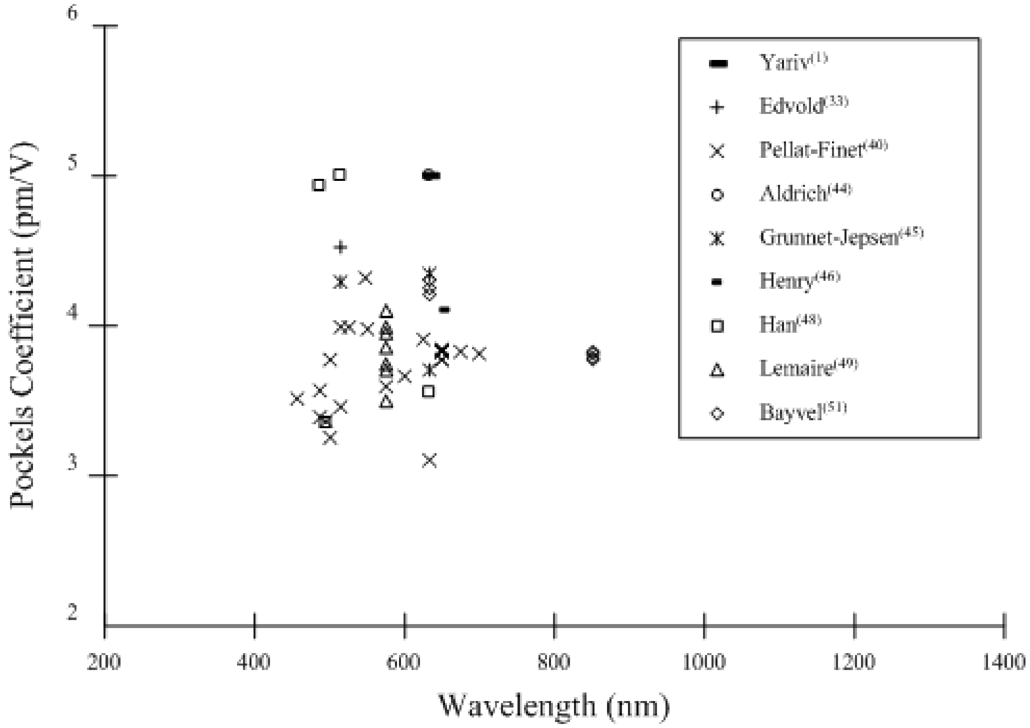

Figure (A-3) – Reported Pockels coefficients for BSO

We are able to describe the behavior of optical activity as a polarization rotation given by the Jones matrix

$$T_{PR}(\rho) = \begin{pmatrix} \cos(\rho) & -\sin(\rho) \\ \sin(\rho) & \cos(\rho) \end{pmatrix} \tag{A-27}$$

where ρ is the amount of rotation of the principal axes of polarization. We are able to recycle most of the double-pass bench top experiment work above for an analysis of the BSO V_π measurement. The optical configuration of this analysis is identical to what is shown in Figure (A-2). The only difference is the Jones description of the Pockels cell. We shall begin our analysis with Equation (A-15), which describes the polarization state of the light after passing through the eighth waveplate. From this point, the light enters the BSO crystal, however, because the crystal is optically active we must insert Equation (A-27) into the Jones calculus.

In order to accurately describe the state of polarization of the light as it passes through the crystal, we cannot simply state

$$J_4 = T_{PC}(\theta, \Gamma) T_{PR}(\rho) J_3 \tag{A-28}$$

as this describes a rotation of polarization before passing through the Pockels cell. Instead, we shall incrementally break down the amount of rotation due to optical activity and account for the amount of linear birefringence given by the Pockels cell at each increment. As we make the increment smaller and smaller, we converge to an accurate description of the polarization state of the light exiting the BSO crystal. It was found mathematically that choosing an increment of 1/1000 provided a convergent Jones vector. The BSO crystal that was tested measured 10 mm in length, yielding an incremental slice of 10 μm. For each 10 μm slice, the circular and linear birefringence are calculated and a Jones vector summation is determined for one pass through the entire optically active crystal. This summation is given by

$$J_4 = \left[T_{PC}\left(\theta, \frac{\Gamma}{1000}\right) T_{PR}\left(\frac{\rho}{1000}\right) \right]^{1000} J_3 \tag{A-29}$$

which represents the polarization state of the light just before the reflector. The Jones matrix for the state of polarization after the reflector is the same as that given by Equation (A-18). The second trip through the Pockels cell yields a Jones vector of

$$J_6 = \left[T_{PC}\left(-\theta, \frac{\Gamma}{1000}\right) T_{PR}\left(\frac{\rho}{1000}\right) \right]^{1000} J_5 \tag{A-30}$$

The light then again passes through the eighth waveplate, denoted by the Jones vector in Equation (A-22). The state of polarization of the light exiting the linear polarizer is described by Equation (A-24). A symbolic representation of this Jones vector, like the one in Equation (A-25) is not feasible, given the number of matrices in this vector, however, we are able to describe the entire system by a Jones vector containing the Jones matrices for each optical element. This vector is given by

$$\begin{aligned} J_8 = T_{LP2} T_{WR}(-\theta, \phi) \left[T_{PC}\left(-\theta, \frac{\Gamma}{1000}\right) T_{PR}\left(\frac{\rho}{1000}\right) \right]^{1000} R \\ \left[T_{PC}\left(\theta, \frac{\Gamma}{1000}\right) T_{PR}\left(\frac{\rho}{1000}\right) \right]^{1000} T_{WR}(\theta, \phi) T_{LP1} J_1 \end{aligned} \tag{A-31}$$

Using the above equation, we are able to numerically analyze the effects of optical activity on an electro-optic V_π measurement. We shall evaluate the BSO experiment at 850 nm where its optical activity has been reported as $\rho_o = 12°/\text{mm}$.(61) This yields a total rotation of $\rho = 120°$ for a 10 mm long crystal. For the value of the half-wave voltage used in numerically analyzing the BSO experiment, we shall use the predicted value of 6,211 volts. Our choice in using this half-wave voltage for the numerical analysis is geared toward determining sensor response when optical activity is taken into account. If done correctly, we would hope to use the predicted half-wave voltage to generate a transmission curve that better approximates the data curves measured in the BSO experiment at 850 nm.

The output of the Jones vector in Equation (A-31) is a two element complex matrix representing the amplitude and phase of the light. In order to find the intensity of the light we must apply the following formula.

$$I_T = \left| J \cdot \begin{pmatrix} 1 \\ 0 \end{pmatrix} \right|^2 + \left| J \cdot \begin{pmatrix} 0 \\ 1 \end{pmatrix} \right|^2 \tag{A-32}$$

where I_T is the optical transmission through the sensor system and J is the Jones vector describing the system. We can substitute Equation (A-31) into the above equation and plot the sensor transmission as a function of applied Pockels voltage given θ, ϕ, Γ and ρ. When $\rho = 0$, we will generate a transmission curve identical to the one shown in Figure (3-8) for the transmission through a double-pass sensor configuration with crossed polarizers. If we account for ρ, we can visually determine the effects of optical activity by comparing the transmission curve through an optically active sensor system to the transmission curve of a non-optically active system. To do this, we can add the calculated optically active transmission curve to the measured and predicted transmission curves of BSO at 850 nm given in Figure (5-24). This new comparative plot is shown in Figure (A-4) where the black dotted curve and solid black curve represents the predicted and measured transmission curves respectively through the system with optical activity ignored. The grey dashed-line curve represents the transmission through the same system but with optical activity taken into account.

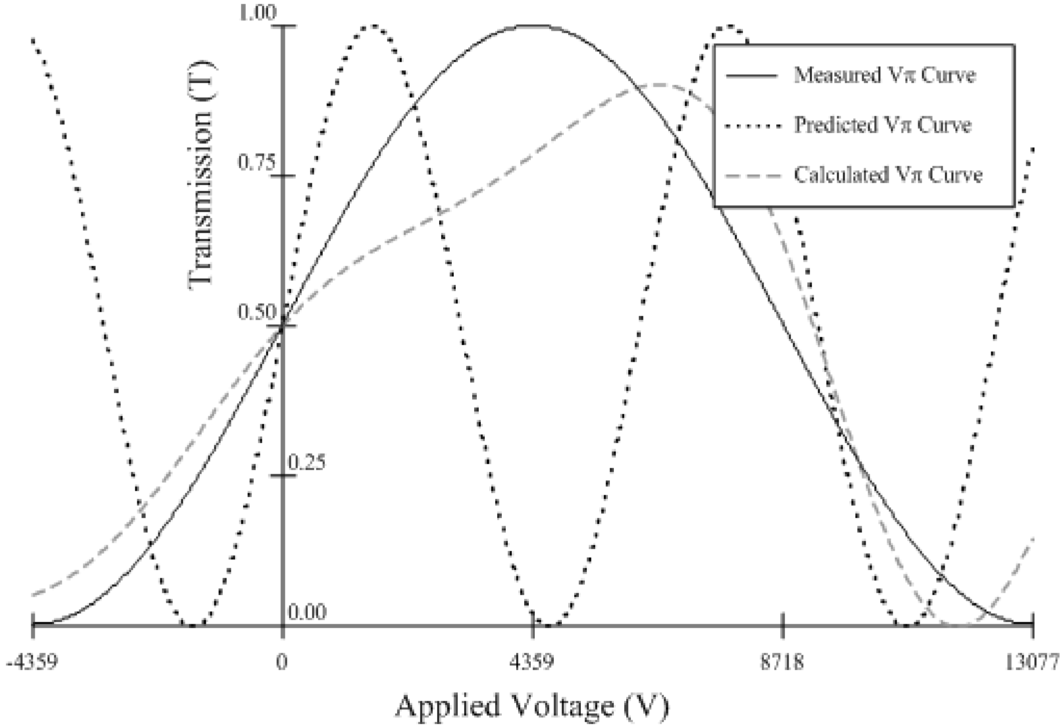

Figure (A-4) – Transmission curves of optically active BSO at 850 nm

We can add our newly calculated transmission curve to Figure (5-25), the plot showing the actual data curves at 850 nm, to see if our calculations are correct. As we can see from this figure, our calculations do not seem to align well with the measured data curves. This leads us to further investigate the behavior of this optically active system.

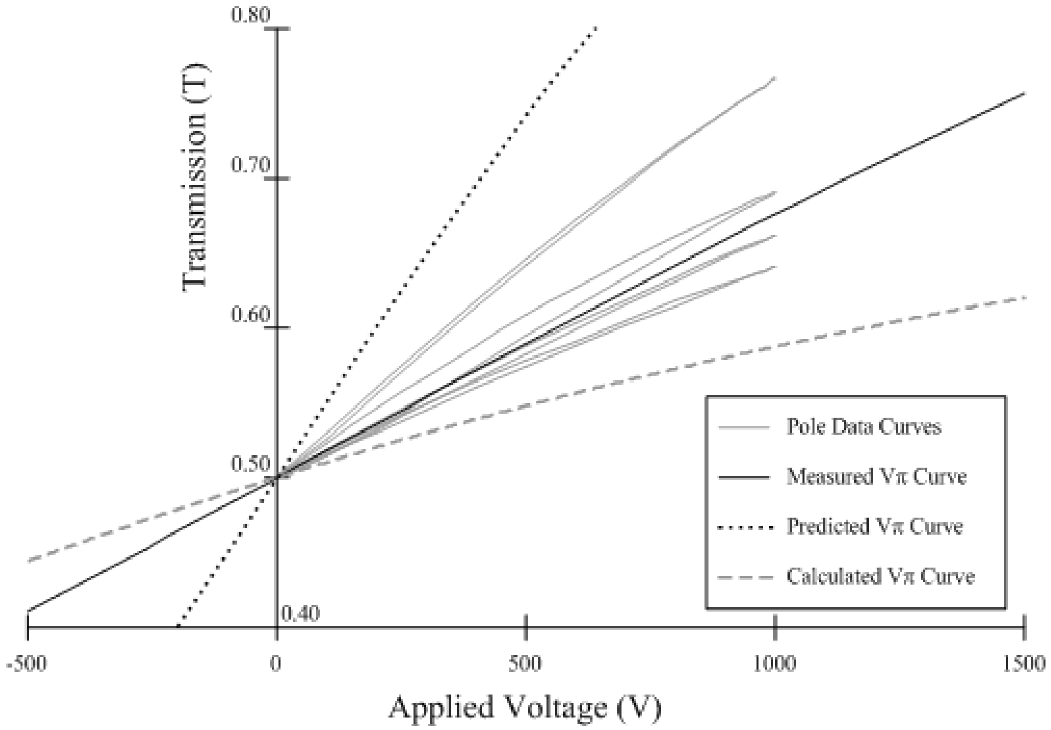

Figure (A-5) – Data curves of optically active BSO at 850 nm

The analysis above makes the assumption that the optical axes of the BSO crystal are aligned to the other optical components of the system as one would align a normal cubic crystal. As we are beginning to see, BSO is not a normal cubic crystal. In light of this, we have plotted the optically active sensor response as a function of rotational alignment of the crystal. A normal double-pass cubic crystal system should produce response lobes like those in Figure (5-23). However, when optical activity is taken into account, we find that the response lobes change shape and orientation. Our half-wave voltage measurements were made at the locations of greatest response and were thus arbitrarily aligned to the other optical components of the bench-top experiment. If we use the new orientation of greatest response taken from the calculated response lobes of Figure (A-6), we can generate new transmission curves that should better simulate our actual measurement configuration.

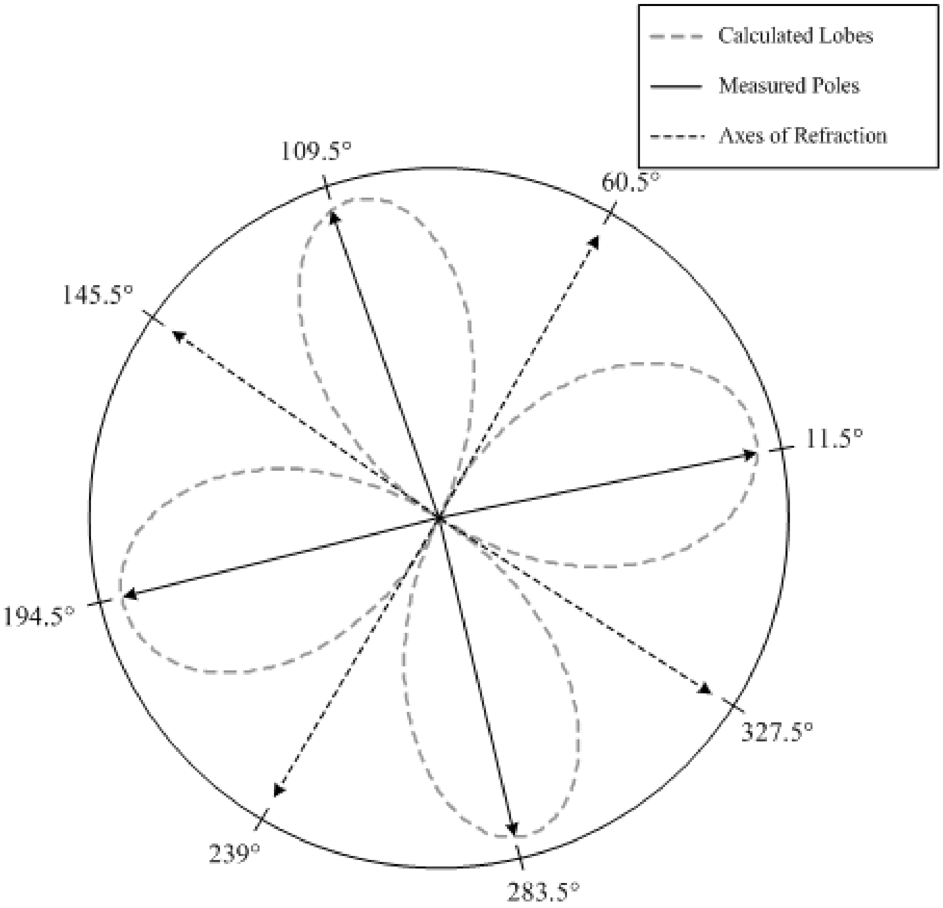

Figure (A-6) – Optically active BSO orientations of interest at 850 nm

Instead of aligning the BSO crystal to $\theta = 45°$ to the x axis of the system, we find that the BSO sensor will have the greatest response when $\theta = 105.5°$. Using this optimized alignment, we can generate transmission curves to see if our new calculations better approximate that which was measured. Figure (A-7) shows the newly calculated transmission curve with the measured and predicted transmission curves of BSO at 850 nm. It is easy to see that we have calculated a transmission curve that closely approximates the measured transmission curve measured in the BSO experiment at 850 nm. It is even more evident in Figure (A-8), which shows our optimized calculation of the transmission through optically active BSO with the measured data curves.

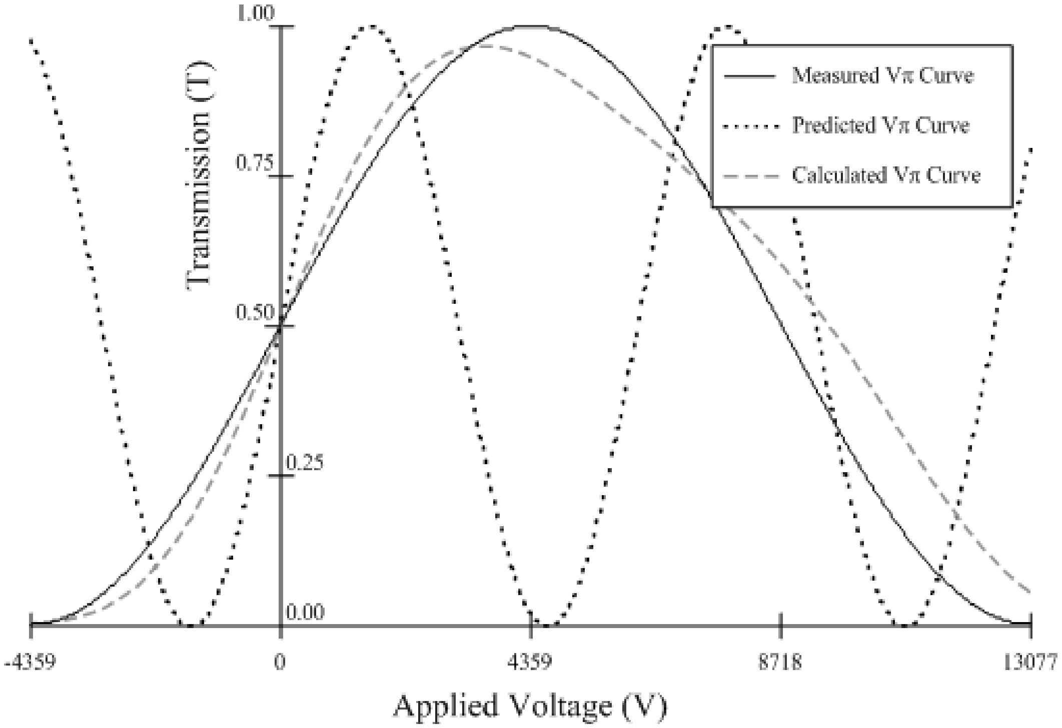

Figure (A-7) – Transmission of optimized optically active BSO at 850 nm

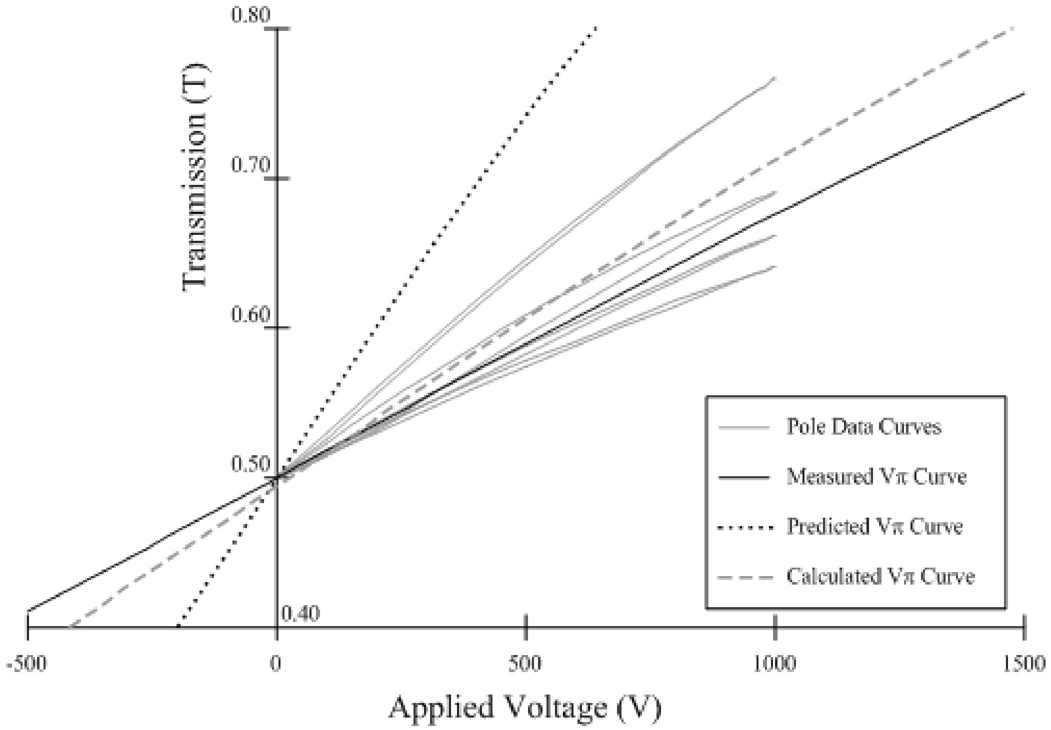

Figure (A-8) – Data curves of optimized optically active BSO at 850 nm

As you can see from the analysis above, optical activity not only affects the sensitivity of the system but also affects its linearity. The circular birefringence caused by the optical activity washes out the induced linear birefringence, leading to false measurements of the half-wave voltage for BSO.

We are able to use this Jones model of the optically active BSO system to estimate a corrected half-wave voltage for BSO at 850 nm. We find that our model converges upon the measured transmission curve when the half-wave voltage is approximately 7,025 volts. This means that in the absence of optical activity, we would have measured a half-wave voltage of 7,025 volts for BSO at 850 nm. This value would have been 13.1% larger than the predicted half-wave voltage of

6,211 volts. To further illustrate, we have plotted the reported values with our newly corrected half-wave voltage for BSO at 850 nm in Figure (A-9).

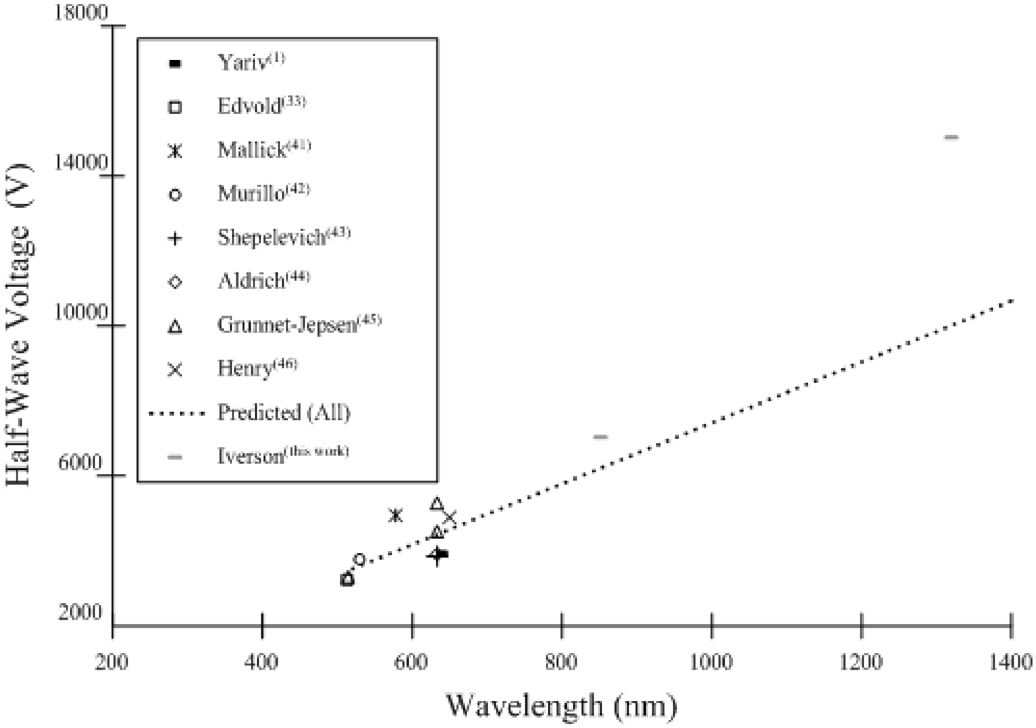

Figure (A-9) – Updated BSO V_π data

As far as the author knows, the optical activity of BSO has not been reported at 1319 nm. We recommend further study of BSO at longer wavelengths if the reader is interested. For the purposes of this thesis, in which we investigated the linear electro-optic effect as it applies to voltage sensors, BSO is not a good choice due to its intrinsic optical activity.

BIBLIOGRAPHY

(1) Yariv, A., Yeh, P., *Optical Waves in Crystals*, John Wiley and Sons, Inc., New York, NY, 1984.

(2) Saleh, B.E.A., Teich, M.C., *Fundamentals of Photonics*, John Wiley and Sons, Inc., New York, NY, 1991.

(3) Hecht, J., *Understanding Fiber Optics*, 2nd Edition, Howard W. Sams & Co., India, 1997

(4) Yariv, A., *Optical Electronics in Modern Communications*, Fifth Edition, Oxford University Press, Inc., New York, NY, 1997.

(5) Ito, A., Ohta, K., Yagi, T., Shinagawa, M., Nagatsuma, T., Yamada, J., *Probe for Electro-Optic Sampling Oscilloscope*, United States Patent #6,288,531, September 11, 2001.

(6) Miller, R., *Electro-Optical Voltage Measuring System Incorporating a Method and Apparatus to Derive the Measured Voltage Waveform from Two Phase Shifted Electrical Signals*, United States Patent #4,904,931, February 27, 1990.

(7) Bohnert, K., Nehring, J., *Method and Device for the Optical Determination of a Physical Quantity*, United States Patent #5,715,058, February 3, 1998.

(8) Yakymyshyn, C.P., Brubaker, M.A., Johnston, P.M., Reinbold, C., *Manufacturing Challenges of Optical Current and Voltage Sensors for Utility Applications*, Proceedings of SPIE, Vol. 3201, pp 2-19.

(9) Jaeger, N., Chavez, P., Cherukupalli, S., Polovick, G., *Method and Apparatus for Measuring Voltage using Electric Field Sensors*, United States Patent #6,252,388, June 26, 2001.

(10) Ferianis, M., *Optical Techniques in Beam Diagnostics*, Proceedings of the 1998 European Particle Accelerator Conference, Stockholm, 1998, pp 159-163.

(11) Tsang, T., Castillo, V., Larsen, R., Lazarus, D.M., Nikas, D., Ozben, C., Semertzidis, Y.K., Srinivasan-Rao, T., Kowalski, L., *Electro-Optic Measurements of Picosecond Bunch Length of a 45 MeV Electron Beam,* Journal of Applied Physics, Vol. 89, No. 9, May 2001, pp 4921-4926.

(12) Brubaker, M.A., Yakymyshyn, C.P., Iverson, A.J., VandeVeegaete, I.E., *A Prototype Optical Voltage Sensor for Accelerator Diagnostic Applications*, Proceedings of the 12th IEEE International Pulsed Power Conference, Monterey, CA, 1999, pp 619-622.

(13) Brubaker, M.A., Yakymyshyn, C.P., *Pockels Cell Voltage Probe for Noninvasive Electron Beam Measurements*, Applied Optics, Vol. 39, No. 7, March 2000, pp 1164-1167.

(14) Brubaker, M.A., Yakymyshyn, C P., *An Electro-Optic Voltage Sensor for Electron Beam Position and Current Monitoring*, IEEE Transactions on Plasma Science, Vol. 28, No. 5, October 2000, pp 1440-1444.

(15) Brubaker, M.A., Ekdahl, C.A., Yakymyshyn, C.P., *Electro-Optic Beam Position and Pulsed Power Monitors for the Second Axis of DARHT*, Proceedings of the 2001 Particle Accelerator Conference, Chicago, IL, 2001, pp 534-538.

(16) Burns, M.J., Carlsten, B., Davis, H., Ekdahl, C., Fortgang, C., McCuistain, B., Merrill, F., Nielsen, K., Wilkinson, C., Chow, K., Fawley, W., Rutkowski, H., Waldron, W., Yu, S., Caporaso, G., Chen, Y., Cook, E., Sampayan, S., Watson, J., Westenskow, G., Hughes, T., *Status of the DARHT Phase 2 Long-Pulse Accelerator*, Proceedings of the 2001 Particle Accelerator Conference, Chicago, 2001, pp 325-329.

(17) Sahu, S.K., Peng, K.C., Huang, H.C., Wang, C.H., Change, Y.H., Hou, W.S., Ueno, K., Chou, F.I., Wei, Y.Y., *Radiation Hardness of Undoped BGO Crystals*, Nuclear Instruments & Methods in Physics Research, Sect. A, Vol. 388, 1997, pp 144-148

(18) Peng, K.C., Wang, M.Z., Wang, C.H., Ueno, K., Huang, H.C., Chang, Y.H., Chou, F.I., Hou, W.S., Wei, Y.Y., *Performance of Undoped BGO Crystals Under Extremely High Dose Conditions*, Nuclear Instruments & Methods in Physics Research, Sect. A, Vol. 427, 1999, pp 524-527.

(19) Zhang, N., Ding, Z., Wu, Y., Salomon, M., *Study of a Large BGO Crystal in a Charged Particle Beam*, IEEE Transactions on Nuclear Science, Vol. 37, No. 2, April 1990, pp 216-219.

(20) Williams, P.A., Rose, A.H., Lee, K.S., Conrad, D.C., Day, G.W., Hale, P.D., Optical, *Thermo-Optic, Electro-Optic, and Photoelastic Properties of Bismuth Germanate ($Bi_4Ge_3O_{12}$)*, Applied Optics, Vol. 35, No. 19, July 1996, pp 3562-3569.

(21) Kamada, O., Kakishita, K., *Electro-Optical Effect of* $Bi_4Ge_3O_{12}$ *Crystals for Optical Voltage Sensors*, Japanese Journal of Applied Physics, Vol. 32, September 1993, pp 4288-4291.

(22) Collett, E., *Polarized Light*, Marcel Dekker, Inc., New York, NY, 1993

(23) Yariv, A., *Quantum Electronics*, Third Edition, John Wiley and Sons, Inc., New York, NY, 1989.

(24) Born, M., Wolf, E., *Principles of Optics*, Seventh Edition, Cambridge University Press, New York, NY, 1999.

(25) Bass, M., *Handbook of Optics: Volume I*, Second Edition, McGraw-Hill, Inc., New York, NY, 1995.

(26) Bass, M., *Handbook of Optics: Volume II*, Second Edition, McGraw-Hill, Inc., New York, NY, 1995.

(27) Möller, K.D., *Optics*, University Science Books, Mill Valley, CA, 1988.

(28) Wilson, J., Hawkes, J., *Optoelectronics: an introduction*, Third Edition, Prentice Hall Europe, Hemel Hempstead, Hertfordshire, UK, 1998.

(29) Pollock, C.R., *Fundamentals of Optoelectronics*, Richard D. Irwin, Inc., Chicago, IL, 1995.

(30) Wood, E.A., *Crystals and Light: An Introduction to Optical Crystallography*, Second Edition, Dover Publications, Inc., New York, NY, 1977.

(31) Santos, J., Taplamacioglu, M., Hidaka, K., *Pockels High-Voltage Measurement System*, IEEE Transactions on Power Delivery, Vol. 15, No. 1, January 2000, pp 8-13.

(32) Milek, J., Neuberger, M., *Linear Electro-Optic Modular Materials*, Plenum Data Corporation, New York, NY, 1972.

(33) Edvold, B., Andersen, P., Buchhave, P., Petersen, P., *Polarization Properties of a Photorefractive* $Bi_{12}SiO_{20}$ *Crystal and their Application in an Optical Correlator*, IEEE Journal of Quantum Electronics, Vol. 30, No. 4, April 1994, pp 1075-1089.

(34) Montemezzani, G., Pfandler, St., Gunter, P., *Electro-optic and photorefractive properties of* $Bi_4Ge_3O_{12}$ *crystals in the ultraviolet spectral range*, Journal of the Optical Society of America: B, Vol. 9, No. 7, July 1992, pp 1110-1117.

(35) Nitsche, R., *Crystal Growth and Electro-Optic Effect of Bismuth Germanate,* $Bi_4(GeO_4)_3$, Journal of Applied Physics, Vol. 36, No. 8, August 1965, pp 2358-2360.

(36) Babucke, H., Thiele, P., Prasse, T., Egorov, V., Rabe, M., Henneberger, F., *Electro-optical modulation in the blue-green spectral range using ZnSe-based waveguides*, Journal of Crystal Growth, Vol. 159, 1996, pp 898-901.

(37) Babucke, H., Thiele, P., Prasse, T., Rabe, M., Henneberger, F., *ZnSe-based electro-optic waveguide modulators for the blue-green spectral range*, Semiconductor Science and Technology, Vol. 13, February 1998, pp 200-206.

(38) Haase, M., Cheng, H., Misemer, D., Strand, T., DePuydt, J., *ZnSe-ZnSSe electro-optic waveguide modulators*, Applied Physics Letters, Vol. 59, No. 25, 16 December 1991, pp 3228-3229.

(39) Baillou, J., Lemercier, M., Rivaud, G., Pavis, B., *Effet Electro-Optique Dans les Cristaux de ZnSe*, Revue de Physique Appliquee, Vol. 8, No. 2, June 1973, pp 121-126.

(40) Pellat-Finet, P., *Measurement of the electro-optic coefficient of BSO crystals*, Optics Communications, Vol. 50, No. 5, 1 July 1984, pp 275-280.

(41) Mallick, S., Rouede, D., Apostolidis, A., *Efficiency and polarization characteristics of photorefractive diffraction in a* $Bi_{12}SiO_{20}$ *crystal*, Journal of the Optical Society of America: B, Vol. 4, No. 8, August 1987, pp 1247-1259.

(42) Murillo, J., *Photorefractive grating dynamics in* $Bi_{12}SiO_{20}$ *using optical pulses*, Optics Communications, Vol. 159, 1999, pp 293-300.

(43) Shepelevich, V. V., Egorov, N., Shepelevich, V., *Orientation and polarization effects of two-beam coupling in a cubic optically active photorefractive piezoelectric BSO crystal*, Journal of the Optical Society of America: B, Vol. 11, No. 8, August 1994, pp 1394-1402.

(44) Aldrich, R., Hou, S., Harvill, M., *Electrical and Optical Properties of* $Bi_{12}SiO_{20}$, Journal of Applied Physics, Vol. 42, 1971, pp 493-494

(45) Grunnet-Jepsen, A., Aubrecht, I., Solymar, L., *Investigation of the internal field in photorefractive materials and measurement of the effective electro-optic coefficient*, Journal of the Optical Society of America: B, Vol. 12, No. 5, May 1995, pp 921-929.

(46) Henry, M., Mallick, S., Rouede, D., *Propagation of light in an optically active electro-optic crystal of* $Bi_{12}SiO_{20}$*: Measurement of the electro-optic coefficient*, Journal of Applied Physics, Vol. 59, No. 8, 15 April 1986, pp 2650-2654.

(47) Vachss, F., Hesselink, L., *Measurement of the electrogyratory and electro-optic effects in BSO and BGO*, Optics Communications, Vol. 62, No. 3, 1 May 1987, pp 159-165.

(48) Han, S., Wu, J., *Polarization-interferometry measurement of the Pockels coefficient in a chiral* $Bi_{12}SiO_{20}$ *single crystal*, Journal of the Optical Society of America: B, Vol. 17, No. 7, July 2000, pp 1205-1210.

(49) Lamaire, Ph., Georges, M., *Local measurement system for optical and electro-optic characterization and homogeneity analysis of photorefractive sillenite crystals*, Optical Materials, Vol. 4, January 1995, pp 182-187.

(50) Xue, D., Zhang, S., *Bond-charge Calculation of Electro-Optic Coefficients of Diatomic Crystals*, Journal of Solid State Chemistry, Vol. 128, January 1997, pp 17-20.

(51) Bayvel, P., McCall, M., Wright, R., *Continuous method for measuring the electro-optic coefficient in* $Bi_{12}SiO_{20}$ *and* $Bi_{12}GeO_{20}$, Optics Letters, Vol. 13, No. 1, January 1988, pp 27-29.

(52) Marple, D., *Refractive Index of ZnSe, ZnTe, and CdTe*, Journal of Applied Physics, Vol. 35, No. 3, March 1964, pp 539-542.

(53) Bortfeld, D., Meier, H., *Refractive indices and electro-optic coefficients of the eulitites* $Bi_4Ge_3O_{12}$ *and* $Bi_4Si_3O_{12}$, Journal of Applied Physics, Vol. 43, No. 12, December 1972, pp 5110-5111.

(54) Shea, N., McFarland, L., Oakes, M., Gaskey, A., *DARHT: Dual-Axis Radiographic Hydrodynamic Test Facility*, CIC-9 Imaging Services LANL, August 1999.

(55) Nelson, S., Fessenden, T., Yu, C., Holmes, C., Selchow, N., *High Precision Electron Beam Diagnostic System for High Current Long Pulse Beams*, Proceedings of the 1999 Particle Accelerator Conference, New York, 1999, pp 2235-2237.

(56) Theofanous, N., *Analysis of Circular-Polarization Electrooptic Amplitude Modulators*, IEEE Journal of Quantum Electronics, Vol. 31, No. 7, July 1995, pp 1315-1325.

(57) Cecelja, F., Bordovsky, M., Balachandran, W., *Lithium Niobate Sensor for Measurement of DC Electric Fields*, IEEE Transactions on Instrumentation and Measurement, Vol. 50, No. 2, April 2001, pp 465-469.

(58) Anastassakis, E., *Photorefractive Effects in Cubic Crystals: Explicit Treatment of the Piezoelectric Contribution*, IEEE Journal of Quantum Electronics, Vol. 29, No. 7, July 1993, pp 2239-2244.

(59) Cho, P., Ho, P., Goldhar, J., Lee, C., *Photoconductivity in ZnSe Under High Electric Fields*, IEEE Journal of Quantum Electronics, Vol. 30, No. 6, June 1994, pp 1489-1497.

(60) Paulait, G., Besson, C., Roosen, G., *Polarization Properties of Two-Wave Mixing Under and Alternating Electric Field in BSO Crystals*, IEEE Journal of Quantum Electronics, Vol. 25, No. 7, July 1989, pp 1736-1740.

(61) Tassev, V., Gospodinov, M., Veleva, M., *Optical activity of BSO crystals doped with Cr, Mn and Cu, Optical Materials*, Vol. 13, 1999, pp 249-253.

(62) Hamurty, N., *Photoelastic & Electro-Optic Properties of Crystals*, Plenum Press, New York, NY, 1981.

(63) Kaminow, I., *An Introduction to Electrooptic Devices*, Academic Press, New York, NY, 1974.

(64) Jupina, M., Garmire, E., Shibata, N., Zembutsu, S., *Electroabsorption and Electrooptic Modulation in Single Crystal ZnSe-ZnSSe Waveguides Grown by OMPVE on GaAs*, IEEE Journal of Quantum Electronics, Vol. 28, No. 3, March 1992, pp 663-669.

(65) Goodman, J., *Introduction to Fourier Optics*, 2nd Edition, The McGraw-Hill Companies, New York, NY, 1996.

(66) Ulaby, F., *Fundamentals of Applied Electromagnetics*, Prentice Hall, Upper Saddle River, NJ, 1997.

(67) Sadiku, M., *Elements of Electromagnetics*, Second Edition, Oxford University Press, New York, NY, 1995.

(68) Serway, R., *Physics for Scientists & Engineers with Modern Physics*, Third Edition, Harcourt Brace & Company, Philadelphia, PA, 1992.

(69) Ramo, S., Whinnery, J., Van Duzer, T., *Fields and Waves in Communication Electronics*, Third Edition, John Wiley & Sons, Inc., New York, NY, 1994.

(70) Jenkins, F., White, H., *Fundamentals of Optics*, Third Edition, McGraw-Hill Book Company, New York, NY, 1957.

(71) Humphries Jr., S., *Charged Particle Beams*, John Wiley and Sons, New York, NY, 1990.

(72) Humphries Jr., S., *Principles of Charged Particle Acceleration*, John Wiley and Sons, New York, NY, 1986.